

CALIFA, the Calar Alto Legacy Integral Field Area survey

III. Second public data release[★]

R. García-Benito¹, S. Zibetti², S. F. Sánchez³, B. Husemann⁴, A. L. de Amorim⁵, A. Castillo-Morales⁶, R. Cid Fernandes⁵, S. C. Ellis⁷, J. Falcón-Barroso^{8,9}, L. Galbany^{10,11}, A. Gil de Paz⁶, R. M. González Delgado¹, E. A. D. Lacerda⁵, R. López-Fernández¹, A. de Lorenzo-Cáceres¹², M. Lyubenova^{13,14}, R. A. Marino¹⁵, D. Mast¹⁶, M. A. Mendoza¹, E. Pérez¹, N. Vale Asari⁵, J. A. L. Aguerri^{8,9}, Y. Ascasibar¹⁷, S. Bekeraité¹⁸, J. Bland-Hawthorn¹⁹, J. K. Barrera-Ballesteros^{8,9}, M. Cano-Díaz³, C. Catalán-Torrecilla⁶, C. Cortijo¹, G. Delgado-Inglada³, M. Demleitner²⁰, R.-J. Dettmar^{21,22}, A. I. Díaz¹⁷, E. Florido^{23,34}, A. Gallazzi^{2,24}, B. García-Lorenzo^{8,9}, J. M. Gomes²⁵, L. Holmes²⁶, J. Iglesias-Páramo^{1,27}, K. Jahnke¹⁴, V. Kalinova²⁸, C. Kehrig¹, R. C. Kennicutt Jr.²⁹, Á. R. López-Sánchez^{30,31}, I. Márquez¹, J. Masegosa¹, S. E. Meidt¹⁴, J. Mendez-Abreu¹², M. Mollá³², A. Monreal-Ibero³³, C. Morisset³, A. del Olmo¹, P. Papaderos²⁵, I. Pérez^{23,34}, A. Quirrenbach³⁵, F. F. Rosales-Ortega³⁶, M. M. Roth¹⁸, T. Ruiz-Lara^{23,34}, P. Sánchez-Blázquez¹⁷, L. Sánchez-Menguiano^{1,23}, R. Singh¹⁴, K. Spekkens²⁶, V. Stanishev^{37,38}, J. P. Torres-Papaqui³⁹, G. van de Ven¹⁴, J. M. Vilchez¹, C. J. Walcher¹⁸, V. Wild¹², L. Wisotzki¹⁸, B. Ziegler⁴⁰, and J. Aceituno²⁷

(Affiliations can be found after the references)

ABSTRACT

This paper describes the Second Public Data Release (DR2) of the Calar Alto Legacy Integral Field Area (CALIFA) survey. The data for 200 objects are made public, including the 100 galaxies of the First Public Data Release (DR1). Data were obtained with the integral-field spectrograph PMAS/PPak mounted on the 3.5 m telescope at the Calar Alto observatory. Two different spectral setups are available for each galaxy, (i) a low-resolution V500 setup covering the wavelength range 3745–7500 Å with a spectral resolution of 6.0 Å (FWHM), and (ii) a medium-resolution V1200 setup covering the wavelength range 3650–4840 Å with a spectral resolution of 2.3 Å (FWHM). The sample covers a redshift range between 0.005 and 0.03, with a wide range of properties in the Color-Magnitude diagram, stellar mass, ionization conditions, and morphological types. All released cubes were reduced with the latest pipeline, including improved spectrophotometric calibration, spatial registration and spatial resolution. The spectrophotometric calibration is better than 6% and the median spatial resolution is 2''.5. Altogether the second data release contains over 1.5 million spectra. It is available at <http://califa.caha.es/DR2>.

Key words. techniques: spectroscopic - galaxies: general - surveys

1. Introduction

The Calar Alto Legacy Integral Field Area (CALIFA) survey (Sánchez et al. 2012a, hereafter S12) is an ongoing large project of the Centro Astronómico Hispano-Alemán at the Calar Alto observatory (Almería, Spain) to obtain spatially resolved spectra for 600 galaxies in the Local Universe by means of integral field spectroscopy (IFS). CALIFA observations started in June 2010 with the Potsdam Multi Aperture Spectrograph (PMAS, Roth et al. 2005), mounted on the 3.5 m telescope, utilizing the large hexagonal field-of-view (FoV) offered by the PPak fiber bundle (Verheijen et al. 2004; Kelz et al. 2006). Each galaxy is observed using two different setups: an intermediate spectral resolution one (V1200, $R \sim 1650$) and a low-resolution one (V500, $R \sim 850$). A diameter-selected sample of 939 galaxies was drawn from the 7th data release of the Sloan Digital Sky Survey (SDSS DR7, Abazajian et al. 2009) which is described

in Walcher et al. (2014, hereafter W14). From this mother sample the 600 target galaxies are randomly selected.

Combining the techniques of imaging and spectroscopy through optical IFS provides a more comprehensive view of individual galaxy properties than any traditional survey. CALIFA-like observations were collected during the feasibility studies (Mármol-Queraltó et al. 2011; Viironen et al. 2012) and the PPak IFS Nearby Galaxy Survey (PINGS, Rosales-Ortega et al. 2010), a predecessor of this survey. First results based on those datasets already explored their information content (e.g., Sánchez et al. 2011; Rosales-Ortega et al. 2011; Alonso-Herrero et al. 2012; Sánchez et al. 2012b; Rosales-Ortega et al. 2012). CALIFA can therefore be expected to make a substantial contribution to our understanding of galaxy evolution in various aspects, including (i) the relative importance and consequences of merging and secular processes; (ii) the evolution of galaxies across the color-magnitude diagram; (iii) the effects of the environment on galaxies; (iv) the AGN–host galaxy connection; (v) the internal dynamical processes in galaxies; and (vi) the global and spatially

[★] Based on observations collected at the Centro Astronómico Hispano Alemán (CAHA) at Calar Alto, operated jointly by the Max-Planck-Institut für Astronomie (MPIA) and the Instituto de Astrofísica de Andalucía (CSIC)

resolved star formation history and chemical enrichment of various galaxy types.

Compared with previous IFS surveys, e.g., Atlas3D (Cappellari et al. 2011) or DMS (Bershady et al. 2010), CALIFA covers a much wider range of morphological types over a large range of masses, sampling the entire Color-Magnitude diagram for $M_r > -19$ mag. While the recently started SAMI (Croom et al. 2012; Bryant et al. 2014) and MaNGA (Law & MaNGA Team 2014) surveys have a similarly broad scope as CALIFA and aim at building much larger samples, CALIFA has still an advantage in terms of spatial coverage and sampling. For 50% of the galaxies, CALIFA provides data out to $3.5 r_e$, and for 80% out to $2.5 r_e$. At the same time the spatial resolution of ~ 1 kpc is typically better than in either SAMI or MaNGA, revealing several of the most relevant structures in galaxies (spiral arms, bars, bulges, giant H 2 regions, etc.). CALIFA has lower spectral resolution than these two surveys in the red, but is comparable for the blue wavelength range.

So far, a number of science goals have been addressed using the data from the CALIFA survey: (i) New techniques have been developed to understand the spatially resolved star formation histories (SFH) of galaxies (Cid Fernandes et al. 2013, 2014). We found solid evidence that mass-assembly in the typical galaxies happens from the inside-out (Pérez et al. 2013). The SFH and metal enrichment of bulges and early-type galaxies are fundamentally related to the total stellar mass, while for disk galaxies it is more related to the local stellar mass density (González Delgado et al. 2014b,a); (ii) We developed new tools to detect and extract the spectroscopic information of H II (Sánchez et al. 2012b), building the largest catalog currently available ($\sim 6,000$ H II regions and aggregations). This catalog has been used to define a new oxygen abundance calibrator anchored to electron temperature measurements (Marino et al. 2013). From these, we explored the dependence of the mass-metallicity relation with Star Formation Rate (Sánchez et al. 2013), and the local mass-metallicity relation (Rosales-Ortega et al. 2012). We found that all galaxies in our sample present a common gas-phase oxygen abundance radial gradient with a similar slope when normalized to the effective radius (Sánchez et al. 2014), which agrees with an inside-out scenario for galaxy growth. This characteristic slope is independent of the properties of the galaxies, and in particular of the presence or absence of a bar, contrary to previous results. More recently, this result has been confirmed by the analysis of the stellar abundance gradient in the same sample (Sanchez-Blazquez et al. 2014); (iii) We explored the origin of the low intensity, LINER-like, ionized gas in galaxies. These regions are clearly not related to star-formation activity, or to AGN activity. They are most probably related to post-AGB ionization in many cases (Kehrig et al. 2012; Singh et al. 2013; Papaderos et al. 2013); (iv) We explored the aperture and resolution effects on the data. CALIFA provides a unique tool to understand the aperture and resolution effects in larger single-fiber (e.g. SDSS) and IFS surveys (e.g. MaNGA, SAMI). We explored the effects of the dilution of the signal in different gas and stellar population properties (Mast et al. 2014), and proposed a new empirical aperture correction for the SDSS data (Iglesias-Páramo et al. 2013); (v) We have analysed the local properties of the ionized gas and stellar population of galaxies where supernovae (SNe) have exploded. Core collapse SNe are found closer to younger stellar populations, while SNe Ia show no correlation to stellar age (Galbany et al. 2014); (vi) CALIFA is the first IFS survey that allows gas and stellar kinematic studies for all morphologies with enough spectroscopic resolution to study (a) the kinematics of the ionized gas (García-Lorenzo et al. 2014), (b) the

effects of bars in the kinematics of galaxies (Barrera-Ballesteros et al. 2014); (c) the effects of the interaction stage on the kinematic signatures (Barrera-Ballesteros et al., submitted), (d) the Bar Pattern Speeds in late-type galaxies (Aguerri et al., submitted), (e) the measurements of the angular momentum of galaxies to previously unexplored ranges of morphology and ellipticity (Falcón-Barroso et al., in prep.); (vii) We explored the effects of a first stage merger on the gas and stellar kinematics, star formation activity and stellar populations of the Mice merging galaxies (Wild et al. 2014).

In this article, we introduce the second data release (DR2) of CALIFA, which grants public access to high-quality data for a set of 200 galaxies (400 datacubes). All released cubes have been reduced with the latest pipeline, including improved spectrophotometric calibration, spatial registration and spatial resolution. This DR supersedes and increases by a factor of two the amount of data delivered in DR1 (Husemann et al. 2013, hereafter H13).

DR1 opened CALIFA to the community, and allowed for the exploration of several different scientific avenues not addressed by the collaboration (e.g. Holwerda & Keel 2013; De Geyter et al. 2014; Martínez-García et al. 2014; Davies et al. 2014). The properties of the galaxies in the DR2 sample are summarized in Sect. 2. We describe the processing (Sect. 3), structure (Sect. 4), and data (Sect. 5) of the distributed CALIFA data as essential information for any scientific analysis. The several interfaces to access the CALIFA DR2 data are explained in Sect. 6.

2. The CALIFA DR2 sample

The CALIFA “mother sample” (MS) consists of 939 galaxies drawn from SDSS DR7. The main criteria for the target selection are: angular isophotal diameter ($45'' < isoA_r < 79.2''$) of the galaxies¹; redshift range $0.005 < z < 0.03$; cut in Galactic latitude to exclude the Galactic plane ($|b| > 20^\circ$); flux limit of $petroMag_r < 20$; declination limit to $\delta > 7^\circ$. Redshift limits were imposed so that the sample would not be dominated by dwarf galaxies and in order to keep relevant spectral features observed with a fixed instrumental spectral setup. Redshift information was taken from SIMBAD for all galaxies where SDSS DR7 spectra were unavailable. The cut in declination was chosen to reduce problems due to differential atmospheric refraction (DAR) and PMAS flexure issues, but was not applied to the SDSS Southern area due to the sparsity of objects in this region. The reader is referred to W14 for a comprehensive characterization of the CALIFA MS and a detailed evaluation of the selection effects implied by the chosen criteria. From the CALIFA MS, 600 galaxies are randomly selected for observation purely based on visibility, and we refer to these galaxies as the virtual final CALIFA sample hereafter.

The 200 DR2 galaxies, which include the first 100 galaxies of DR1, were observed in both spectral setups from the start of observations in June 2010 until December 2013. We list these galaxies in Table 1 together with their primary characteristics. The distribution of galaxies in the sky follows the underlying SDSS footprint (Fig. 1). The number of galaxies in DR2 is not homogeneous as a function of right ascension, $\alpha(J2000)$, and has three mean clear peaks at around $\alpha \sim 15^\circ$, 255° and 345° . All three peaks are located in the same season run, in the period

¹ $isoA_r$ is the isophote major axis at 25 magnitudes per square arcsecond in the r -band. For other SDSS pipeline parameters meaning, the reader is referred to the DR7 webpage: <http://skyserver.sdss.org/dr7/en/help/browser/browser.asp>

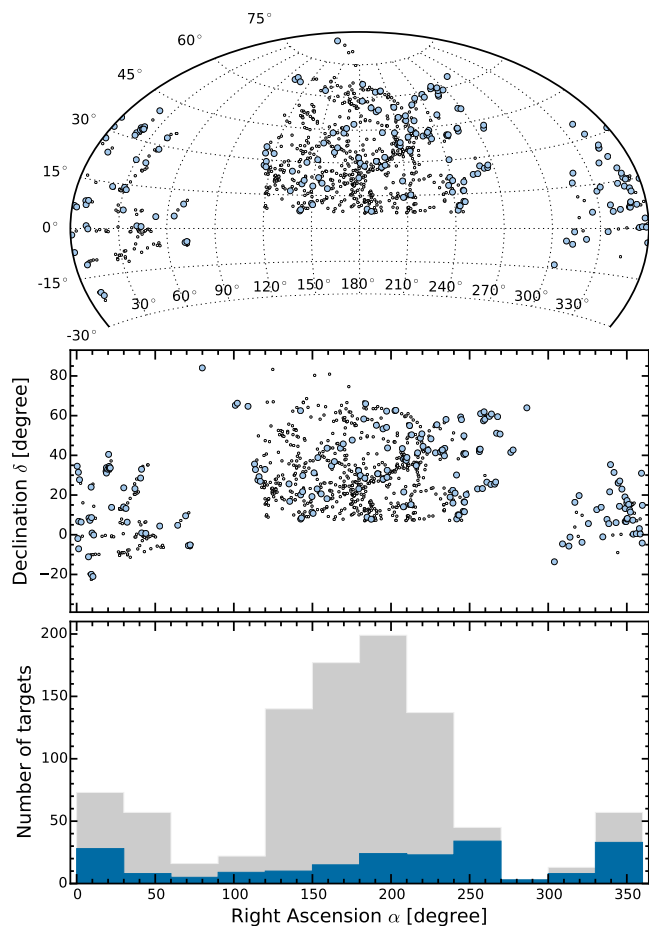


Fig. 1. Distribution on the sky of galaxies in the CALIFA mother sample (black dots) and CALIFA DR2 sample (blue filled symbols). The upper panel shows the distribution in an Aitoff projection in J2000 Equatorial Coordinates (cut off at $\delta = -30^\circ$, below which the sample does not extend), while the middle panel is plotted in the cartesian system. The lower panel shows both samples as a function of right ascension. The number distribution in bins of 30° along the right ascension is shown for the mother sample (grey area) and the DR2 sample (blue area).

from April to October. As noted in H13, there was a downtime of the 3.5 m telescope from August 2010 until April 2011 due to operational reasons at the observatory, which delayed the survey roughly by 8 months. In addition to this, due to scheduling matters, a large part of the granted time was allocated in summer seasons. Regardless of the observing time issue, the distribution of physical properties for DR2 is nearly random, as expected, and covers galaxies with a wide range of properties as discussed below.

Figure 2 shows the distribution of galaxies in the color-magnitude diagram. It is evident that the DR2 sample covers nearly the full range of the CALIFA MS. On average, the DR2 targets comprise $\sim 37\%$ per color-magnitude bin of the total 600 objects when CALIFA is completed. The deficit of low luminosity galaxies with intermediate colors noted in DR1 has improved. Fluctuations can be explained by the effect of low number statistics, especially within those color-magnitude bins in which the MS contains fewer galaxies. This point is highlighted in Figure 2 and emphasizes the need to increase further the numbers to the full CALIFA sample to obtain enough galaxies in each bin for a meaningful multi-dimensional statistical analysis.

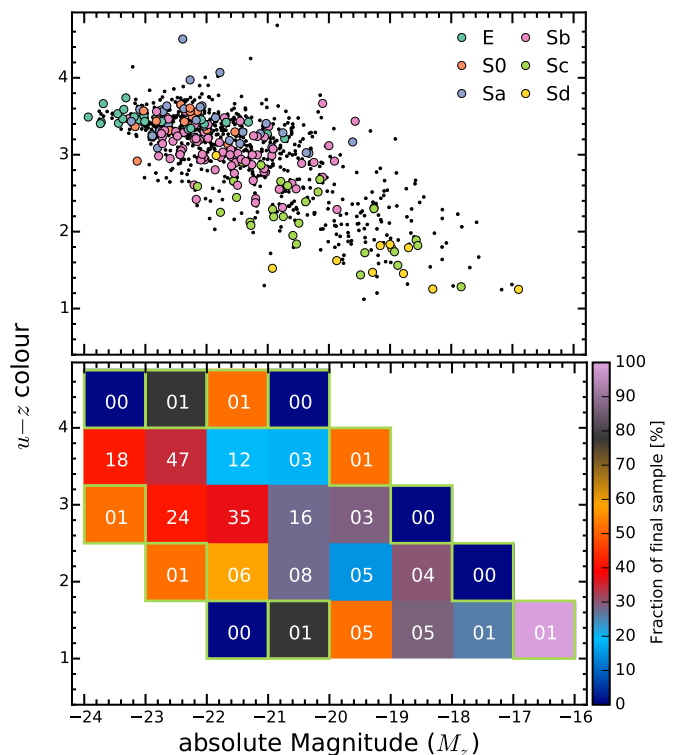


Fig. 2. Upper panel: Distribution of CALIFA galaxies in the $u-z$ vs. M_z color-magnitude diagram. Black dots denote galaxies in the CALIFA mother sample (S12, W14) and colored symbols indicate CALIFA DR2 galaxies. Different colors account for the morphological classification, which range from ellipticals (E) to late-type spirals (Sd). Lower panel: Fraction of galaxies in the DR2 sample with respect to the expected final CALIFA sample distribution (600 objects) in bins of 1 mag in M_z and 0.75 mag in $u-z$. The total number of galaxies per bin in the DR2 sample is shown in each bin. Bins for which the number of galaxies in the mother sample is less than 5 are prone to low-number statistics and enclosed by a green square for better identification.

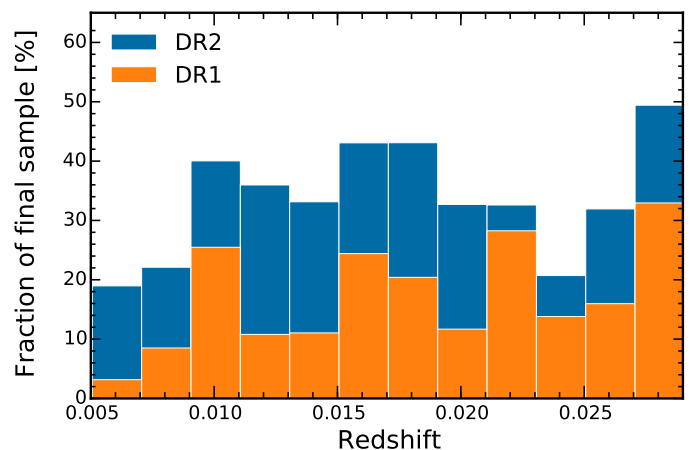


Fig. 3. Redshift distribution of the DR2 (blue) and DR1 (orange) as a fraction of the final CALIFA sample.

Figure 3 compares the redshift distribution of the CALIFA galaxies in the DR2 and DR1, as a fraction of the CALIFA sample. As it can be seen, except for a few particular bins, the redshift distribution is homogeneous with respect to the final sample.

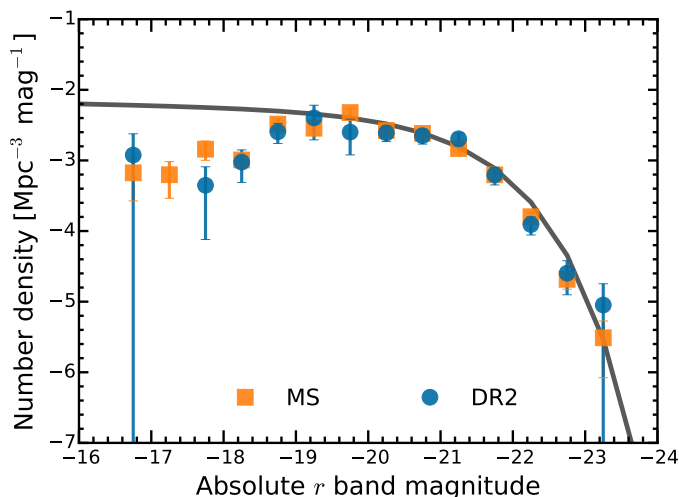


Fig. 4. Luminosity functions in the r band of the CALIFA mother sample (orange squares) and the DR2 sample (blue points). Error bars represent Poissonian uncertainties. The line shows the Schechter fit to the LF of Blanton et al. (2005).

One important test to be made is whether the number density of galaxies estimated from the CALIFA sample is in accordance with other surveys. Figure 4 shows the r -band luminosity function (LF) of the DR2 sample as compared to the MS and the reference SDSS sample of Blanton et al. (2005). The reader is referred to W14 for all technical details on how the LFs are obtained and for the explanation of the turnover of the LF at $M_r \approx -18.6$. It should be noted that the DR2 sample already reproduces very closely the CALIFA MS LF in most of its magnitude bins.

An important characteristic of the CALIFA MS is that it contains galaxies of all morphological types. Galaxy morphologies were inferred by combining the independent visual classifications of several collaboration members as described in W14. Fig. 5 shows a histogram of bars strengths as well as the fraction of DR2 galaxies with respect to the expected final sample distribution for different morphological types grouped into elliptical, lenticular and spiral galaxies (and subtypes). A more detailed classification of ellipticals (from 0 to 7) is available, but we do not distinguish between them here because of the low number of galaxies per elliptical subtype within DR2. From 200 galaxies in DR2, 18 have been classified as ongoing mergers² (of any type). As clearly seen in Fig. 5, the fraction of DR2 galaxies with respect to the expected final sample is almost constant for all types, implying that the DR2 coverage seems to be consistent with a random selection. Axis ratios (b/a) were measured from the SDSS r -band image from growth curve analysis by calculating light moments after proper sky subtraction and masking of foreground stars (see W14 for details). The axis ratios can be used as a proxy of the inclination of spiral galaxies. Figure 6 shows that the DR2 sample covers the same range of axis ratios as the final sample. A Kolmogorov-Smirnov test confirms with $> 95\%$ confidence that the morphology and the axis-ratio distributions of DR2 are consistent with being randomly drawn from the CALIFA MS.

In Fig. 7, we present the distribution of stellar masses for the DR2 galaxies. Galaxy stellar masses are from González Delgado et al. (2014a), and they have been estimated following the process described in Pérez et al. (2013), Cid Fernandes et al. (2013, 2014) and González Delgado et al. (2014b). These masses ac-

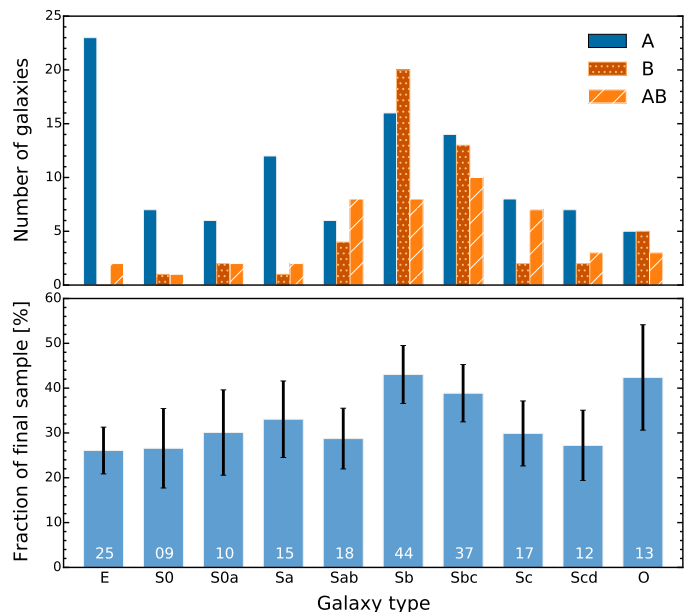


Fig. 5. The distribution of visually classified morphological types in the DR2 sample. We divide the galaxies into ellipticals (E), spirals (from S0 to Scd) and the *other* group “O” which includes Sd, Sdm, Sm and I (only one) types. *Upper panel:* Bar strength histogram, where A stands for non-barred, B for barred and AB if unsure. *Lower panel:* The fraction of galaxies in the DR2 sample with respect to the expected final CALIFA sample distribution. The total number of galaxies in the DR2 for each morphology type is written on each bar. Error bars are computed from the Poisson errors of the associated DR2 number counts. The morphological distribution of the DR2 sample is similar to that of the mother sample.

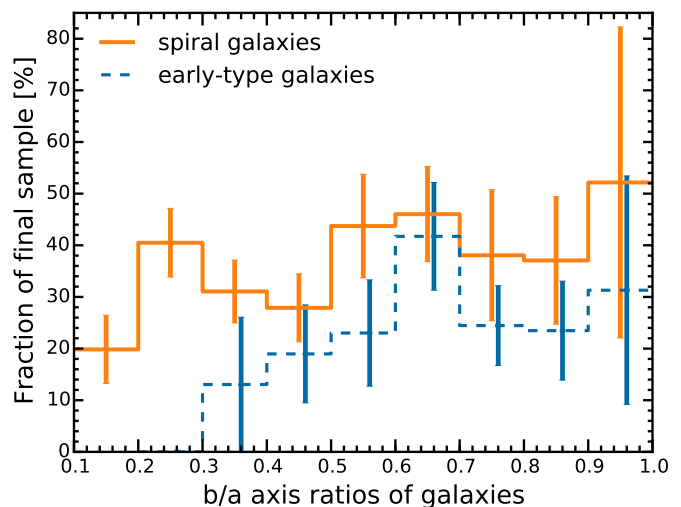


Fig. 6. The fraction of galaxies in the DR2 sample with respect to the expected final CALIFA sample distribution, as a function of the light-weighted axis ratio (b/a). Galaxies were separated into early-type galaxies (E+S0) and spiral galaxies (Sa and later). The CALIFA mother sample does not include any elliptical galaxies with $b/a < 0.3$. Error bars are computed from the Poisson errors of the associated DR2 number counts.

count for spatial variations in both M/L ratio and stellar extinction. In short, we use the STARLIGHT code (Cid Fernandes et al. 2005) to fit each spectrum extracted from the datacube with a combination of SSP models from the Granada (González Delgado et al. 2005) and MILES (Vazdekis et al. 2010) libraries, that

² According to our visual classification.

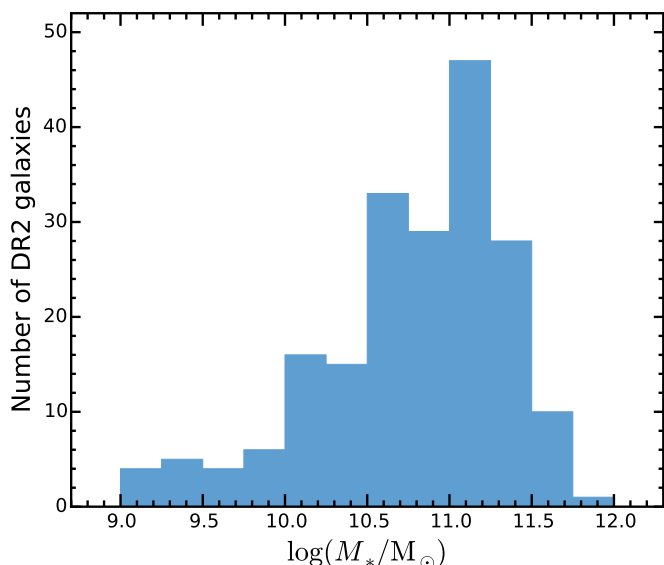


Fig. 7. Distribution of stellar masses in the DR2 sample. The stellar masses have been determined from the CALIFA data using spectral fitting techniques (see text for details).

cover the full metallicity range of the MILES models ($\log Z/Z_\odot$ from -2.3 to $+0.22$), and ages from 0.001 to 14 Gyr. We assume a Salpeter IMF. The DR2 galaxies cover intermediate to high-mass galaxies, including at least 10 galaxies per 0.25 dex bin between 10^{10} and $10^{12} M_\odot$ and a median value close to $10^{11} M_\odot$. The asymmetric distribution is expected from the distribution in absolute magnitudes (see Fig. 2) and is inherited from the CALIFA MS due to its selection criteria (see W14 for details).

A more general “panoramic view” of the DR2 sample characteristics is presented in Fig. 8. Several of the main properties observable in 2D are highlighted for 169 randomly-selected galaxies, shown individually in hexagons that together form the shape of a CALIFA-like FoV. The galaxies have been ordered by r -band absolute magnitude (a proxy for the stellar mass), from top right (lowest absolute magnitude) to bottom left (highest absolute magnitude). The highlighted properties derive from several different analysis pipelines developed within the collaboration. Stellar properties like ages and mass surface density were measured with the STARLIGHT code (see references in the preceding paragraph describing the distribution of stellar masses in the sample) while gas properties and emission lines were measured using FIT3D (Sánchez et al. 2007). This plot is only intended to demonstrate the diversity of the DR2 sample.

3. Data processing and error propagation

For the sake of completeness, we provide here a brief summary of the instrument layout and observing strategy. All the details can be found in S12. The PPAk fiber bundle of the PMAS instrument has a FoV of $74'' \times 64''$. There are 382 fibers in total, distributed in 3 different groups. The PPAk Integral Field Unit (IFU) holds 331 “science” fibers in a hexagonal grid with a maximum diameter of $74''$ while each fiber projects to $2''.7$ in diameter on the sky. The fiber-to-fiber distance is $3''.2$ which yields a total filling factor of 0.6 . An additional set of 36 fibers devoted to measuring the surrounding sky level are distributed in six bundles of 6 fibers each, located in a circle $72''$ from the center. Finally, there are 15 extra fibers connected to the calibration unit.

Every galaxy in the CALIFA sample is observed in the optical range using two different overlapping setups. The V500 low-resolution mode ($R \sim 850$) covers the range 3745 – 7500 Å, but it is affected by internal vignetting within the spectrograph giving an unvignetted range of 4240 – 7140 Å. The blue mid-resolution setup (V1200; $R \sim 1650$) covers the range 3400 – 4840 Å with an unvignetted range of 3650 – 4620 Å. The resolutions quoted are those at the overlapping wavelength range ($\lambda \sim 4500$ Å). In order to reach a filling factor of 100% across the FoV, a 3-pointing dithering scheme is used for each object. The exposure time per pointing is fixed. V1200 observations are carried out during dark nights with an exposure time of 1800 s (split in 2 or 3 individual exposures) pointing. V500 observations are taken during grey nights with 900 s per pointing.

In the following section we describe the new improvements to the CALIFA data reduction pipeline used to produce the DR2 data.

3.1. Improvements on the CALIFA data reduction scheme

As described in H13, since V1.3c the CALIFA pipeline has a Python-based architecture (Py3D package). The main improvements to the current pipeline V1.5 are: i) new sensitivity curve for V500 setup obtained from a dedicated calibration programme for several CALIFA elliptical galaxies (Husemann et al., in preparation) ii) a new registering method, comparing individual CALIFA pointings with SDSS images; iii) an improved image reconstruction method (cube interpolation). Among others, step ii) also improves the absolute photometric matching of the three dithered pointings.

The new version starts with the Raw Stacked Spectra (RSS) files of the three individual pointings after sky subtraction produced by pipeline V1.3c. The V500 RSS files are then spectrophotometrically re-calibrated with the new sensitivity curve (undoing the V1.3c calibration). A new estimate for the sensitivity curve was necessary to account for severe wavelength-dependent aperture losses particular to standard star observations that have low fiber filling factor given the large fiber diameter of PPAk. We therefore re-observed about two dozen elliptical CALIFA galaxies with the PMAS Lens-Array (LArr) and the V300 grism with a continuous $16'' \times 16''$ FoV covering the bright center of the galaxy. The details of those observations and their application to coarse-fiber IFS will be presented in a separate publication (Husemann et al., in preparation), but we briefly outline the concept and its application to CALIFA data here.

A robust spectrophotometric calibration can be assembled using observations of standard stars in the PMAS LArr mode, in which aperture losses are absent, and the atmospheric extinction curve has been directly estimated for each observing night, instead of using the average extinction curve derived by Sánchez et al. (2007). We derive a new sensitivity curve using these secondary spectrophotometric standards, by comparing the LArr flux spectra against the observed count spectra in targeted elliptical galaxies over the same aperture. The latter should be much less sensitive to wavelength-dependent aperture losses, given that the surface brightness profiles of elliptical galaxies smoothly vary over several tens of arcseconds. To match the apertures and increase the S/N, all CALIFA fibers that fall within the LArr FoV are co-added together. PPAk spectra are further smoothed to 9 Å FWHM, matching the spectral resolution of the V300 LArr observations, to improve the match between the spectra. To the resulting sensitivity curve we fit a high-order polynomial, creating a noise-free representation. Then we derive a master sen-

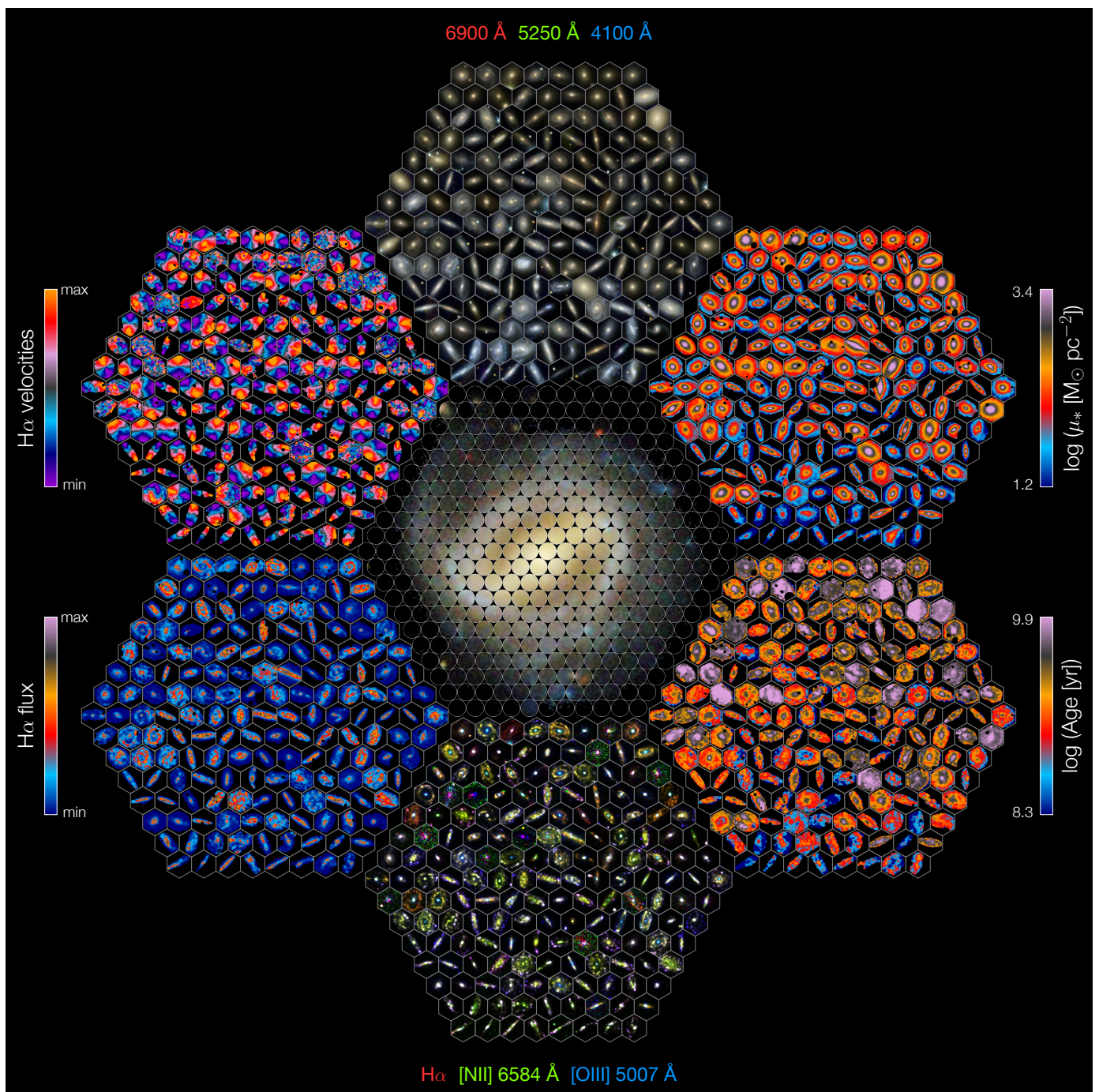


Fig. 8. CALIFA “panoramic view” (also CALIFA’s “Mandala”) representation, consisting of the basic physical properties (all of them derived from the CALIFA datacubes) of a subsample of 169 galaxies extracted randomly from DR2. We show 1) broad band images (top center; central wavelength 6900 Å, 5250 Å, and 4100 Å), 2) stellar mass surface densities (upper right), 3) ages (lower right), 4) narrow band images (bottom center; emission lines: H α , [N II] 6584 Å, and [O III] 5007 Å), 5) H α emission (lower left) and 6) H α kinematics (upper left). The CALIFA logo is placed at the central hexagon.

sitivity curve by averaging the sensitivity curves measured independently for each galaxy. We anticipate that the largest uncertainty in the relative spectrophotometry across the CALIFA wavelength range will be dominated by the unknown extinction curve at the time of each observation.

The current pipeline also implements a new scheme for estimating the registration of the images. First, sky-subtracted and calibrated images are created from SDSS DR7 (in the r -band for the V500 setup and the g -band for the V1200) based on the so-called “corrected frames” (fpC). Then, the magnitude in the

corresponding SDSS filter is computed for each RSS spectrum. The predicted SDSS flux for each CALIFA fiber is estimated using 2''7 diameter apertures, adopting the PPAk layout projected on the SDSS image. This layout is displaced in steps in RA and Dec across a search box in the SDSS image. Then a χ^2 map is computed to obtain the best offsets for each pointing, taking into account errors in the flux measurements (only fibers with $S/N > 3.0$ are considered) and allowing for a photometric scaling factor between the SDSS and the CALIFA observations as an additional parameter. The minimum value of the χ^2 map is

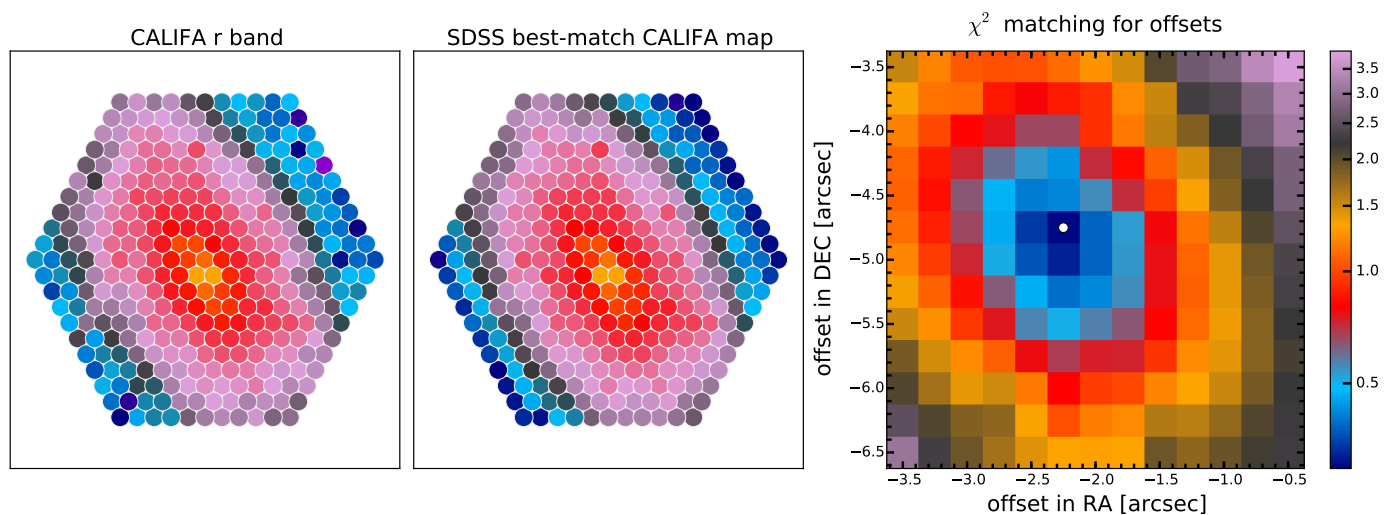


Fig. 9. Example of the registering method for pointing 1 of NGC0496 (ID 45). *Left panel:* Flux map in r -band for the PPak fibers. *Central panel:* Predicted SDSS flux for each CALIFA fiber estimated using $2.7''$ diameter apertures and adopting the PPak layout projected on the SDSS image for the best match according to the χ^2 map. Note that the PPak layout is not to scale, i.e. relative distances between adjacent fibers have been decreased for the sake of clarity. *Right panel:* χ^2 map of the offsets (best offset marked with a white dot).

used to obtain the best-fitting RA and Dec for the center of the PPak IFU with respect to the center of the CALIFA galaxy seen by SDSS. Figure 9 shows an example of the described procedure. The photometric scale factor at the best matching position is used to rescale the absolute photometry of each particular RSS pointing to bring them on the same flux scale.

The photometric anchoring to the SDSS images of the V1.5 data is more accurate than those of the previous version. However, there are a few datacubes where the new registering method does not return optimal results, particularly in low surface brightness edge-on galaxies or in the presence of bright foreground field stars. This effect is more likely to occur in the V1200 setup, given its lower S/N on average compared to V500. In such cases, we apply the photometric SDSS matching of pipeline V1.3c described in H13 (to both setups, for the sake of consistency). A new “REGISTER” keyword has been included in the header of the datacubes (see Sect. 4.4) and a dagger symbol has been added to the quality tables (Table 6 and 7) in order to easily identify these galaxies.

The third step in the reduction sequence is the interpolation method used to convert from RSS to cube format, aimed at improving the spatial resolution. We use the position of each RSS pointing obtained in the previous step for the image reconstruction. In a series of tests, we found that an inverse-distance weighted image reconstruction scheme performs more favorably than, e.g. the drizzle method (Fruchter & Hook 2002). In order to increase the spatial resolution and reduce the correlation between nearby pixels, we have reduced the extent of the Gaussian kernel for the interpolation. We adopt $0.75''$ for the dispersion of the Gaussian (instead of $1''$ in V1.3c) and limit the kernel to a radius of $3.5''$ (instead of $5''$). This results in a much sharper image and a lower value for the correlated noise. In the previous pipeline V1.3c, a minimum number of 3 fibers was imposed in the reconstruction of the image to achieve a homogeneous data quality across the field. With the new maximum radius in pipeline V1.5, such prescription results in the absence of data in the outer $2''$ of the FoV, due to the wider fiber separation in the outer ring of the fiber bundle. Thus, we decided to lower this limit to 1 as the minimum number of fibers needed to fill a spaxel. We have added a new Header Data Unit (see Sect. 4.3)

that records the number of fibers used to compute the total flux per spaxel. This allows the user to control what spaxels to include if a particular science case requires a minimum number of fibers for the reconstruction of the flux.

3.2. Characterization of spatially correlated noise

Due to the interpolation procedure to obtain a regular grid, the output pixels in the final datacube are not independent of one another. The gaussian interpolation method distributes the flux from a given fiber between several pixels which are combined with neighboring pixels within a certain radius, as described in Sect. 3.1. This causes the noise in the adjacent pixels to be correlated (in the spatial dimension). The correlation implies that a measurement of the noise in a stacked spectrum of N pixels will be underestimated (noise is underestimated on scales larger than pixel units). Characterizing this effect is essential for estimating the statistical errors when spectra in datacubes are co-added to increase the S/N, a common approach in specific applications when a minimum S/N is required.

First of all, it is important to check that the error spectra derived from the pipeline for individual spaxels are reliable. Spectral fitting analysis can provide an approximate assessment of the accuracy of the error spectra. In Fig. 10 we update figure 9 of H13 to DR2 data. The plot shows the histogram of reduced residuals, i.e. the difference between the observed (O_λ) and synthetic (M_λ) spectra obtained with STARLIGHT in units of the corresponding error ϵ_λ (details on the fitting procedures can be found in 5.5). The distribution is very well described by a Gaussian centered at 0.03 with $\sigma = 0.87$, only slightly less than expected if residuals are purely due to noise.

The correlated noise can be taken into account by providing the spatial covariance (Sharp et al. 2014). However, a more practical approach consists of using the datacubes to calculate the expected rms noise, with the noise correlation ratio $\beta(N)$, as a function of the number of pixels. To obtain a sample of co-added spaxels with different areas, we have used the Voronoi adaptive binning method (implemented for optical IFS data by Cappellari & Copin 2003) with a target S/N of 20. We have removed from the analysis individual spaxels with $S/N < 5$ and co-added bins

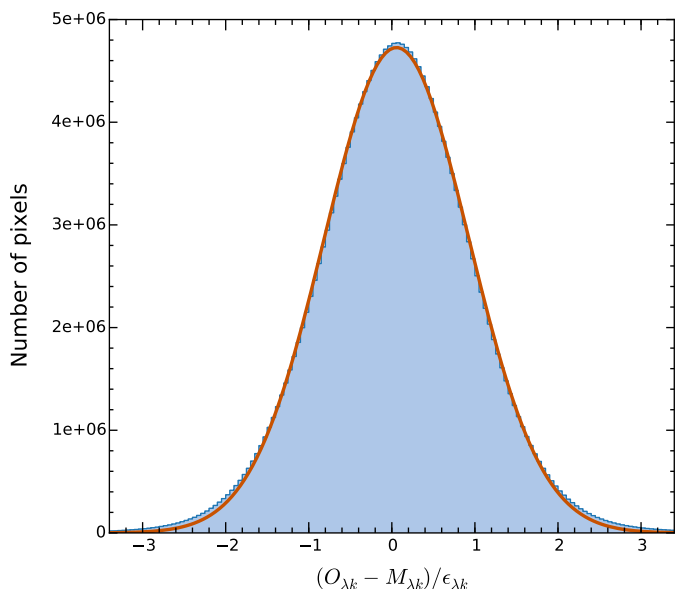


Fig. 10. Histogram of the reduced residuals $(O_{\lambda k} - M_{\lambda k})/\epsilon_{\lambda k}$ for all λ 's, all bins (k) and all galaxies in DR2 (209151086 points in total). The solid orange line shows the best Gaussian fit to the sample.

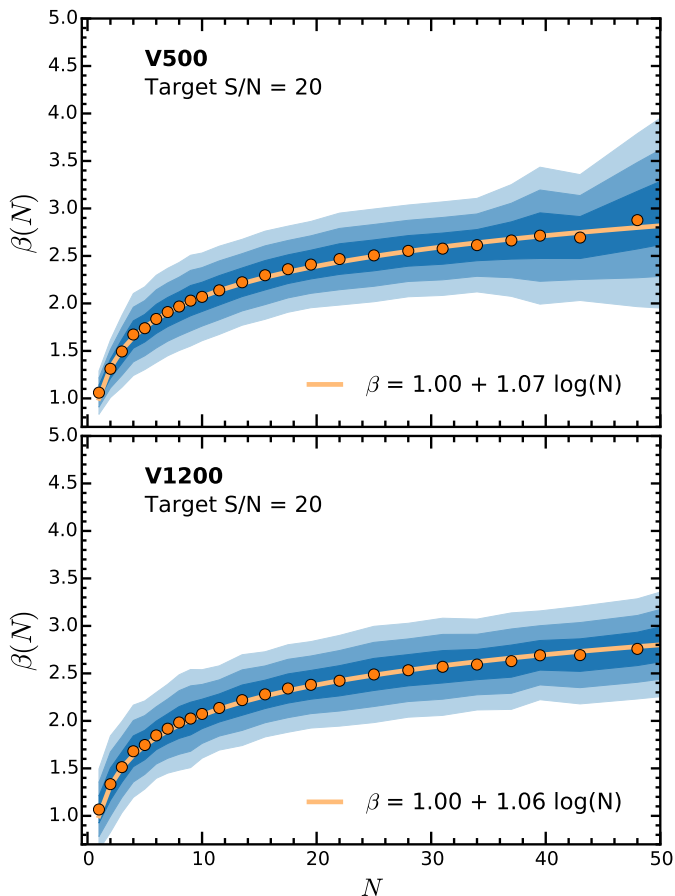


Fig. 11. Noise correlation ratio β (ratio of the real estimated error to the analytically propagated error) as a function of number of spaxels per bin for all the V500 (upper panel) and V1200 (lower panel) data of DR2 at a target S/N of 20. Shaded areas mark the 1σ , 2σ and 3σ levels. The orange lines represent the best fit logarithmic function with a slope $\alpha = 1.07$ and $\alpha = 1.06$, respectively.

Table 3. Dimension and sampling of CALIFA datacubes

Setup	N_α^a	N_δ^a	N_λ^a	λ_{start}^b	λ_{end}^c	d_λ^d	δ_λ^e
V500	78	73	1877	3749Å	7501Å	2.0Å	6.0Å
V1200	78	73	1701	3650Å	4840Å	0.7Å	2.3Å

Notes. ^(a) Number of pixels in each dimension. ^(b) Wavelength of the first pixel on the wavelength direction. ^(c) Wavelength of the last pixel on the wavelength direction. ^(d) Wavelength sampling per pixel. ^(e) Homogenized spectral resolution (FWHM) over the entire wavelength range.

with areas larger than 60 spaxels. The β correlation ratio (or correction factor) is the ratio of the “real” or measured error to the analytically propagated error of the binned spectra as a function of bin size. The results obtained for all DR2 datacubes, shown in Fig. 11, can be well described by the logarithmic function

$$\beta(N) = 1 + \alpha \log N, \quad (1)$$

with N the number of spaxels per bin.

The values for the slope α are equal within the errors (0.01) in both setups, with a value of 1.06 for V1200 and 1.07 for V500. The slope is lower than the DR1 value (mean ~ 1.4), indicating that the noise in DR2 datacubes is less correlated than in DR1. This is expected since we changed the parameters in the interpolation (reducing the number of adjacent fibers contributing to a particular spaxel) and the registering method. In Appendix A we give some instructions on how to estimate the final co-added error spectrum and the limit of the application of equation 1.

4. CALIFA data format and characteristics

The CALIFA data are stored and distributed as datacubes (three-dimensional data) in the standard binary FITS format and consist of several FITS Header Data Units (HDU). These datacubes contain (1) the measured flux densities, corrected for Galactic extinction as described in S12, in units of $10^{-16} \text{ erg s}^{-1} \text{ cm}^{-2} \text{ \AA}^{-1}$ (primary datacube), (2) associated errors, (3) error weighting factors, (4) bad pixels flags and (5) fiber coverage (Table 2). The last HDU is a new added content absent in DR1, as explained in Sect. 3.1, but the others share the same properties as the previous data release. The first two axes of the cubes correspond to the spatial dimension along right ascension and declination with a $1'' \times 1''$ sampling. The third dimension represents the wavelength and is linearly sampled. Table 3 summarizes the dimensions of each datacube (N_α , N_δ , and N_λ), as well as the spectral sampling (d_λ) and constant resolution (δ_λ) along the entire wavelength range.

4.1. Error and weight datacubes

The 1σ noise level of each pixel as formally propagated by the pipeline can be found in the first FITS extension. Sect. 3.2 discusses on the accuracy of the formal noise and the correlation, important when CALIFA data need to be spatially binned, and an empirical function is provided to account for the correlation effect. The second FITS extension (ERRWEIGHT) stores the error scaling factor for each pixel in the limiting case that all valid spaxels of the cube would be co-added (see also Appendix A). In the case of bad pixels, we assigned an error value that is roughly ten orders of magnitude higher than the typical value.

Table 2. CALIFA FITS file structure

HDU	Extension name	Format	Content
0	Primary	32-bit float	flux density in units of $10^{-16} \text{ erg s}^{-1} \text{ cm}^{-2} \text{ \AA}^{-1}$
1	ERROR	32-bit float	1σ error on the flux density
2	ERRWEIGHT	32-bit float	error weighting factor
3	BADPIX	8-bit integer	bad pixel flags (1=bad, 0=good)
4	FIBCOVER	8-bit integer	number of fibers used to fill each spaxel

4.2. Bad pixel datacubes

Bad pixel datacubes are stored in the third FITS extension (BADPIX). This information, in combination with the error vector, is essential to properly account for the potential problems in each spaxel. Pixels with flag = 1 reports the absence of sufficient information in the raw data due to cosmic rays, bad CCD columns or the effect of vignetting³. These bad pixels have been interpolated and we strongly suggest not to use them for any science analysis.

Finally, the uncovered corners of the hexagonal PPak FoV are filled with zeros and flagged as bad pixels for consistency. The residuals of bright night-sky emission lines are not flagged as bad pixels.

4.3. Fiber coverage datacubes

Pipeline V1.5 adds a new FITS extension (FIBCOVER) to the datacubes, not available in previous DR1 datacubes. As explained in Sect. 3.1 we have reduced the maximum distance of fibers that can contribute to the flux of a given spaxel. The outer hexagonal-ring of fibers do not have the same coverage in the surroundings as any other fiber inside the hexagon. In pipeline V1.3c we imposed a minimum of 3 fibers for computing the flux of given spaxel. In V1.5, with the new radius limit this would yield an empty outer hexagonal-ring of $\sim 2''$ in the FoV. Thus, we have relaxed to 1 the minimum number of fibers. In order to control which spaxels have enough flux “resolution”, we have included a new HDU reporting the number of fibers used to account for the computed flux.

4.4. FITS header information

The FITS header contains the standard keywords that encode the information required to transform the pixel-space coordinates into sky and wavelength-space coordinates, following the World Coordinate System (WCS, Greisen & Calabretta 2002). Each CALIFA datacube contains the full FITS header information of all raw frames from which it was created. Information regarding observing and instrumental conditions such as sky brightness, flexure offsets, Galactic extinction or approximate limiting magnitude is also kept in the FITS header of each datacube. See Sect. 4.3 of H13 for nomenclature and their Table 4 for a summary of the main header keywords and meaning.

The most important new keyword added in DR2 datacubes is “REGISTER” and takes a boolean value. It indicates if a particular datacube has been successfully registered using the new method explained in Sect. 3.1 (*True*) or it has used the old V1.3c scheme (*False*). Datacubes with a *False* value are marked with a dagger in Tables 6 and 7.

³ The vignetting effect imprints a characteristic inhomogeneous pattern across the FoV on the bad pixels vector. See Fig. 11 of H13 for more details.

5. Data Quality

This second CALIFA data release (DR2) provides science-grade data for a sample of 200 galaxies, including the 100 galaxies released in the first data release (DR1), identified by an asterisk in Tables 6 and 7. As for DR1, we have run a careful quality control (QC) on the data products and selected only those galaxies that passed a series of QC checks in both setups (V500 and V1200), as we detail in this section. The QC checks are based on a set of measured parameters and/or visual inspection, resulting in a set of flags that allow to quickly assess the quality of the data and their suitability for scientific use. Quantities and flags are organized into three distinct categories, respectively related to: observing conditions (denoted by the `obs` prefix); instrumental performance and effectiveness of the data reduction (`red`); accuracy and quality of the final data products (`cal`). The flags in each category are computed based on thresholds on measured quantities, possibly combined with flags given by human classifiers based on visual inspection, as detailed below and summarized in Tables 4 and 5. Thresholds are determined from the distribution of the parameters in order to exclude outliers and also by analyzing the effects of anomalous parameters on the final quality of the datacubes. The tables of the relevant QC parameters, along with the QC flags are available on the DR2 website.

Each flag can have one of the following values:

- `-1` = undefined
- `0` = good quality – OK
- `1` = minor issues that do not significantly affect the quality – WARNING
- `2` = significant issues affecting the quality – BAD

By selection, DR2 only includes galaxies with `WARNING` flags in the worst cases, with just a few minor exceptions affecting previously released DR1 galaxies: in these cases the revised QC criteria adopted here would have prevented to include such galaxies in the DR, but given the incremental nature of our data releases we keep them in the current sample.

In naming the QC parameters we adopt the following convention: the first part is the category prefix (`obs`, `red` or `cal`), followed by a measured parameter, and possibly a final suffix indicating the statistics applied to combine the parameter as measured in different observations/pointings/fibers (i.e., `MEAN`, `MIN`, `MAX`, `RMS`).

In the following subsections we describe the QCs in each of the above-mentioned categories. As mentioned in Sect. 3.1, the V1.5 pipeline starts after sky subtraction of the individual RSS files. Thus, some of the quality and properties of the DR2 datacubes are inherited from V1.3c and will not be discussed here, namely: wavelength calibration and sky subtraction.

5.1. Quality of the observing conditions (`obs`)

Three quantities are considered crucial in determining the quality of the observing conditions of the CALIFA data: the airmass,

Table 4. Definition of CALIFA DR2 quality control flags for the V500 data

QC flag	QC parameters involved	WARNING condition(s)	BAD condition(s)	Flag definition
FLAG_OBS_AM	OBS_AIRMASS_MEAN OBS_AIRMASS_MAX OBS_AIRMASS_RMS	> 1.7 > 2.0 > 0.15	> 2.0 > 2.5 ...	Worst of the three parameters
FLAG_OBS_SKYMAG	OBS_SKYMAG_MEAN OBS_SKYMAG_RMS	< 20.5 mag _V arcsec ⁻² > 0.1	< 19.5 ...	Worst of the two parameters
FLAG_OBS_EXT	OBS_EXT_MEAN OBS_EXT_MAX OBS_EXT_RMS	> 0.30 mag > 0.35 > 0.10	Worst of the three parameters
FLAG_RED_STRAYLIGHT	RED_MEANSTRAYLIGHT_MAX RED_MAXSTRAYLIGHT_MAX RED_RMSSTRAYLIGHT_MAX	> 30 counts > 50 > 5	> 50 > 100 > 10	Worst of the three parameters
FLAG_RED_DISP	RED_DISP_MEAN RED_DISP_MAX RED_DISP_RMS	> 5.5 Å (FWHM) > 10.0 > 0.5 > 1.0	Worst of the three parameters
FLAG_RED_CDISP	RED_CDISP_MEAN RED_CDISP_MAX RED_CDISP_RMS	> 3.0 pixels (FWHM) ≥ 4.0 > 0.25	Worst of the three parameters
FLAG_RED_SKYLINES	RED_RES5577_MIN RED_RES5577_MAX RED_RMSRES5577_MAX	< -0.1 counts > 0.1 > 1.0	Worst of the three parameters
FLAG_RED_LIMSB	RED_LIMSB	< 23.25 mag _V arcsec ⁻²	< 22.50	
FLAG_CAL_SPECPHOTO	CAL_QFLUX_G CAL_QFLUX_R CAL_QFLUX_RMS	> 0.06 dex < -0.06 dex > 0.06 dex < -0.06 dex > 0.1	> 0.097 dex < -0.097 dex > 0.097 dex < -0.097 dex > 0.2	Worst of the three parameters combined with visual checks on the 30"-integrated spectrum: spectral shape and comparison with SDSS photometry
FLAG_CAL_WL	CAL_RMSVELMEAN	> 2.0 km s ⁻¹	> 5.0	
FLAG_CAL_IMA	CAL_CHI2REG_MAX	> 10	...	Combine parameter and visual inspection on registration and synthetic broad-band image

the brightness of the sky, and the atmospheric extinction. While seeing is in general an important parameter of the observing conditions, the imaging quality and spatial resolution of the CALIFA cubes is mostly limited by the sampling of the fibers on the plane of the sky and the resampling process (see section 5.4.1 for more detail), rather than by the seeing. Moreover, the seeing measurement is only available for a small fraction of the objects (see Sect. 5.4.2), and therefore cannot be used as a reliable QC parameter.

For the airmass we consider the average and the maximum airmass of the observations over all pointings (OBS_AIRMASS_MEAN and OBS_AIRMASS_MAX) and its rms (OBS_AIRMASS_RMS). For each of these quantities we defined two thresholds (the same for V500 and V1200, see Table 6 and 7) above which the WARNING or the BAD flags, respectively, are

raised. The combined FLAG_OBS_AM is the worst of the three cases.

The surface brightness of the sky in V-band during the observations is another critical parameter, which mainly limits the depth of the observations and the accuracy of the sky subtraction. The quantity SKYMAG is measured in each pointing from the sky spectrum obtained from the 36 sky fibers⁴. The mean and the rms over all pointings are considered to define the corresponding flags. Note that stricter requirements are applied to V1200 data (blue setup, high resolution) with respect to the V500 ones.

The transparency of the sky during each pointing (EXT) is obtained from the monitored V band extinction at the time of the observation. We consider as symptoms of low/bad quality obser-

⁴ See Appendix A.8 of H13.

Table 5. Definition of CALIFA DR2 quality control flags for the V1200 data

QC flag	QC parameters involved	WARNING condition(s)	BAD condition(s)	Flag definition
FLAG_OBS_AM	OBS_AIRMASS_MEAN OBS_AIRMASS_MAX OBS_AIRMASS_RMS	> 1.7 > 2.0 > 0.15	> 2.0 > 2.5 ...	Worst of the three parameters
FLAG_OBS_SKYMAG	OBS_SKYMAG_MEAN OBS_SKYMAG_RMS	< 21.5 mag _V arcsec ⁻² > 0.1	< 21.0 ...	Worst of the two parameters
FLAG_OBS_EXT	OBS_EXT_MEAN OBS_EXT_MAX OBS_EXT_RMS	> 0.30 mag > 0.35 > 0.10	Worst of the three parameters
FLAG_RED_STRAYLIGHT	RED_MEANSTRAYLIGHT_MAX RED_MAXSTRAYLIGHT_MAX RED_RMSSTRAYLIGHT_MAX	> 15 counts > 20 > 1.5	> 30 > 40 > 2.0	Worst of the three parameters
FLAG_RED_DISP	RED_DISP_MEAN RED_DISP_MAX RED_DISP_RMS	> 2.0 Å (FWHM) > 10.0 > 0.15	> 2.5	Worst of the three parameters
FLAG_RED_CDISP	RED_CDISP_MEAN RED_CDISP_RMS	> 3.0 pixels (FWHM) > 0.66	Worst of the two parameters
FLAG_RED_SKYLINES	RED_RES4358_MIN RED_RES4358_MAX RED_RMSRES4358_MAX	< -0.1 counts > 0.1 > 0.7	Worst of the three parameters
FLAG_RED_LIMSB	RED_LIMSB	< 22.50 mag _B arcsec ⁻²	< 22.00	
FLAG_CAL_SPECPHOTO				Visual checks on 30"-aperture integrated spectrum for spectral shape and mismatch with V500 spectrophotometry
FLAG_CAL_WL	CAL_RMSVELMEAN	> 1.0 km s ⁻¹	> 2.0	
FLAG_CAL_IMA	CAL_CHI2REG_MAX	> 10	...	Combined parameter of visual inspection on registration and synthetic broad-band image

vations large extinctions on average, a large maximum extinction or a large rms variation across the pointings (indicating inhomogeneous observing conditions).

5.2. Quality of the instrumental/data reduction performance (RED)

The quality of the instrumental and data reduction performance is assessed via a series of four quantities measured on the reduced data *before* combining them into the final datacube: STRAYLIGHT, spectral DISPERSION, cross dispersion CDISP, and the residuals from the subtraction of bright skylines (namely, the 5577Å O₂ line in the V500 setup and the 4358Å HgI in the V1200 setup). In addition we consider the limiting surface brightness corresponding to a 3-σ detection measured on the final cube.

The so-called straylight is an additional source of illumination internal to the instrument, possibly as a distributed scattered light component. Straylight, if not subtracted properly, introduces systematic errors and thus limits the final sensitivity and accuracy of the data reduction⁵. High mean level of straylight in a frame (MEANSTRAYLIGHT), as well as high maximum values (MAXSTRAYLIGHT) and large rms (RMSSTRAYLIGHT), are indication of poor performance. Levels above the thresholds provided in Tables 4 and 5 in at least one of the exposures (_MAX suffix) raise a WARNING or a BAD FLAG_RED_STRAYLIGHT flag.

The spectral dispersion and cross dispersion are measured on individual fiber spectra as the FWHM of skylines and the FWHM of the spectral trace, respectively. Thresholds are set on the mean values to ensure that the typical parameters do not de-

⁵ For a detailed description on the straylight subtraction, see Appendix A.3 of H13.

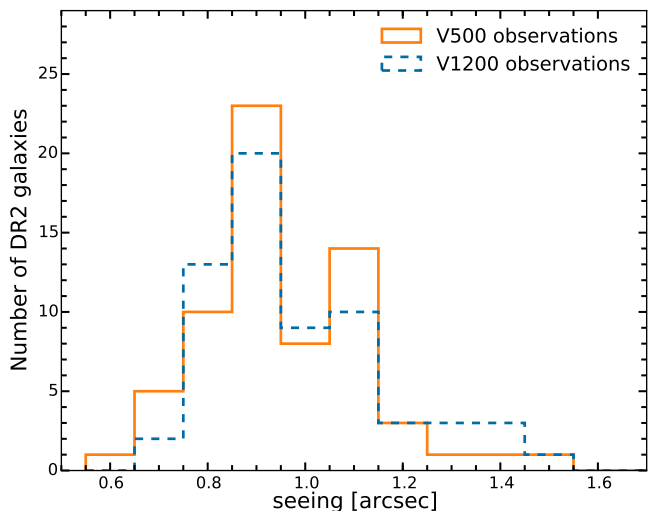


Fig. 12. Distribution of the seeing during the CALIFA observations as measured by the automatic Differential Image Motion Monitor (DIMM, Aceituno 2004).

part too much from the nominal target specifications, and on the maximum and rms in order to check for anomalies in the data. Any failure to comply within the thresholds reported in Tables 4 and 5 raises a FLAG_RED_DISP or FLAG_RED_CDISP.

In order to assess the performance of the sky subtraction we consider the minimum and the maximum over all pointings of the average (over all fibers) flux residual of a bright skyline within an individual pointing (RED_RES4358_MIN and RED_RES4358_MAX, and RED_RES5577_MIN and RED_RES5577_MAX for the V1200 and the V500 setup respectively). We also consider the maximum over all pointings of the rms residuals (over all fibers in an individual pointing), RED_RMSRES4358_MAX and RED_RMSRES5577_MAX. Too negative or too positive average residuals are indication of systematic bias in the sky subtraction. Too large rms can be regarded as symptom of localized failures or noisy data. In these cases the FLAG_RED_SKYLINES is set.

Finally, the 3σ continuum flux density detection limit per interpolated 1 arcsec²-spaxel for the faintest regions is used to identify cubes whose depth does not fulfil the survey requirements and this is reflected in the FLAG_RED_LIMSB flag. More about the depth of the final datacubes is discussed in Sec. 5.6.

5.3. Quality of the calibrated data products (CAL)

The quality of the calibrated data products is determined by checks on the global spectrophotometry, on the stability of the wavelength calibration across the spectral range, and on the quality of the resulting 2D flux distribution (synthetic image) and its ability to match the SDSS broad-band imaging.

The quality of global spectrophotometric calibration is assessed by comparing the photometric fluxes derived from spectra integrated within 30''-radius apertures with the corresponding fluxes derived from SDSS imaging, as explained below in Sec. 5.5. For the V500 setup, in particular, it is possible to derive the flux ratio between SDSS and CALIFA in *g* and *r*-band (CAL_QFLUX_G and CAL_QFLUX_R, respectively, averaged over all pointings for a given galaxy): values of these ratios departing from 1 by more than the tolerances listed in Table 4 are flagged. Large rms variations of these values over the three V500 pointings (CAL_QFLUX_RMS, which combines *g* and *r* bands) are also

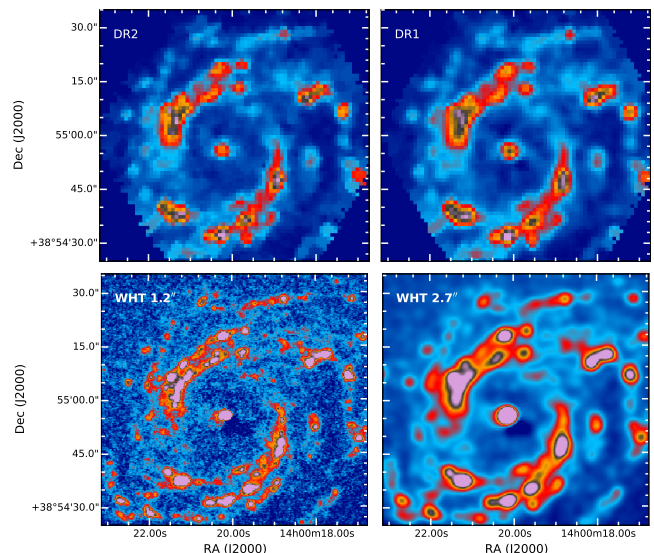


Fig. 13. DR2 spatial resolution comparison for NGC 5406 (ID 684). The upper left panel shows the DR2 image of the H α map and the upper right the DR1 one. The lower row are H α images taken with the 4.2m William Herschel Telescope (Roque de los Muchachos Observatory, La Palma, Spain), using the AUXCAM detector (Sánchez-Menguiano et al., in prep.). The image, with an original resolution of 1.2'' (bottom left), has been degraded to a resolution of 2.7'' (bottom right) and the FoV has been reduced to match exactly the same WCS coordinates as CALIFA.

considered symptoms of poor quality. In addition to these quantitative parameters, we visually check that the spectral energy distribution (SED) measured via SDSS photometry matches the CALIFA integrated spectrum. For this check we also consider the *u* and the *i* band data-points: although the CALIFA spectra do not cover the full extent of these pass-bands, they prove helpful in judging the matching of spectral shapes. Five members of the collaboration have performed these checks independently and assigned flags OK-WARNING-BAD: the second-to-worst classification is retained. This flag is then combined with the flags based on the quantitative flux ratios to create the final FLAG_CAL_SPECPHOTO flag.

In order to check the stability of the wavelength calibration over the full spectral range we performed the same measurements presented in Sec. 5.3 of H13: for each galaxy and setup, the spectra within 5'' of the center of the galaxy are integrated and the systemic velocity is estimated first for the full spectrum and then for 3 (4) independent spectral ranges in V1200 (V500); the rms of these values with respect to the systemic velocity from the full spectrum (CAL_RMSVELMEAN) is an estimate of the stability of the wavelength calibration across the wavelength range and is used to set the corresponding quality flag FLAG_CAL_WL. In > 97.5% of the cases we obtain CAL_RMSVELMEAN well below 2 km sec⁻¹ for the V1200 and 3 km sec⁻¹ for the V500 grating.

Finally, the quality flag on the 2D flux distribution and plane-of-sky registration, FLAG_CAL_IMA, is defined by combining the information on the goodness of matching between SDSS images and synthetic images from the CALIFA datacube and a series of visual checks. The former piece of information is provided by the chi-squared of the registration procedure (see Sect. 3.1). The visual checks include: a check on possible artefacts in the synthetic broad band image from the final CALIFA cubes (e.g. mismatched features, elongated PSF); a comparison of the CALIFA fiber footprints of each pointing with the registered SDSS im-

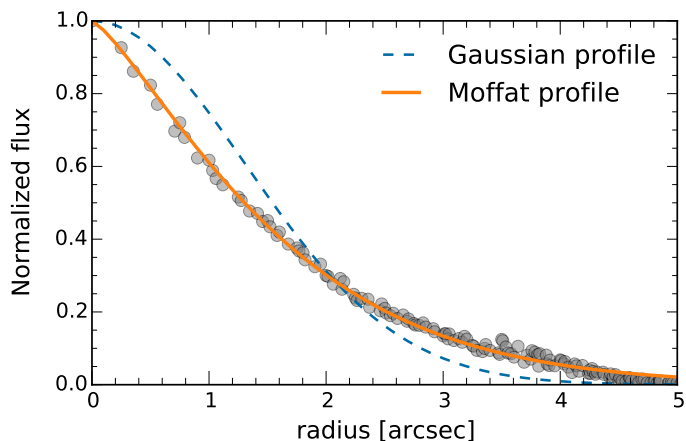


Fig. 14. Profile fit to a foreground star close to the center in the data cube of the galaxy NGC 2916. When the PSF is good, a Moffat function fits the data better than a Gaussian.

age, looking for apparent mismatched and miscomputed spatial offsets; a check of the chi-squared surface plot displaying the dependence of the registration procedure (see below) on the x and y spatial offsets, whereby irregular chi-square surfaces and lacks of clear minimum likely imply the impossibility of an accurate registration. Out of five independent classifiers we chose the median value of the attributed flags and combine it with the flag corresponding to the chi-squared measurements. We note that a small number of objects already released as part of DR1 do not reach the imaging quality standards using the registration procedure adopted in the pipeline V1.5 (see Sect. 3.1), which uses cross-correlation with SDSS images: in these cases we revert to the old registration scheme adopted for DR1 (pipeline V1.3c) and mark the objects with a dagger in Tables 6 and 7.

5.4. Astrometric accuracy and spatial resolution

5.4.1. Astrometric registration accuracy

Pipeline V1.5 implements a new method (see Sect. 3.1) to register the absolute astrometry of the datacube coordinate system to the International Coordinate Reference System (ICRS). The previous pipeline, V1.3c, used tabulated coordinates of the galaxy V band photometric center that were assigned to the barycenter measured in the reconstructed image from the datacubes (just one point, instead of the global match applied in V1.5).

In order to check the accuracy of the new astrometric registration for V500 and V1200 datacubes, we performed independent tests using SDSS r and g -band images (DR10) for each galaxy. Synthetic r and g -band PPAK images were computed using the V1.5 reduced data. The coordinates of the peak centroid PPAK images are used as an approximate galactic center, and the corresponding peak was measured in the SDSS images. The offsets between the SDSS and CALIFA are less than $3''$ (rms $\sim 1''$) for the majority of the DR2 sample. Large offsets are mostly due either to edge-on galaxies, centers of the galaxies not well defined due to dust lanes, irregular morphology or bright field star(s) near the center of the galaxy. Objects with offsets larger than $3''$ measured in V500 setup are: IC1652, NGC0444, UGC00809, UGC00841, NGC0477, IC1683, NGC0499, NGC0496, NGC0528, UGC01938, NGC1056, NGC3991, MCG-01-01-012 and NGC7800. For the V1200 setup: IC1528, IC1652, NGC0444, UGC00809, UGC00841,

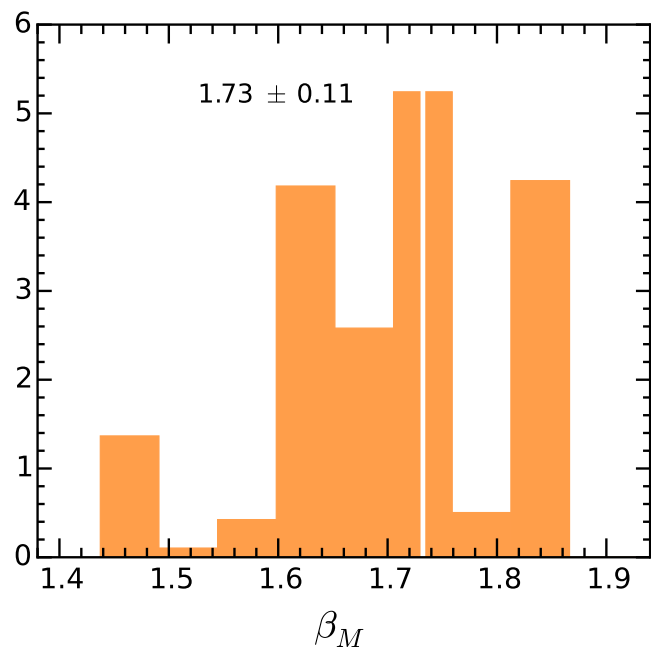
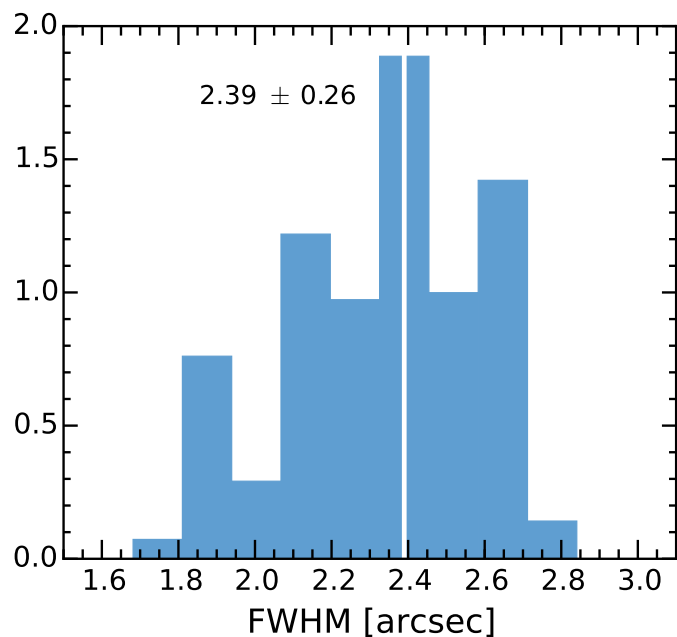


Fig. 15. Normalized Distribution of PSF FWHM (*top*) and β_M (*bottom*) parameters of a 2-d Moffat profile fitted to 45 calibration stars, weighted by the likelihood of the fit. The mean value of the distributions are marked with a white solid line.

NGC0477, NGC0499, NGC0496, NGC0528, UGC02222, NGC3991, UGC11792, MCG-01-01-012 and NGC7800.

5.4.2. Seeing and spatial resolution

In order to cover the complete FoV of the central bundle and to increase the final resolution of the CALIFA datacubes (PPAK fibers have a diameter of $2.7''$), a dithering scheme with three pointings has been adopted, as described in S12. In imaging, in addition to the telescope aperture, instrumental and atmospheric

seeing determine the final spatial resolution. This has to be added to the IFU particular characteristics.

The average atmospheric seeing conditions along the time of the observation of the CALIFA data were derived from the measurements acquired by the DIMM (DIMM, [Aceituno 2004](#)), which operates fully automatically at the Calar Alto observatory during the night. DIMM has different operational constraints (humidity lower than 80% and wind speed less than 12 m s^{-1}) than the 3.5m telescope, thus seeing information is not available for every CALIFA observation. Thus, there can be some DIMM seeing values missing from Tables 6 and 7, but the overall seeing distribution is not expected to be very different. Figure 12 shows the DIMM seeing distribution for the DR2 sample, which has a median value of $0''.9$ FWHM (the distribution is very similar to the DR1 sample), and therefore atmospheric seeing is not a limiting factor in the spatial resolution of the CALIFA cubes.

Another improvement of the pipeline, as discussed 3.1, is the spatial resolution. Fig. 13 shows $H\alpha$ maps (obtained using FIT3D on the CALIFA datacubes) for NGC 5406 (ID 684) for DR1, DR2 and one image taken with the William Herschel Telescope (WHT) using a narrowband filter. The last image has been also degraded to the DR2 nominal resolution for the sake of comparison. This improvement impacts directly, for example, onto the detection rate of $H\text{ II}$ regions. Using HIIEXPLORER ([Sánchez et al. 2012b](#)) on the V1.3c datacubes of the 200 galaxies, a total of 5878 are recovered, while this number rises to 7646 $H\text{ II}$ regions for the DR2 galaxies using pipeline V1.5, which represents an increase of $\sim 30\%$.

We follow two different approaches to measure the PSF in the datacubes. In those cases where a bright foreground star is present not far from the center, a fit is performed to the radial distribution of the star light profile. When the PSF is good, a Moffat function yields a better fit than the Gaussian, as shown in Fig. 14. This method can only be applied to a few galaxies, usually with stars being far from the center of the images, by construction of the survey.

Since January 2012 standard stars were observed using the same dithering pattern adopted for the science observations for the V500 setup. We observed a total of 107 nights in this period. Only 70% of the nights had weather conditions good enough to acquire a calibration star and $2/3$ were observed adopting the dithering scheme, yielding a total of 45 datacubes. We reduced the data using the same procedure described before for the science objects. As the calibration stars have a very high S/N, the PSF can be measured very precisely. From the datacubes we simulate a SDSS g -band image for each of these stars. For each of these images we fit a 2-d Moffat profile using the software IMFIT ([Erwin 2014](#))⁶. Figure 15 shows the normalized distributions of FWHM and β_M parameters of the Moffat profile, weighted by the likelihood of the fit. We obtain a mean value of the FWHM = 2.39 ± 0.26 arcsec, with $\beta_M = 1.73 \pm 0.11$. We also measure an ellipticity ($1 - b/a$, with a and b being the semi-major and semi-minor axes, respectively) of 0.08 ± 0.06 . Given the uncertainties, this means the PSF can be considered effectively axisymmetric. The uncertainties in these measurements correspond to $1-\sigma$ of the distributions.

The second method is based on the fact that the nuclei of galaxies have a relatively steep luminosity profile, and we take advantage of the good quality of the SDSS images. For each galaxy, the SDSS r -band image is convolved with a 2D function (Moffat or Gaussian) and we compute the residuals after subtracting the resulting flux radial distribution from the flux ra-

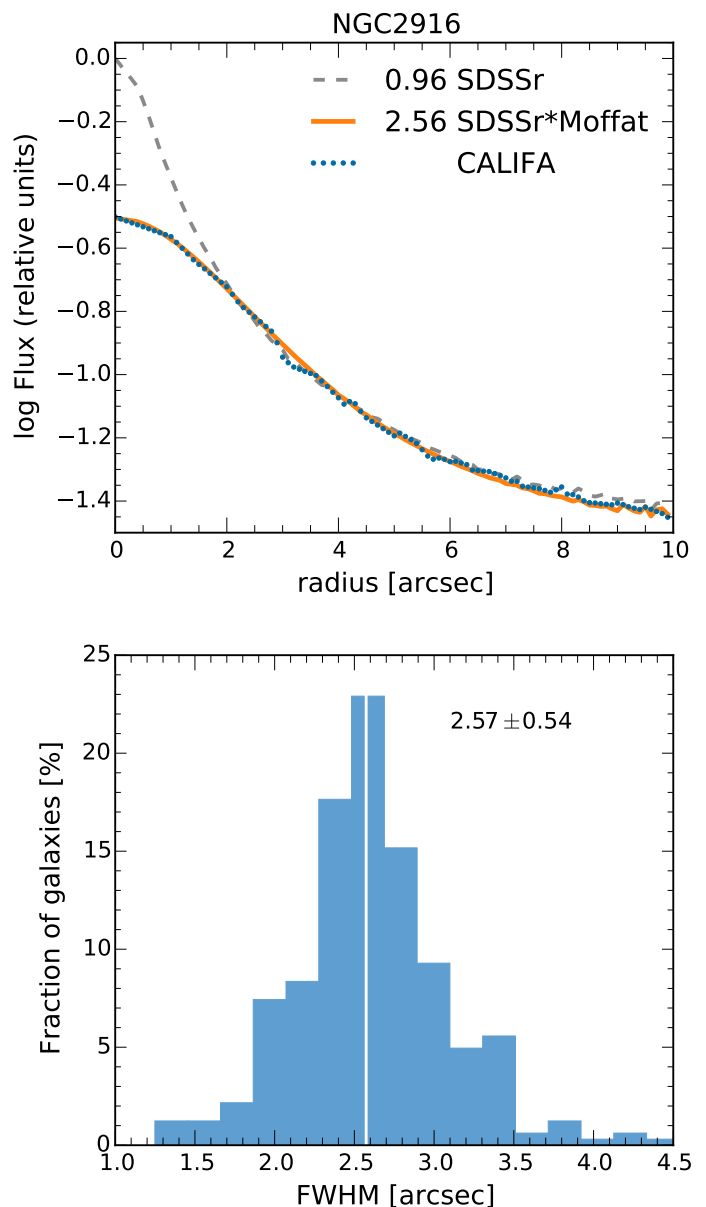


Fig. 16. *Top panel:* The dashed (grey) line is the flux profile of the galaxy NGC 2916 from the original SDSS r -band image, with a PSF FWHM = $0''.96$ (as obtained from the SDSS Skyserver), the dotted (blue) line is the flux profile from the CALIFA datacube of NGC 2916, and the solid (orange) line is the profile from the convolution of the SDSS r image with a 2D Moffat kernel of width $2''.37$, resulting in a final PSF FWHM = $2''.56$. *Bottom panel:* Distribution of FWHM obtained for all galaxies when convolving SDSS r images with a Moffat kernel, with values around 2.57 ± 0.54 arcsec (white line).

dial distribution of the datacube of the same galaxy. A range of FWHM for the convolution function is used and we choose the one that minimizes the residuals. An example for the galaxy NGC 2916 is shown in the top panel of Fig. 16 for the case of convolving with a Moffat kernel. The dashed (grey) line is the flux profile of the original SDSS r -band image, with a PSF FWHM = $0''.96$ (as obtained from the SDSS Skyserver), the dotted (blue) line is the flux profile from the CALIFA datacube, and the continuous (orange) line is the convolution of the grey profile with a 2D Moffat kernel of width $2''.37$, resulting in a final PSF FWHM = $2''.56$. The *bottom panel* of Fig. 16 shows the

⁶ <http://www.mpe.mpg.de/~erwin/code/imfit/>

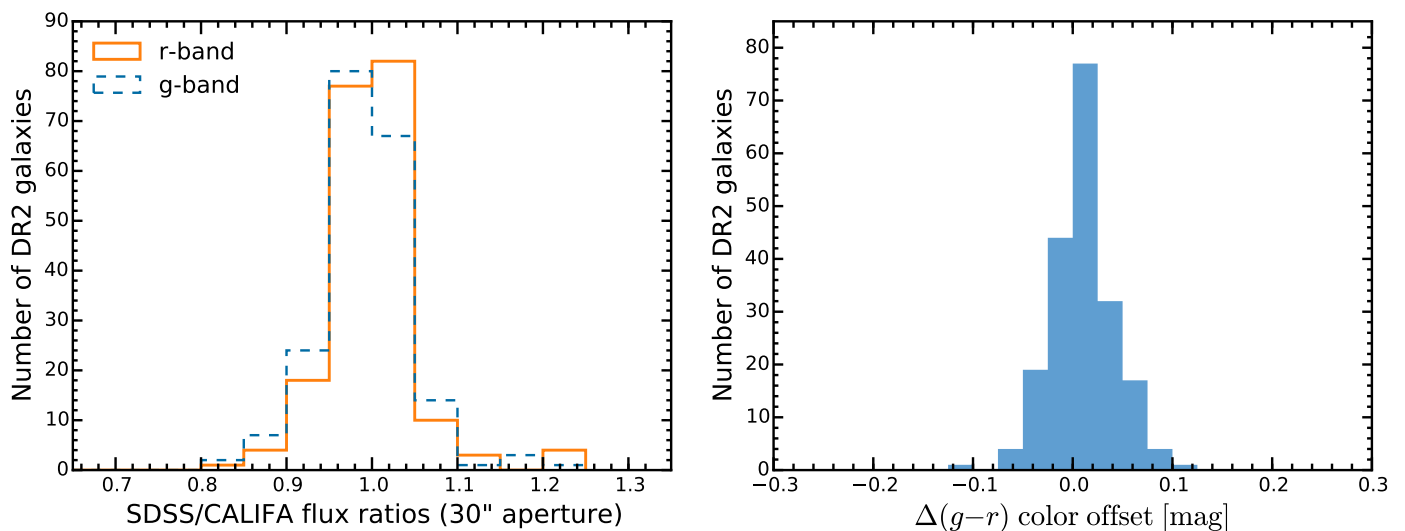


Fig. 17. *Left panel:* Distribution of the 30'' aperture photometry scale factor between the SDSS DR7 images and re-calibrated CALIFA data. We compare the photometry only for the g and r bands, which are both entirely covered by the V500 wavelength range. *Right panel:* Distribution of the corresponding color offset between the SDSS DR7 images and the synthetic CALIFA broad-band images.

distribution of FWHM obtained for all galaxies for the case of convolving with a Moffat kernel, with values around 2.57 ± 0.54 arcsec (white line).

Both methods, even though being from completely different natures, agree with each other in the value of FWHM. Thus, we conclude that a Moffat profile with $\text{FWHM} = 2.5''$ and $\beta_M = 1.7$ is a good description of the PSF of the datacubes in this data release.

5.5. Spectrophotometric accuracy

As mentioned in Sect. 3.1 the new registration scheme of the pipeline uses SDSS r -band for the V500 setup and g -band for the V1200, and field calibration images of the SDSS DR7. Each V500 datacube is rescaled in the absolute flux level to match the SDSS DR7 broad-band photometry using the photometric scale factor at the best matching position for each pointing. On the other hand, the V1200 data is matched to the V500 data (S12). This procedure, together with the new re-calibrated sensitivity curve (see Sect. 3.1 and Husemann et al., in preparation), improves the spectrophotometric calibration over DR1. This is clearly shown in Fig. 17. As part of the CALIFA pipeline V1.5, a 30'' diameter photometric aperture in r and g is measured both in the SDSS DR7 images and the equivalent synthetic CALIFA broad-band images. The mean SDSS/CALIFA g and r band ratios in DR2 are 1.00 ± 0.05 and 0.99 ± 0.06 , respectively. In the *right panel* of Fig. 17 the distribution in $\Delta(g-r)$ color difference between the SDSS and CALIFA data shows that the spectrophotometric accuracy across the wavelength range is better than 3%, with a median value of 0.01 ± 0.03 .

Spectral fitting methods can be used to perform useful tests of the data and their calibration, and this has been done before in CALIFA. H13 used STARLIGHT fits to evaluate the accuracy of the error estimates in DR1 datacubes, while Cid Fernandes et al. (2014) used such fits to map systematic features in the spectral residuals which may indicate calibration issues.

We have repeated the same experiments for the DR2 datacubes. Results are shown in Fig. 18. The top panel shows in blue the mean spectrum of 170670 Voronoi bins of the 200 galaxies in

DR2⁷. The average is done after normalizing each spectrum by its median flux in the $5635 \pm 45 \text{ \AA}$ window. The mean synthetic spectrum (overplotted orange line) as well as the mean residual (at the bottom of the upper panel, purple line) are also plotted. The middle panel zooms in on the residual spectrum, which now excludes emission lines and bad-pixels masked away in the fitting process. Finally, the bottom panel shows what fraction of all spectra was used in the statistics at each λ .

The layout of Fig. 18 is identical to figure 13 of Cid Fernandes et al. (2014), to which it should be compared⁸. Focusing on the middle panel, one sees that from $\sim 5000 \text{ \AA}$ to the red the residuals are very similar, including the humps around 5800 \AA , associated to imperfect removal of telluric features. Towards the blue however, the new reduction pipeline leads to smaller residuals. For instance, the broad feature around H β seen with V1.3c spectra is essentially gone with the new reduction. A systematic excess blueness persists for $\lambda < 3900 \text{ \AA}$, but overall the improvement is clear.

Residuals for the 200 DR2 nuclear spectra are shown in Fig. 19, where galaxies are sorted by redshift and piled up. This visualization facilitates the identification of telluric features, which appear as slanted lines in the image. Comparison with an identical plot in H13 (their Fig. 16) shows the improvements achieved with the new pipeline.

5.6. Limiting sensitivity and signal-to-noise

In order to assess the depth of the data, we estimated the 3σ continuum flux density detection limit per interpolated 1 arcsec^2 -spaxel for the faintest regions. Fig. 20 shows the limiting continuum sensitivity of the spectrophotometrically recalibrated CALIFA spectra. The depth is plotted against the average S/N per

⁷ The spatial binning is used to guarantee a minimum S/N of 20 in the continuum at $\sim 5635 \text{ \AA}$. In practice, 88% of the Voronoi bins actually comprise a single spaxel.

⁸ Fig. 13 in Cid Fernandes et al. (2014) is in fact busier than our Fig. 18, as it shows results obtained with three different spectral bases. Here we adopt the same base described in González Delgado et al. (2014b), which is very similar to base GM in Cid Fernandes et al. (2014).

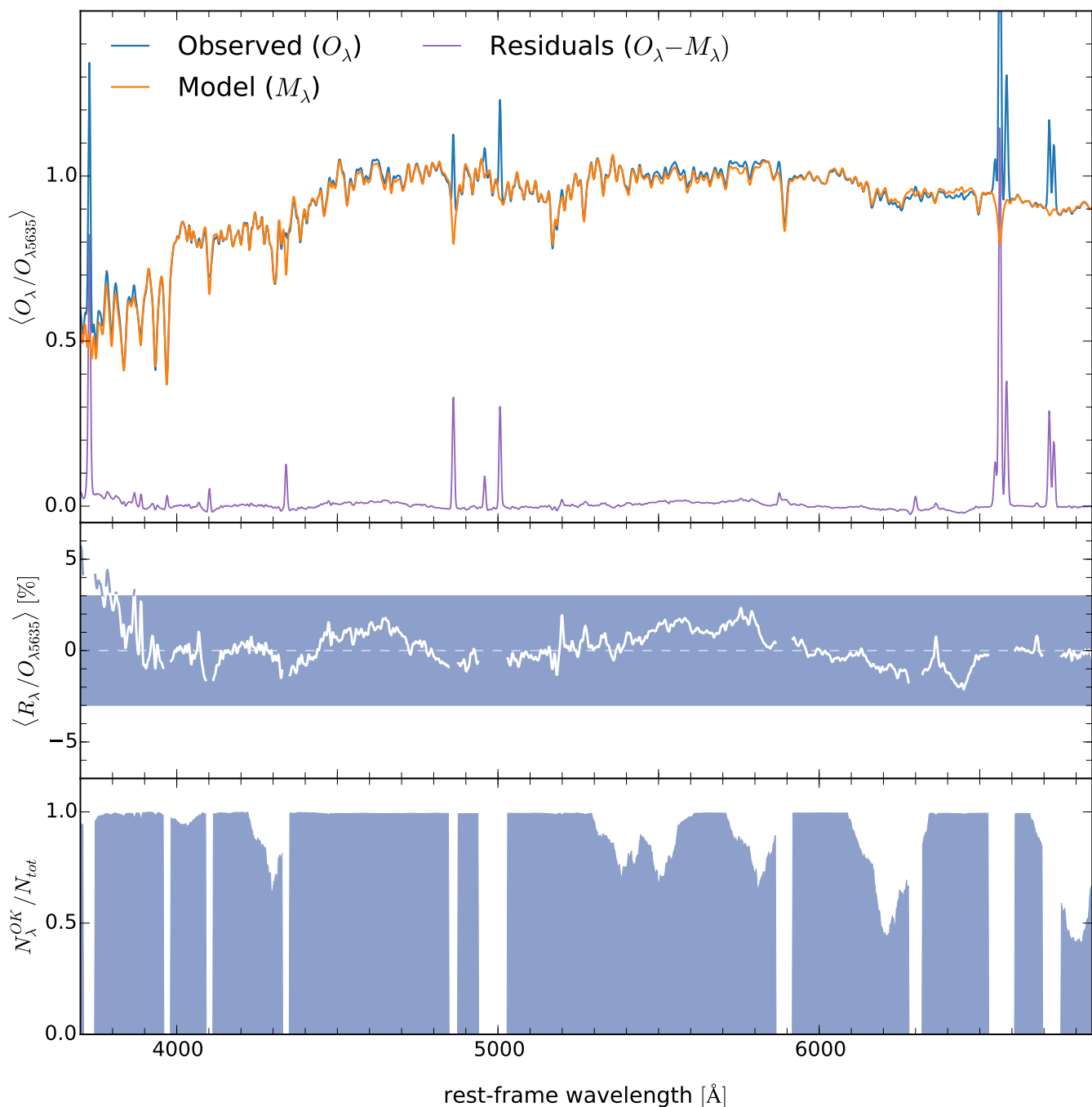


Fig. 18. Statistics of the spectral residuals (compare to Fig. 13 of Cid Fernandes et al. 2014). *Top:* The mean normalized spectrum of 170670 bins from 200 galaxies. The mean STARLIGHT fit is overplotted in orange, while the mean residual is plotted at the bottom of the panel (purple). *Middle:* Zoom of the residual spectrum, with emission lines removed for clarity. The shaded rectangle encompasses the $\pm 3\%$ area. *Bottom:* Fraction of the bins contributing to the statistics at each λ .

spectral resolution element within an elliptical annulus of $\pm 1''$ around the galaxies r -band half-light semi-major axis (HLR), with PA and radius values taken from W14. A narrow wavelength window at 4480–4520Å for the V1200 and at 5590–5680Å for the V500 was used to estimate both values. These small windows are nearly free of stellar absorption features or emission lines. The 3σ continuum flux density detection limit⁹ for the V1200 data ($I_{3\sigma} = 3.2 \times 10^{-18} \text{ erg s}^{-1} \text{ cm}^{-2} \text{ \AA}^{-1} \text{ arcsec}^{-2}$ in the median at 4500Å) is a factor of ~ 2 -3 brighter than for

the V500 data ($I_{3\sigma} = 1.2 \times 10^{-18} \text{ erg s}^{-1} \text{ cm}^{-2} \text{ \AA}^{-1} \text{ arcsec}^{-2}$ in the median at 5635Å) mainly due to the difference in spectral resolution. These continuum sensitivities can be transformed into equivalent limiting broad band surface brightnesses of 23.0 mag arcsec⁻² in the g -band for the V1200 data and 23.4 mag arcsec⁻² in the r -band for the V500. The variance of the sky brightness of each night might be one of the main factors of the dispersion in the limiting continuum sensitivity. Dust attenuation, transparency of the night, and other atmospheric conditions might also affect the achievable depth at fixed exposure times.

⁹ Note that this is a continuum flux density. See Note 5 of H13.

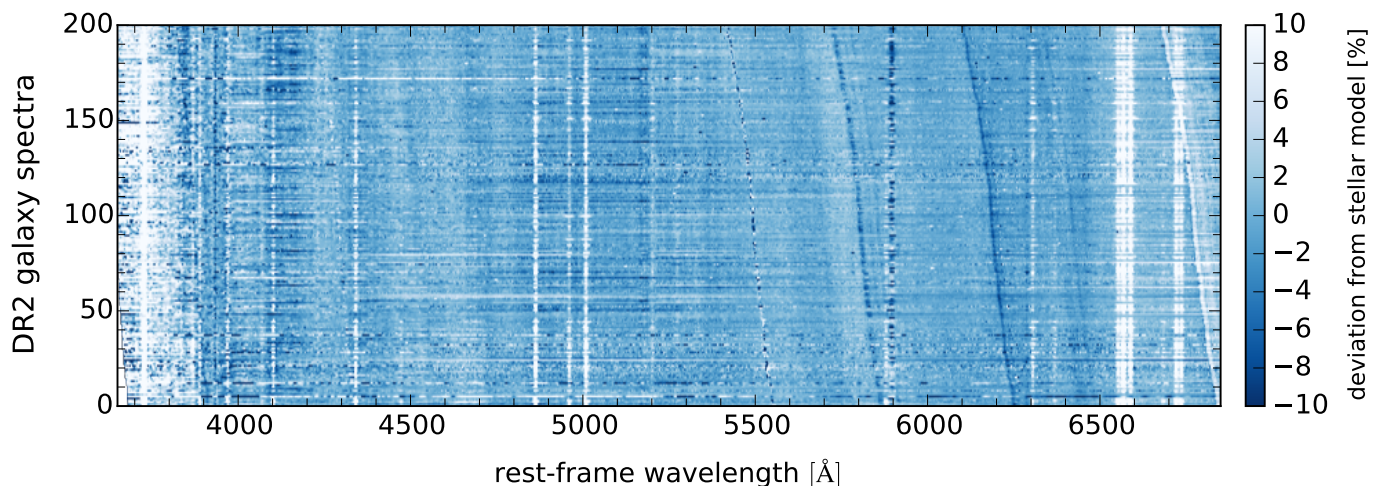


Fig. 19. Relative spectral deviations $-(O_\lambda - M_\lambda)/O_\lambda$, where O and M denote the observed and the model spectra, respectively—for the nuclear regions of all DR2 galaxies, vertically sorted by redshift. Unlike in Fig. 18, emission lines and bad-pixels are not masked in this plot. Systematic deviations from the STARLIGHT model appear as vertical stripes (rest-frame mismatches, e.g. imperfect stellar model or emission lines), while slanted stripes trace observed-frame mismatches (e.g. imperfect sky model). Compare to Fig. 16 of H13.

The limiting sensitivity is a measure of the noise and thus it correlates mildly with the S/N. The mean S/N in the continuum per spaxel at the half-light semi-major axis (HLR) of all objects is ~ 9.5 for the V1200 setup, while it is ~ 22.2 for the V500 data. Thus, we achieve a $S/N \gtrsim 10$ for a significant number of the objects even for the V1200 setup.

6. Access to the CALIFA DR2 data

6.1. The CALIFA DR2 search and retrieval tool

The public data is distributed through the CALIFA DR2 web page (<http://califa.caha.es/DR2>). A simple web form interface, already in use for the first data release, allows the user to select data of a particular target galaxy, or a subsample of objects within some constraints on observing conditions or galaxy properties. Among the selection parameters we include the instrument setup, galaxy coordinates, redshift, g -band magnitudes, observing date, Hubble type, bar strength, inclination estimated from axis ratio, V band atmospheric attenuation, airmass, and relative accuracy of the SDSS/CALIFA photometric calibration.

If any CALIFA datasets are available given the search parameters, they are listed in the following web page and can be selected to be downloaded. The download process requests a target directory on the local machine to store the data, after the downloading option was selected. The CALIFA data are delivered as fully reduced datacubes in FITS format separately for each of the two CALIFA spectral settings, i.e. the V500 and V1200 setup. Each DR2 dataset is uniquely identified by their file name, $GALNAME.V1200.rscube.fits.gz$ and $GALNAME.V500.rscube.fits.gz$ for the V1200 and V500 setup respectively, where $GALNAME$ is the name of the CALIFA galaxy listed in Table 1.

All the QC tables discussed along this article are also distributed in CSV and FITS-table formats in the same webpage. In addition, we distribute the more relevant tables discussed in W14 regarding the characterization of the MS, using similar formats. These tables could be useful in further science explorations of the cubes.

6.2. Virtual Observatory services

CALIFA data is also available through several Virtual Observatory (VO) facilities.

1. The FITS files of the full cubes are accessible through GAVO's ObsCore (Louys et al. 2011) service, which is part of the TAP (Dowler et al. 2011) service at <http://dc.g-vo.org/tap>. ObsCore provides a homogeneous description of observational data products of all kinds and thus allows global data set discovery. The system already supports the upcoming IVOA DataLink standard for performing cutouts and similar server-side operations.
2. At the same TAP endpoint, the `califadr2.cubes` and `califadr2.objects` tables allow queries versus CALIFA-specific metadata, in particular the quality control parameters given in Tables 6 and 7.
3. Individual, cut-out spectra can be located and retrieved from the CALIFA SSA service¹⁰; advanced SSAP clients like Splat (Draper 2014) also support server-side spectral cutouts on this service via a DataLink prototype.
4. The spaxels can also be queried in database tables via GAVO's TAP service mentioned above (the tables are called `califadr2.fluxv500` and `califadr2.fluxv1200`).

An overview of VO-accessible resources generated from CALIFA – possibly updated from what is reported here – is available at <http://dc.g-vo.org/browse/califa/q2>. This page also gives some usage scenarios for CALIFA VO resources.

7. Conclusions

Along this article we have presented the main characteristics of the second public data release of the Calar Alto Legacy Integral Field Area (CALIFA) survey. This data release comprises 200 galaxies (400 datacubes) containing more than 1.5 million spectra¹¹, covering a wide range of masses, morphological types, colors, etc. This subset of randomly selected objects conforms a statistically representative sample of the galaxies in the Local Uni-

¹⁰ SSA access URL <http://victor:8080/califa/q2/s/info>.

¹¹ Obtained from ~ 400000 independent spectra from the RSS files.

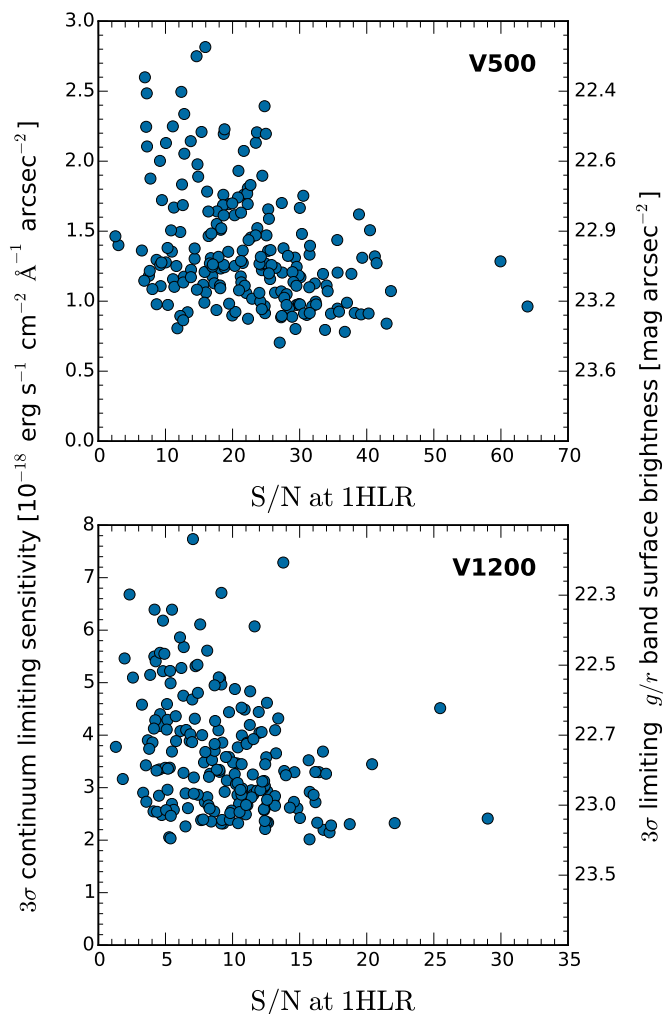


Fig. 20. Limiting 3σ continuum sensitivity as a function of the average continuum S/N at the half light radius (HLR). The corresponding broadband surface brightness limits in r (V500) and g (V1200) are indicated on the right y-axis. The limiting continuum sensitivity and the S/N were computed from the median signal and noise in the wavelength region 4480–4520Å and 5590–5680Å for the V1200 and V500 data, respectively.

verse. The CALIFA DR2 provides science-grade and quality-checked integral-field spectroscopy publicly distributed to the community at <http://califa.caha.es/DR2>.

We have described in detail the main quality parameters analysed in the validation process, provided to the users with complete tables to select the objects for their science cases. The data have been reduced using a new version of the pipeline (V1.5), which improves considerably the quality of the data in terms of: (i) the spatial resolution, (ii) the covariance between the adjacent spectra, and (iii) the spectrophotometric calibration.

Compared with other on-going major surveys, CALIFA offers a better spatial resolution. The PSF of the datacubes has been improved considerably, with a mean value of $\sim 2.5''$ (Sect. 5.4.2), similar to SAMI (Sharp et al. 2014). In the case of MaNGA, the combination of an average seeing at the Sloan Telescope ($\sim 1.5''$) and the fiber size ($2''$), would produce a PSF with a very similar FWHM. The redshift range of SAMI and MaNGA surveys is considerably larger than of CALIFA, reaching up to $z \sim 0.1$. This means that only for galaxies at the lowest redshift range SAMI and MaNGA will offer a similar physical

resolution. On the other hand, the spatial coverage of CALIFA is larger than any of those surveys, both in physical and in projected terms (five times larger than SAMI and two times larger than MaNGA). In summary, CALIFA is the survey that samples the galaxies with the largest number of spatial elements for the largest FoV. The penalty for this wider coverage is the lower number of galaxies observed (6 times lower than SAMI and 15 times lower than MaNGA), and a lower spectral resolution of CALIFA in the full wavelength range.

The shorter redshift range, covering 300 Myrs in cosmological times, provides homogeneity of the derived properties, such as the SFH or the gas abundances, which in other surveys should be corrected prior to making an homogeneous comparison of their full sample.

The dataset analysed so far have produced significant advances in our knowledge of the stellar and gas composition in galaxies, their kinematical structure, and the overall star formation history and chemical enrichment (as reviewed in the introduction). We have uncovered new local relations within galaxies, tightly connected to the global ones described using classical spectroscopic surveys. With this new DR we open to the astronomical community the possibility to further analyse the spatially resolved properties of galaxies, presenting a panoramic view of the galaxy properties.

Acknowledgements. CALIFA is the first legacy survey being performed at Calar Alto. The CALIFA collaboration would like to thank the IAA-CSIC and MPIA-MPG as major partners of the observatory, and CAHA itself, for the unique access to telescope time and support in manpower and infrastructures. The CALIFA collaboration thanks also the CAHA staff for the dedication to this project. RGB, RGD and EP are supported by the Spanish *Ministerio de Ciencia e Innovación* under grant AYA2010-15081. SZ has been supported by the EU Marie Curie Integration Grant “SteMaGE” Nr. PCIG12-GA-2012-326466 (Call Identifier: FP7-PEOPLE-2012 CIG). JFB acknowledges support from grants AYA2010-21322-C03-02 and AIB-2010-DE-00227 from the Spanish Ministry of Economy and Competitiveness (MINECO), as well as from the FP7 Marie Curie Actions of the European Commission, via the Initial Training Network DAGAL under REA grant agreement number 289313. Support for L.G. is provided by the Ministry of Economy, Development, and Tourism’s Millennium Science Initiative through grant IC12009, awarded to The Millennium Institute of Astrophysics, MAS. L.G. also acknowledges support by CONICYT through FONDECYT grant 3140566. AG acknowledges support from the FP7/2007-2013 under grant agreement n. 267251 (AstroFit). JMG acknowledges support from the Fundação para a Ciência e a Tecnologia (FCT) through the Fellowship SFRH/BPD/66958/2009 from FCT (Portugal) and research grant PTDC/FIS-AST/3214/2012. RAM was funded by the Spanish programme of International Campus of Excellence Moncloa (CIE). JMA acknowledges support from the European Research Council Starting Grant (SEDMorph; P.I. V. Wild). IM, JM and AdO acknowledge the support by the projects AYA2010-15196 from the Spanish Ministerio de Ciencia e Innovación and TIC 114 and PO08-TIC-3531 from Junta de Andalucía. AMI acknowledges support from Agence Nationale de la Recherche through the STILISM project (ANR-12-BS05-0016-02). MM acknowledges financial support from AYA2010-21887-C04-02 from the Ministerio de Economía y Competitividad. PP is supported by an FCT Investigador 2013 Contract, funded by FCT/MCTES (Portugal) and POPH/FSE (EC). He acknowledges support by FCT under project FCOMP-01-0124-FEDER-029170 (Reference FCT PTDC/FIS-AST/3214/2012), funded by FCT-MEC (PIDDAC) and FEDER (COMPETE). TRL thanks the support of the Spanish Ministerio de Educación, Cultura y Deporte by means of the FPU fellowship. PSB acknowledges support from the Ramón y Cajal program, grant ATA2010-21322-C03-02 from the Spanish Ministry of Economy and Competitiveness (MINECO). CJW acknowledges support through the Marie Curie Career Integration Grant 303912. V.W. acknowledges support from the European Research Council Starting Grant (SEDMorph P.I. V. Wild) and European Career Re-integration Grant (Phiz-Ev P.I. V. Wild). YA acknowledges financial support from the *Ramón y Cajal* programme (RyC-2011-09461) and project AYA2013-47742-C4-3-P, both managed by the *Ministerio de Economía y Competitividad*, as well as the ‘Study of Emission-Line Galaxies with Integral-Field Spectroscopy’ (SELGIFS) programme, funded by the EU (FP7-PEOPLE-2013-IRSES-612701) within the Marie-Sklodowska-Curie Actions scheme.

References

- Abazajian, K. N., Adelman-McCarthy, J. K., Agüeros, M. A., et al. 2009, *ApJS*, 182, 543
- Aceituno, J. 2004, Calar Alto Newsletter No. 8, <http://www.caha.es/newsletter/news04b/Aceituno/Newsletter.html>
- Alonso-Herrero, A., Rosales-Ortega, F. F., Sánchez, S. F., et al. 2012, *MNRAS*, 425, L46
- Barrera-Ballesteros, J. K., Falcón-Barroso, J., García-Lorenzo, B., et al. 2014, *A&A*, 568, A70
- Bershady, M. A., Verheijen, M. A. W., Swaters, R. A., et al. 2010, *ApJ*, 716, 198
- Blanton, M. R., Schlegel, D. J., Strauss, M. A., et al. 2005, *AJ*, 129, 2562
- Bryant, J. J., Owers, M. S., Robotham, A. S. G., et al. 2014, *ArXiv e-prints*
- Cappellari, M. & Copin, Y. 2003, *MNRAS*, 342, 345
- Cappellari, M., Emsellem, E., Krajnović, D., et al. 2011, *MNRAS*, 413, 813
- Cid Fernandes, R., González Delgado, R. M., García Benito, R., et al. 2014, *A&A*, 561, A130
- Cid Fernandes, R., Mateus, A., Sodré, L., Stasińska, G., & Gomes, J. M. 2005, *MNRAS*, 358, 363
- Cid Fernandes, R., Pérez, E., García Benito, R., et al. 2013, *A&A*, 557, A86
- Croom, S. M., Lawrence, J. S., Bland-Hawthorn, J., et al. 2012, *MNRAS*, 421, 872
- Davies, R. L., Kewley, L. J., Ho, I., & Dopita, M. A. 2014, *ArXiv e-prints*
- De Geyter, G., Baes, M., Camps, P., et al. 2014, *MNRAS*, 441, 869
- Dowler, P., Rixton, G., & Tody, D. 2011, *ArXiv e-prints*
- Draper, P. W. 2014, SPLAT: Spectral Analysis Tool, astrophysics Source Code Library
- Erwin, P. 2014, *ArXiv e-prints*
- Fruchter, A. S. & Hook, R. N. 2002, *PASP*, 114, 144
- Galbany, L., Stanishev, V., Mourão, A. M., et al. 2014, *ArXiv e-prints*
- García-Lorenzo, B., Marquez, I., Barrera-Ballesteros, J. K., et al. 2014, *ArXiv e-prints*
- González Delgado, R. M., Cerviño, M., Martins, L. P., Leitherer, C., & Hauschildt, P. H. 2005, *MNRAS*, 357, 945
- González Delgado, R. M., Cid Fernandes, R., García-Benito, R., et al. 2014a, *ApJ*, 791, L16
- González Delgado, R. M., Pérez, E., Cid Fernandes, R., et al. 2014b, *A&A*, 562, A47
- Greisen, E. W. & Calabretta, M. R. 2002, *A&A*, 395, 1061
- Holwerda, B. W. & Keel, W. C. 2013, *A&A*, 556, A42
- Husemann, B., Jahnke, K., Sánchez, S. F., et al. 2013, *A&A*, 549, A87 (H13)
- Iglesias-Páramo, J., Vílchez, J. M., Galbany, L., et al. 2013, *A&A*, 553, L7
- Kehrig, C., Monreal-Ibero, A., Papaderos, P., et al. 2012, *A&A*, 540, A11
- Kelz, A., Verheijen, M. A. W., Roth, M. M., et al. 2006, *PASP*, 118, 129
- Law, D. R. & MaNGA Team. 2014, in *American Astronomical Society Meeting Abstracts*, Vol. 223, *American Astronomical Society Meeting Abstracts #223*, 254.31
- Louys, M., Bonnarel, F., Schade, D., et al. 2011, *Observation Data Model Core Components and its Implementation in the Table Access Protocol, Version 1.0, IVOA Recommendation*
- Marino, R. A., Rosales-Ortega, F. F., Sánchez, S. F., et al. 2013, *A&A*, 559, A114
- Mármol-Queraltó, E., Sánchez, S. F., Marino, R. A., et al. 2011, *A&A*, 534, A8
- Martínez-García, E. E., Puerari, I., Rosales-Ortega, F. F., et al. 2014, *ArXiv e-prints*
- Mast, D., Rosales-Ortega, F. F., Sánchez, S. F., et al. 2014, *A&A*, 561, A129
- Papaderos, P., Gomes, J. M., Vílchez, J. M., et al. 2013, *A&A*, 555, L1
- Pérez, E., Cid Fernandes, R., González Delgado, R. M., et al. 2013, *ApJ*, 764, L1
- Rosales-Ortega, F. F., Díaz, A. I., Kennicutt, R. C., & Sánchez, S. F. 2011, *MNRAS*, 415, 2439
- Rosales-Ortega, F. F., Kennicutt, R. C., Sánchez, S. F., et al. 2010, *MNRAS*, 405, 735
- Rosales-Ortega, F. F., Sánchez, S. F., Iglesias-Páramo, J., et al. 2012, *ApJ*, 756, L31
- Roth, M. M., Kelz, A., Fechner, T., et al. 2005, *PASP*, 117, 620
- Sánchez, S. F., Cardiel, N., Verheijen, M. A. W., Pedraz, S., & Covone, G. 2007, *MNRAS*, 376, 125
- Sánchez, S. F., Kennicutt, R. C., Gil de Paz, A., et al. 2012a, *A&A*, 538, A8 (S12)
- Sánchez, S. F., Rosales-Ortega, F. F., Iglesias-Páramo, J., et al. 2014, *A&A*, 563, A49
- Sánchez, S. F., Rosales-Ortega, F. F., Jungwiert, B., et al. 2013, *A&A*, 554, A58
- Sánchez, S. F., Rosales-Ortega, F. F., Kennicutt, R. C., et al. 2011, *MNRAS*, 410, 313
- Sánchez, S. F., Rosales-Ortega, F. F., Marino, R. A., et al. 2012b, *A&A*, 546, A2
- Sanchez-Blazquez, P., Rosales-Ortega, F., Mendez-Abreu, J., et al. 2014, *ArXiv e-prints*
- Sharp, R., Allen, J. T., Fogarty, L. M. R., et al. 2014, *ArXiv e-prints*
- Singh, R., van de Ven, G., Jahnke, K., et al. 2013, *A&A*, 558, A43
- Vazdekis, A., Sánchez-Blázquez, P., Falcón-Barroso, J., et al. 2010, *MNRAS*, 404, 1639
- Verheijen, M. A. W., Bershady, M. A., Andersen, D. R., et al. 2004, *Astronomische Nachrichten*, 325, 151
- Viironen, K., Sánchez, S. F., Marmol-Queraltó, E., et al. 2012, *A&A*, 538, A144
- Walcher, C. J., Wisotzki, L., Bekeraite, S., et al. 2014, *A&A*, 569, A1 (W14)
- Wild, V., Rosales-Ortega, F., Falcón-Barroso, J., et al. 2014, *A&A*, 567, A132

¹ Instituto de Astrofísica de Andalucía (IAA/CSIC), Glorieta de la Astronomía s/n Aptdo. 3004, E-18080 Granada, Spain, e-mail: rgb@iaa.es

² INAF-Osservatorio Astrofisico di Arcetri - Largo Enrico Fermi, 5 - I-50125 Firenze, Italy

³ Instituto de Astronomía, Universidad Nacional Autónoma de México, A.P. 70-264, 04510, México, D.F.

⁴ European Southern Observatory, Karl-Schwarzschild-Str. 2, D-85748 Garching b. München, Germany

⁵ Departamento de Física, Universidade Federal de Santa Catarina, P.O. Box 476, 88040-900, Florianópolis, SC, Brazil

⁶ Departamento de Astrofísica y CC. de la Atmósfera, Universidad Complutense de Madrid, E-28040, Madrid, Spain

⁷ Australian Astronomical Observatory, 105 Delhi Road, North Ryde, NSW 2113, Australia

⁸ Instituto de Astrofísica de Canarias, Vía Láctea s/n, La Laguna, Tenerife, Spain

⁹ Departamento de Astrofísica, Universidad de La Laguna, E-38205 La Laguna, Tenerife, Spain

¹⁰ Millennium Institute of Astrophysics, Universidad de Chile, Santiago, Chile

¹¹ Departamento de Astronomía, Universidad de Chile, Casilla 36-D, Santiago, Chile

¹² School of Physics and Astronomy, University of St Andrews, SUPA, North Haugh, KY16 9SS, St Andrews, UK

¹³ Kapteyn Astronomical Institute, University of Groningen, Postbus 800, 9700 AV Groningen, The Netherlands

¹⁴ Max-Planck-Institut für Astronomie, Königstuhl 17, D-69117 Heidelberg, Germany

¹⁵ CEI Campus Moncloa, UCM-UPM, Departamento de Astrofísica y CC. de la Atmósfera, Facultad de CC. Físicas, Universidad Complutense de Madrid, Avda. Complutense s/n, 28040 Madrid, Spain

¹⁶ Instituto de Cosmología, Relatividade e Astrofísica – ICRA, Centro Brasileiro de Pesquisas Físicas, Rua Dr.Xavier Sigaud 150, CEP 22290-180, Rio de Janeiro, RJ, Brazil

¹⁷ Departamento de Física Teórica, Facultad de Ciencias, Universidad Autónoma de Madrid, E-28049 Madrid, Spain

¹⁸ Leibniz-Institut für Astrophysik Potsdam (AIP), An der Sternwarte 16, D-14482 Potsdam, Germany

¹⁹ Sydney Institute for Astronomy, School of Physics, University of Sydney, NSW 2006, Australia

²⁰ Universität Heidelberg, Zentrum für Astronomie, Astronomisches Rechen-Institut, Mönchhofstraße 12-14, D-69120 Heidelberg, Germany

²¹ Astronomisches Institut, Ruhr-Universität Bochum, Universitätsstr. 150, D-44801 Bochum, Germany

²² RUB Research Department Plasmas with Complex Interactions

²³ Departamento de Física Teórica y del Cosmos, University of Granada, Facultad de Ciencias (Edificio Mecenas), E-18071 Granada, Spain

²⁴ Dark Cosmology Center, University of Copenhagen, Niels Bohr Institute, Juliane Maries Vej 30, 2100 Copenhagen, Denmark

²⁵ Instituto de Astrofísica e Ciências do Espaço, Universidade do Porto, CAUP, Rua das Estrelas, PT4150-762 Porto, Portugal

²⁶ Department of Physics, Royal Military College of Canada, PO box 17000, Station Forces, Kingston, Ontario, Canada, K7K 7B4

²⁷ Centro Astronómico Hispano Alemán de Calar Alto (CSIC-MPG), C/ Jesús Durbán Remón 2-2, E-4004 Almería, Spain

- ²⁸ Department of Physics 4-181 CCIS, University of Alberta, Edmonton AB T6G 2E1, Canada
- ²⁹ Institute of Astronomy, University of Cambridge, Madingley Road, Cambridge CB3 0HA, UK
- ³⁰ Australian Astronomical Observatory, PO Box 915, North Ryde, NSW 1670, Australia
- ³¹ Department of Physics and Astronomy, Macquarie University, NSW 2109, Australia
- ³² CIEMAT, Avda. Complutense 40, 28040 Madrid, Spain
- ³³ GEPI, Observatoire de Paris, CNRS, Université Paris Diderot, Place Jules Janssen, 92190 Meudon, France
- ³⁴ Instituto Universitario Carlos I de Física Teórica y Computacional, Universidad de Granada, 18071 Granada, Spain
- ³⁵ Landessternwarte, Zentrum für Astronomie der Universität Heidelberg, Königstuhl 12, D-69117 Heidelberg, Germany
- ³⁶ Instituto Nacional de Astrofísica, Óptica y Electrónica, Luis E. Erro 1, 72840 Tonantzintla, Puebla, Mexico
- ³⁷ CENTRA - Centro Multidisciplinar de Astrofísica, Instituto Superior Técnico, Av. Rovisco Pais 1, 1049-001 Lisbon, Portugal
- ³⁸ Department of Physics, Chemistry and Biology, IFM, Linköping University, SE-581 83 Linköping, Sweden
- ³⁹ Departamento de Astronomía, Universidad de Guanajuato, Apartado Postal 144, 36000, Guanajuato, Guanajuato, Mexico
- ⁴⁰ University of Vienna, Department of Astrophysics, Türkenschanzstr. 17, 1180 Vienna, Austria

Table 1. CALIFA DR2 galaxies and their characteristics.

Name	ID ^a	α (J2000) ^b	δ (J2000) ^b	z^c	m_g^d	m_z^d	$m_u - m_z^d$	type ^e	bar ^f	b/a^g
IC5376	001	00:01:19.779	+34:31:32.409	0.0168	14.24	12.60	3.48	Sb	A	0.27
UGC00005	002	00:03:05.643	-01:54:49.804	0.0243	13.88	12.53	2.95	Sbc	A	0.54
NGC7819	003	00:04:24.505	+31:28:19.228	0.0167	14.06	13.01	2.12	Sc	A	0.53
IC1528	005	00:05:05.377	-07:05:36.204	0.0128	13.46	12.52	2.43	Sbc	AB	0.36
UGC00036	007	00:05:13.882	+06:46:19.306	0.0210	14.12	12.46	3.55	Sab	AB	0.60
NGC0001	008	00:07:15.860	+27:42:29.096	0.0151	13.46	12.01	2.97	Sbc	A	0.80
NGC0036	010	00:11:22.298	+06:23:21.667	0.0203	13.46	12.01	3.23	Sb	B	0.65
MCG-02-02-030	013	00:30:07.309	-11:06:49.066	0.0118	13.41	12.08	2.91	Sb	AB	0.34
UGC00312	014	00:31:23.922	+08:28:00.232	0.0145	13.76	13.07	1.52	Sd	B	0.35
UGC00335NED02	017	00:33:57.323	+07:16:05.781	0.0183	14.27	12.82	3.42	E4(x)	A	0.63
NGC0169	022	00:36:51.608	+23:59:27.501	0.0154	14.04	11.74	4.50	Sab(x)	A	0.42
NGC0171	023	00:37:21.552	-19:56:03.210	0.0131	13.21	11.73	3.29	Sb	B	0.63
NGC0180	025	00:37:57.703	+08:38:06.588	0.0177	13.51	11.98	3.00	Sb	B	0.64
NGC0192	026	00:39:13.414	+00:51:50.968	0.0140	13.37	11.72	3.23	Sab	AB	0.31
NGC0216	027	00:41:27.170	-21:02:40.826	0.0052	13.55	12.78	1.78	Sd	A	0.27
NGC0237	030	00:43:27.841	-00:07:29.747	0.0139	13.52	12.38	2.44	Sc	B	0.57
IC1652	037	01:14:56.277	+31:56:54.606	0.0173	14.08	12.72	3.13	S0a	A	0.31
NGC0444	039	01:15:49.562	+31:04:50.245	0.0161	14.47	13.48	2.20	Scd	A	0.24
UGC00809	040	01:15:51.837	+33:48:38.532	0.0140	14.81	13.74	2.52	Scd	A	0.19
UGC00841	041	01:19:10.028	+33:01:50.248	0.0186	14.91	13.73	2.55	Sbc	A	0.25
NGC0477	042	01:21:20.483	+40:29:17.332	0.0196	14.43	13.09	2.66	Sbc	AB	0.66
IC1683	043	01:22:38.929	+34:26:13.654	0.0162	14.11	12.63	2.98	Sb	AB	0.59
NGC0499	044	01:23:11.496	+33:27:36.683	0.0146	12.76	11.19	3.49	E5	A	0.61
NGC0496	045	01:23:11.595	+33:31:45.386	0.0201	13.92	12.93	2.25	Scd	A	0.58
NGC0528	050	01:25:33.571	+33:40:17.198	0.0161	13.51	11.89	3.58	S0	A	0.49
UGC01057	053	01:28:53.253	+13:47:37.674	0.0212	14.54	13.26	2.66	Sc	AB	0.30
NGC0774	072	01:59:34.729	+14:00:29.536	0.0154	13.52	11.88	3.50	S0	A	0.72
NGC0776	073	01:59:54.525	+23:38:39.392	0.0164	13.52	12.06	3.19	Sb	B	0.69
NGC0810	076	02:05:28.562	+13:15:05.867	0.0257	13.70	11.93	3.74	E5(x)	A	0.69
NGC0825	077	02:08:32.329	+06:19:25.200	0.0113	13.63	12.04	3.29	Sa	A	0.33
UGC01938	088	02:28:22.137	+23:12:52.655	0.0213	14.70	13.31	2.90	Sbc	AB	0.25
NGC1056	100	02:42:48.312	+28:34:26.961	0.0052	13.00	11.41	3.02	Sa	A	0.57
UGC02222	103	02:45:09.676	+32:59:22.935	0.0166	13.76	12.29	3.32	S0a(x)	AB	0.51
UGC02229	104	02:45:27.567	+00:54:51.657	0.0244	14.16	12.48	3.49	S0a(x)	A	0.57
UGC02403	115	02:55:57.257	+00:41:33.378	0.0137	14.15	12.41	3.44	Sb	B	0.28
NGC1349	127	03:31:27.512	+04:22:51.241	0.0220	13.34	11.80	3.45	E6	A	0.89
NGC1542	131	04:17:14.172	+04:46:54.239	0.0125	13.60	12.14	3.00	Sab	AB	0.38
UGC03107	133	04:37:21.852	+09:32:40.747	0.0283	14.89	13.35	3.19	Sb	A	0.24
NGC1645	134	04:44:06.400	-05:27:56.414	0.0163	13.46	11.97	3.38	S0a	B	0.64
IC2095	141	04:48:45.881	-05:07:28.668	0.0095	15.59	15.23	1.28	Sc	AB	0.15
UGC03253	146	05:19:41.885	+84:03:09.432	0.0138	13.69	12.27	3.07	Sb	B	0.62
NGC2253	147	06:43:41.836	+65:12:22.950	0.0120	13.26	11.79	2.97	Sbc	B	0.87
UGC03539	148	06:48:54.003	+66:15:41.885	0.0110	14.95	14.13	2.31	Sc	AB	0.19
NGC2347	149	07:16:04.087	+64:42:40.776	0.0149	13.18	11.65	3.08	Sbc	AB	0.64
UGC03899	150	07:32:37.749	+35:36:52.125	0.0130	14.99	14.46	1.47	Sd	A	0.43
NGC2410	151	07:35:02.261	+32:49:19.566	0.0156	13.37	11.78	3.29	Sb	AB	0.32
UGC03969	153	07:41:14.343	+27:36:50.635	0.0275	15.03	13.42	3.21	Sb	A	0.18
UGC03995	155	07:44:09.128	+29:14:50.751	0.0159	13.48	11.92	3.58	Sb	B	0.46
NGC2449	156	07:47:20.299	+26:55:48.708	0.0163	13.70	12.22	3.37	Sab	AB	0.50
UGC04132	165	07:59:13.046	+32:54:52.822	0.0174	13.80	12.23	3.17	Sbc	AB	0.26
UGC04722	231	09:00:24.130	+25:36:53.079	0.0058	15.16	15.07	1.25	Sdm	A	0.19
NGC2730	232	09:02:15.824	+16:50:17.841	0.0128	13.93	13.13	1.95	Scd	B	0.64
NGC2880	272	09:29:34.567	+62:29:26.052	0.0051	12.40	10.99	3.21	E7	AB	0.71
IC2487	273	09:30:09.166	+20:05:27.042	0.0145	13.94	12.58	2.90	Sc	AB	0.22
IC0540	274	09:30:10.338	+07:54:09.903	0.0069	14.24	12.76	3.17	Sab	AB	0.30
NGC2906	275	09:32:06.218	+08:26:30.367	0.0071	12.89	11.46	3.37	Sbc	A	0.51
NGC2916	277	09:34:57.601	+21:42:18.940	0.0124	13.37	11.86	3.16	Sbc	A	0.59
UGC05108	278	09:35:26.279	+29:48:45.439	0.0271	14.35	12.73	3.35	Sb	B	0.77
UGC05358	306	09:58:47.135	+11:23:19.318	0.0097	15.12	14.41	1.79	Sd	B	0.33
UGC05359	307	09:58:51.647	+19:12:53.918	0.0283	14.74	13.43	2.93	Sb	B	0.37

Table 1. continued.

Name	ID ^a	α (J2000) ^b	δ (J2000) ^b	z^c	m_g^d	m_z^d	$m_u - m_z^d$	type ^e	bar ^f	b/a^g
UGC05396	309	10:01:40.485	+10:45:23.140	0.0181	14.43	13.24	2.66	Sbc	AB	0.27
NGC3106	311	10:04:05.251	+31:11:07.653	0.0207	13.41	12.01	3.31	Sab	A	0.93
UGC05498NED01	314	10:12:03.658	+23:05:07.590	0.0210	14.65	12.95	3.48	Sa(x)	A	0.24
NGC3160	319	10:13:55.115	+38:50:34.534	0.0229	14.64	12.92	3.63	Sab	AB	0.29
UGC05598	326	10:22:14.004	+20:35:21.879	0.0188	14.80	13.52	2.77	Sb	A	0.30
NGC3303	340	10:37:00.088	+18:08:09.194	0.0200	14.24	12.55	3.56	S0a(x)	AB	0.60
UGC05771	341	10:37:19.340	+43:35:15.321	0.0248	14.10	12.43	3.58	E6	A	0.71
NGC3381	353	10:48:24.818	+34:42:41.078	0.0054	13.41	12.68	1.82	Sd	B	0.71
UGC06036	364	10:55:55.261	+36:51:41.468	0.0218	14.14	12.47	3.65	Sa	A	0.29
IC0674	381	11:11:06.361	+43:37:58.812	0.0251	14.07	12.57	3.40	Sab	B	0.65
NGC3614	388	11:18:21.332	+45:44:53.408	0.0077	13.60	12.37	2.90	Sbc	AB	0.72
NGC3811	436	11:41:16.630	+47:41:26.920	0.0102	13.48	12.06	3.00	Sbc	B	0.62
NGC3991	475	11:57:30.959	+32:20:13.289	0.0108	14.08	13.52	1.42	Sm	A	0.22
NGC3994	476	11:57:36.866	+32:16:39.426	0.0103	13.46	11.98	2.87	Sbc	AB	0.47
NGC4003	479	11:57:59.033	+23:07:29.636	0.0219	13.96	12.39	3.29	S0a	B	0.42
UGC07012	486	12:02:03.146	+29:50:52.737	0.0102	14.41	13.81	1.73	Scd	AB	0.54
NGC4149	502	12:10:32.849	+58:18:14.884	0.0103	13.86	12.30	3.10	Sa	AB	0.19
NGC4185	515	12:13:22.192	+28:30:39.468	0.0130	13.27	12.01	3.03	Sbc	AB	0.64
NGC4210	518	12:15:15.842	+65:59:07.156	0.0091	13.44	12.03	2.99	Sb	B	0.73
IC0776	528	12:19:03.120	+08:51:22.153	0.0081	14.74	14.42	1.25	Sdm	A	0.56
NGC4470	548	12:29:37.778	+07:49:27.129	0.0079	12.96	12.12	1.84	Sc	A	0.66
NGC4644	569	12:42:42.664	+55:08:43.897	0.0165	14.41	13.02	3.00	Sb	A	0.45
NGC4676A	577	12:46:10.107	+30:43:54.899	0.0222	14.78	13.08	2.99	Sdm(x)	AB	0.28
NGC4874	592	12:59:35.709	+27:57:33.339	0.0239	12.89	11.37	3.42	E0	A	0.88
UGC08107	593	12:59:39.778	+53:20:28.203	0.0277	14.30	12.71	3.45	Sa(x)	A	0.39
UGC08231	606	13:08:37.555	+54:04:27.737	0.0083	14.44	13.97	1.45	Sd	AB	0.37
UGC08234	607	13:08:46.505	+62:16:18.099	0.0270	13.45	12.23	2.92	S0	A	0.63
NGC5000	608	13:09:47.487	+28:54:24.993	0.0187	13.94	12.50	2.97	Sbc	B	0.60
UGC08250	609	13:10:20.138	+32:28:59.479	0.0176	15.17	14.03	2.39	Sc	A	0.19
UGC08267	610	13:11:11.334	+43:43:34.787	0.0242	14.87	13.14	3.39	Sb	AB	0.20
NGC5205	630	13:30:03.571	+62:30:41.624	0.0059	13.45	12.12	2.92	Sbc	B	0.67
NGC5216	633	13:32:06.896	+62:42:02.392	0.0098	13.58	12.12	3.27	E0	A	0.91
UGC08733	657	13:48:38.994	+43:24:44.830	0.0078	14.70	13.63	1.83	Sdm	B	0.49
IC0944	663	13:51:30.868	+14:05:31.959	0.0234	13.67	11.95	3.59	Sab	A	0.30
UGC08778	664	13:52:06.669	+38:04:01.273	0.0108	14.20	12.90	2.89	Sb	A	0.21
UGC08781	665	13:52:22.745	+21:32:21.669	0.0253	13.92	12.49	3.31	Sb	B	0.52
NGC5378	676	13:56:51.013	+37:47:50.055	0.0100	13.53	12.12	3.23	Sb	B	0.63
NGC5394	680	13:58:33.201	+37:27:13.118	0.0114	14.39	13.59	2.29	Sbc(x)	B	0.74
NGC5406	684	14:00:20.120	+38:54:55.528	0.0180	13.37	11.84	3.46	Sb	B	0.88
NGC5485	708	14:07:11.349	+55:00:05.933	0.0064	12.41	10.88	3.42	E5	A	0.81
UGC09067	714	14:10:45.458	+15:12:33.858	0.0262	14.29	13.09	2.61	Sbc	AB	0.45
NGC5520	715	14:12:22.811	+50:20:54.309	0.0063	13.31	12.05	2.71	Sbc	A	0.57
NGC5614	740	14:24:07.588	+34:51:31.869	0.0130	12.68	11.03	3.56	Sa(x)	A	0.95
NGC5630	749	14:27:36.610	+41:15:27.919	0.0089	13.60	13.04	1.62	Sdm	B	0.32
NGC5682	758	14:34:44.978	+48:40:12.831	0.0076	14.39	13.64	1.74	Scd	B	0.31
NGC5720	764	14:38:33.281	+50:48:54.874	0.0260	14.13	12.72	3.18	Sbc	B	0.65
UGC09476	769	14:41:32.029	+44:30:45.978	0.0109	13.63	12.61	2.31	Sbc	A	0.63
NGC5784	778	14:54:16.450	+42:33:28.452	0.0181	13.20	11.69	3.45	S0	A	0.81
UGC09665	783	15:01:32.465	+48:19:10.928	0.0085	14.30	12.83	3.12	Sb	A	0.23
NGC5888	789	15:13:07.372	+41:15:52.666	0.0291	13.84	12.25	3.47	Sb	B	0.54
NGC5908	791	15:16:43.191	+55:24:34.461	0.0112	13.12	11.15	3.97	Sa	A	0.24
NGC5930	795	15:26:07.950	+41:40:33.829	0.0088	13.53	11.76	3.27	Sab(x)	AB	0.84
UGC09873	797	15:29:50.651	+42:37:44.104	0.0188	15.19	13.95	2.63	Sb	A	0.21
UGC09892	798	15:32:51.947	+41:11:29.282	0.0189	14.80	13.51	2.78	Sbc	A	0.29
NGC5966	806	15:35:52.108	+39:46:08.047	0.0151	13.24	11.76	3.36	E4	A	0.60
IC4566	807	15:36:42.162	+43:32:21.545	0.0186	13.84	12.35	3.39	Sb	B	0.69
NGC5987	809	15:39:57.356	+58:04:46.249	0.0100	12.76	11.07	3.62	Sa	A	0.39
NGC6004	813	15:50:22.720	+18:56:21.386	0.0128	13.55	12.22	3.02	Sbc	B	0.94
NGC6020	815	15:57:08.137	+22:24:16.492	0.0144	13.40	11.94	3.40	E4	A	0.73
NGC6021	816	15:57:30.685	+15:57:21.766	0.0158	13.63	12.10	3.45	E5	A	0.78
NGC6032	820	16:03:01.124	+20:57:21.330	0.0145	13.97	12.56	2.94	Sbc	B	0.30

Table 1. continued.

Name	ID ^a	α (J2000) ^b	δ (J2000) ^b	z^c	m_g^d	m_z^d	$m_u - m_z^d$	type ^e	bar ^f	b/a^g
UGC10205	822	16:06:40.181	+30:05:56.651	0.0219	13.89	12.29	3.32	S0a	A	0.58
NGC6063	823	16:07:12.993	+07:58:44.368	0.0095	13.63	12.53	2.56	Sbc	A	0.60
IC1199	824	16:10:34.347	+10:02:25.322	0.0158	13.97	12.59	2.86	Sb	AB	0.41
NGC6081	826	16:12:56.858	+09:52:01.580	0.0171	13.62	11.93	3.65	S0a	A	0.46
UGC10331	828	16:17:21.123	+59:19:12.466	0.0152	14.50	13.60	2.11	Sc(x)	AB	0.26
NGC6125	829	16:19:11.536	+57:59:02.899	0.0154	12.91	11.39	3.43	E1	A	0.91
NGC6132	831	16:23:38.840	+11:47:10.459	0.0166	14.18	13.09	2.38	Sbc	A	0.36
NGC6146	832	16:25:10.331	+40:53:34.325	0.0292	13.28	11.80	3.40	E5	A	0.77
NGC6154	833	16:25:30.483	+49:50:24.934	0.0199	13.81	12.39	3.33	Sab	B	0.65
UGC10380	834	16:25:49.911	+16:34:33.827	0.0292	14.89	13.18	3.57	Sb	AB	0.28
NGC6150	835	16:25:49.966	+40:29:19.419	0.0292	13.92	12.35	3.49	E7	A	0.48
UGC10384	837	16:26:46.685	+11:34:48.968	0.0165	14.70	13.22	2.82	Sb	A	0.22
UGC10388	838	16:27:02.974	+16:22:56.031	0.0154	14.03	12.67	3.15	Sa	AB	0.40
NGC6173	840	16:29:44.875	+40:48:41.965	0.0294	13.16	11.61	3.49	E6	A	0.65
NGC6168	841	16:31:20.834	+20:11:08.298	0.0086	14.70	13.58	2.30	Sc	AB	0.18
UGC10650	843	17:00:14.583	+23:06:22.839	0.0099	15.35	16.29	0.04	Scd	A	0.20
UGC10693	845	17:04:53.020	+41:51:55.764	0.0280	13.45	12.00	3.41	E7	AB	0.68
UGC10695	846	17:05:05.574	+43:02:35.360	0.0280	13.98	12.42	3.50	E5	A	0.67
UGC10710	847	17:06:52.522	+43:07:19.961	0.0280	14.35	12.75	3.31	Sb	A	0.25
NGC6310	848	17:07:57.480	+60:59:24.569	0.0114	13.72	12.29	3.24	Sb	A	0.22
NGC6314	850	17:12:38.716	+23:16:12.297	0.0221	13.52	12.12	3.09	Sab	A	0.51
NGC6338	851	17:15:22.976	+57:24:40.284	0.0274	13.33	11.70	3.66	E5	A	0.66
UGC10796	852	17:16:47.725	+61:55:12.433	0.0102	14.28	13.74	1.44	Scd	AB	0.49
UGC10811	854	17:18:43.726	+58:08:06.433	0.0291	14.55	13.02	3.30	Sb	B	0.42
IC1256	856	17:23:47.285	+26:29:11.482	0.0159	13.91	12.70	2.60	Sb	AB	0.59
NGC6394	857	17:30:21.423	+59:38:23.613	0.0284	14.53	13.06	3.05	Sbc	B	0.29
UGC10905	858	17:34:06.438	+25:20:38.290	0.0265	13.68	12.15	3.37	S0a	A	0.53
NGC6411	859	17:35:32.849	+60:48:48.255	0.0123	12.73	11.37	3.34	E4	A	0.68
NGC6427	860	17:43:38.599	+25:29:38.178	0.0108	13.28	11.82	3.30	S0	AB	0.61
UGC10972	861	17:46:21.921	+26:32:37.681	0.0155	14.10	12.78	2.91	Sbc	A	0.22
NGC6478	862	17:48:37.742	+51:09:13.683	0.0227	14.16	12.83	2.59	Sc	A	0.42
NGC6497	863	17:51:17.966	+59:28:15.149	0.0105	13.73	12.26	3.41	Sab	B	0.65
NGC6515	864	17:57:25.195	+50:43:41.242	0.0228	13.52	12.10	3.27	E3	A	0.78
UGC11228	865	18:24:46.260	+41:29:33.853	0.0194	13.78	12.26	3.43	S0	B	0.57
UGC11262	866	18:30:35.698	+42:41:33.704	0.0186	14.89	13.75	2.65	Sc	A	0.39
NGC6762	867	19:05:37.090	+63:56:02.791	0.0098	13.81	12.37	3.29	Sab	A	0.49
MCG-02-51-004	868	20:15:39.858	-13:37:19.227	0.0188	13.88	12.47	2.93	Sb	A	0.37
NGC6941	869	20:36:23.474	-04:37:07.459	0.0208	13.47	12.06	3.14	Sb	B	0.73
NGC6978	871	20:52:35.435	-05:42:40.041	0.0199	13.48	11.95	3.27	Sb	AB	0.39
UGC11649	872	20:55:27.620	-01:13:30.879	0.0127	13.47	12.06	3.19	Sab	B	0.88
NGC7025	874	21:07:47.336	+16:20:09.224	0.0166	12.85	11.25	3.57	S0a	A	0.72
UGC11717	877	21:18:35.413	+19:43:07.397	0.0212	14.20	12.45	3.60	Sab	A	0.47
MCG-01-54-016	878	21:25:59.971	-03:48:32.267	0.0098	14.90	14.26	1.56	Scd	A	0.13
UGC11792	880	21:42:12.700	+05:36:55.333	0.0160	14.82	13.30	3.08	Sbc	A	0.20
NGC7194	881	22:03:30.938	+12:38:12.414	0.0272	13.55	12.01	3.47	E3	A	0.79
UGC11958	883	22:14:46.882	+13:50:27.132	0.0262	14.02	12.47	3.44	S0(x)	A	0.74
UGC11982	884	22:18:52.939	-01:03:31.254	0.0162	15.24	14.09	2.68	Scd	A	0.23
UGC12054	885	22:29:32.454	+07:43:33.685	0.0070	14.62	13.82	1.89	Sc	A	0.24
NGC7311	886	22:34:06.797	+05:34:13.166	0.0150	12.60	11.18	3.25	Sa	A	0.49
NGC7321	887	22:36:28.022	+21:37:18.354	0.0238	13.58	12.29	2.98	Sbc	B	0.69
UGC12127	888	22:38:29.421	+35:19:46.894	0.0275	13.46	11.94	3.53	E1	A	0.85
UGC12185	890	22:47:25.063	+31:22:24.672	0.0222	14.16	12.75	3.21	Sb	B	0.47
UGC12224	891	22:52:38.364	+06:05:37.045	0.0118	13.89	12.86	2.60	Sc	A	0.83
NGC7436B	893	22:57:57.546	+26:09:00.012	0.0246	13.40	11.80	3.59	E2(x)	A	0.90
UGC12274	894	22:58:19.600	+26:03:42.974	0.0255	14.21	12.59	3.63	Sa	A	0.36
UGC12308	895	23:01:18.684	+14:20:22.466	0.0076	14.69	14.01	1.82	Scd	A	0.25
NGC7466	896	23:02:03.464	+27:03:09.342	0.0251	14.22	12.76	3.00	Sbc	A	0.53
NGC7489	898	23:07:32.695	+22:59:53.127	0.0208	13.70	12.61	2.42	Sbc	A	0.55
NGC7549	901	23:15:17.271	+19:02:30.437	0.0157	13.98	12.62	2.76	Sbc	B	0.75
NGC7563	902	23:15:55.928	+13:11:46.040	0.0143	13.33	11.80	3.45	Sa	B	0.68
NGC7562	903	23:15:57.495	+06:41:15.151	0.0120	12.10	10.56	3.43	E4	A	0.68

Table 1. continued.

Name	ID ^a	α (J2000) ^b	δ (J2000) ^b	z^c	m_g^d	m_z^d	$m_u - m_z^d$	type ^e	bar ^f	b/a^g
NGC7591	904	23:18:16.260	+06:35:08.860	0.0165	13.39	11.80	3.24	Sbc	B	0.59
UGC12519	909	23:20:02.769	+15:57:10.028	0.0146	14.24	12.90	2.87	Sc	AB	0.21
UGC12518	910	23:20:12.737	+07:55:55.915	0.0093	14.74	12.91	3.67	Sb	A	0.23
NGC7625	913	23:20:30.139	+17:13:32.034	0.0054	13.03	11.47	3.03	Sa	A	0.78
NGC7631	914	23:21:26.675	+08:13:03.463	0.0125	13.40	12.05	3.00	Sb	A	0.44
NGC7653	915	23:24:49.358	+15:16:32.165	0.0142	13.17	11.88	3.00	Sb	A	0.88
NGC7671	916	23:27:19.336	+12:28:02.673	0.0135	13.14	11.56	3.56	S0	A	0.65
NGC7683	917	23:29:03.823	+11:26:42.607	0.0124	13.00	11.38	3.61	S0	A	0.62
UGC12688	922	23:35:26.096	+07:19:19.554	0.0174	14.53	13.47	2.29	Scd(x)	AB	0.29
NGC7716	924	23:36:31.450	+00:17:50.179	0.0085	13.03	11.60	3.25	Sb	A	0.71
NGC7738	927	23:44:02.058	+00:30:59.838	0.0228	13.94	12.17	3.56	Sb	B	0.31
UGC12816	930	23:51:50.691	+03:04:57.909	0.0178	14.09	13.16	2.08	Sc	A	0.62
NGC7783NED01	932	23:54:10.078	+00:22:58.299	0.0262	13.62	12.06	3.43	Sa(x)	A	0.46
UGC12864	935	23:57:23.921	+30:59:31.456	0.0156	14.24	13.25	2.19	Sc	B	0.32
MCG-01-01-012	936	23:59:10.803	-04:11:29.763	0.0193	14.64	12.83	4.07	Sab	AB	0.26
NGC7800	937	23:59:36.753	+14:48:25.043	0.0058	13.35	13.16	1.11	Ir	AB	0.40
NGC5947	938	15:30:36.595	+42:43:01.732	0.0198	14.07	12.81	2.80	Sbc	B	0.83
NGC4676B ^h	939	12:46:11.235	+30:43:21.871	0.0218	17.00	15.31	3.44	Sb(x)	B	0.82

Notes. ^(a) CALIFA unique ID number for the galaxy. ^(b) Equatorial coordinates of the galaxies as provided by NED. ^(c) Redshift of the galaxies based on SDSS DR7 spectra or complemented with SIMBAD information if SDSS spectra are not available. ^(d) Petrosian magnitudes as given by SDSS DR7 database corrected for Galactic extinction. ^(e) Morphological type from our own visual classification (see W14 for details). “(x)” indicates ongoing mergers. ^(f) Bar strength of the galaxy as an additional outcome of our visual classification. A stands for non-barred, B for barred and AB if unsure. ^(g) Ratio between the semi-minor and semi-major axis based on a detailed re-analysis of the SDSS images (see W14 for details). ^(h) Morphological classification of this particular galaxy NGC 4676B from Wild et al. (2014).

Table 6. CALIFA DR2 quality control parameters for the V500 data

ID ^a	airmass ^b	$\mu_{V,sky}$ ^c	A_V ^d	seeing ^e	flags(O) ^f	δ_λ ^g	S/N(R_{50}) ^h	$I_{3\sigma}$ ⁱ	flags(R) ^j	$\left(\frac{g_{CALIFA}}{g_{SDSS}}\right)^k$	$\left(\frac{r_{CALIFA}}{r_{SDSS}}\right)^l$	flags(C) ^m
001*	1.02 ± 0.01	21.4	0.18	...	000	4.68	24.8	24.0 0.9	00000	1.04	1.03	000
002	1.41 ± 0.05	20.9	00-	4.63	28.9	23.7 1.2	00000	0.96	0.98	000
003*	1.01 ± 0.01	20.8	0.23	0.8 ± 0.1	000	5.17	12.8	23.7 1.2	00100	0.92	0.97	100
005	1.40 ± 0.01	21.0	00-	4.65	24.3	23.6 1.3	00000	0.99	1.01	000
007*†	1.34 ± 0.05	20.5	00-	5.21	27.6	23.5 1.4	10100	1.03	1.05	000
008	1.34 ± 0.07	21.0	0.20	...	000	4.63	29.1	23.7 1.1	00000	1.02	0.99	000
010*	1.31 ± 0.05	21.0	0.22	...	000	4.62	18.2	23.7 1.2	00000	1.01	0.98	000
013	1.57 ± 0.10	20.8	0.19	...	000	4.63	31.5	23.6 1.3	-00-0	0.96	1.01	001
014*	1.26 ± 0.04	21.0	0.21	...	000	4.62	22.0	23.8 1.1	00000	1.03	1.01	000
017	1.23 ± 0.03	21.1	00-	4.61	9.2	23.6 1.3	00000	1.00	1.00	000
022	1.18 ± 0.05	20.9	00-	4.76	24.8	23.6 1.3	10000	0.94	0.94	100
023	1.86 ± 0.03	19.7	0.15	...	110	4.87	14.6	22.8 2.7	10011	0.92	0.98	000
025	1.24 ± 0.04	21.0	0.17	...	000	4.63	17.9	23.6 1.3	00000	0.98	1.02	001
026	1.26 ± 0.02	20.9	0.13	...	000	4.82	26.3	23.8 1.1	00000	0.99	1.00	000
027	1.90 ± 0.01	20.1	0.20	...	110	4.71	30.3	23.5 1.5	00010	1.00	1.04	001
030	1.34 ± 0.04	20.9	0.20	...	000	4.65	30.1	23.9 1.0	00000	0.99	1.04	101
037	1.58 ± 0.11	20.8	0.17	...	000	4.68	34.7	24.0 0.9	00000	1.20	1.25	101
039*	1.03 ± 0.01	20.8	0.23	0.9 ± 0.1	000	5.21	15.6	23.8 1.1	01000	0.95	0.99	110
040	1.29 ± 0.06	21.1	0.17	...	000	4.69	24.4	24.0 0.9	00000	0.99	1.00	010
041	1.09 ± 0.03	21.1	0.14	...	000	4.95	21.0	23.8 1.1	00010	1.02	1.01	000
042*	1.10 ± 0.03	21.0	0.13	...	000	5.21	14.3	23.6 1.3	10000	1.08	1.09	101
043*	1.01 ± 0.01	21.3	0.19	...	000	4.79	29.5	23.9 1.0	-00-0	1.05	1.02	001
044	1.17 ± 0.04	21.0	00-	4.79	22.3	23.2 1.8	00001	0.96	0.96	000
045	1.28 ± 0.06	20.8	0.14	...	000	5.22	12.6	23.3 1.7	10000	0.98	1.03	001
050	1.43 ± 0.08	20.9	0.16	...	000	4.89	37.7	23.7 1.2	00000	0.99	1.02	000
053*	1.19 ± 0.04	20.7	...	0.8 ± 0.1	00-	5.25	27.4	23.7 1.2	00100	0.95	0.98	000
072	1.16 ± 0.03	21.1	0.15	...	000	4.84	27.3	23.8 1.1	00000	1.00	1.02	000
073*	1.04 ± 0.01	21.1	0.20	...	000	4.73	18.6	23.3 1.8	00000	1.01	1.01	000
076	1.15 ± 0.03	21.2	0.12	...	000	4.95	16.4	23.4 1.6	10000	0.96	0.97	111
077	1.43 ± 0.07	20.9	0.19	...	000	4.64	37.1	23.9 1.0	00000	1.05	1.11	101
088*	1.13 ± 0.03	20.8	...	1.0 ± 0.4	00-	5.43	23.7	23.4 1.5	01100	0.97	0.99	101
100*	1.37 ± 0.26	20.7	0.14	...	100	5.24	23.5	23.1 2.1	10001	0.99	1.00	001
103	1.42 ± 0.08	20.9	0.19	...	000	4.69	28.3	23.6 1.3	00000	1.01	1.05	001
104	1.62 ± 0.10	20.8	00-	4.73	9.4	23.6 1.3	00000	1.01	1.00	000
115	1.28 ± 0.02	20.6	00-	4.67	16.6	23.6 1.3	00010	0.98	0.99	000
127*	1.22 ± 0.02	20.6	0.28	0.9 ± 0.1	000	5.12	11.1	23.0 2.2	00001	0.93	0.98	000
131	1.20 ± 0.01	21.0	00-	4.72	22.2	23.3 1.8	00000	0.98	0.97	000
133	1.17 ± 0.02	20.6	0.28	0.8 ± 0.1	000	5.13	13.8	23.1 2.1	00001	0.88	0.95	100
134	1.47 ± 0.04	21.0	00-	5.26	20.9	23.2 1.9	10101	0.88	0.93	101
141	1.42 ± 0.03	21.0	00-	4.72	11.3	23.8 1.1	00000	1.01	0.97	111
146*†	1.47 ± 0.00	20.7	0.12	...	000	5.79	15.4	23.0 2.2	01101	1.03	1.02	001
147	1.15 ± 0.01	21.2	0.14	...	000	5.63	22.7	23.2 1.8	01101	0.98	1.00	100
148	1.34 ± 0.04	20.9	0.11	...	000	5.01	17.0	23.6 1.2	10000	1.04	0.93	101
149	1.14 ± 0.01	21.4	00-	5.78	24.8	22.9 2.4	11101	0.86	0.91	101
150	1.01 ± 0.01	21.1	00-	4.76	24.0	23.8 1.1	00000	1.00	0.98	010
151*	1.07 ± 0.02	21.0	0.15	...	000	5.85	18.7	23.0 2.2	11001	0.88	0.91	101
153	1.19 ± 0.04	21.1	00-	4.90	25.6	23.7 1.2	00000	0.98	0.99	000
155*	1.03 ± 0.01	21.1	0.16	...	000	5.61	14.8	23.1 2.0	11001	0.94	0.94	001
156*	1.12 ± 0.04	21.0	0.16	...	000	5.54	19.4	23.3 1.7	11000	0.99	1.00	001
165	1.03 ± 0.01	21.1	0.15	...	000	5.98	23.6	23.0 2.2	11001	0.92	0.93	100
231	1.03 ± 0.01	21.2	00-	4.89	8.7	23.9 1.0	00000	1.00	0.99	000
232	1.07 ± 0.00	21.1	00-	4.70	17.1	23.6 1.3	00010	1.02	1.01	000
272	1.15 ± 0.01	21.1	00-	5.19	27.3	23.3 1.7	10000	0.97	0.97	000
273*	1.06 ± 0.01	21.1	0.14	...	000	5.33	21.5	23.6 1.3	00000	0.98	1.00	001
274*	1.18 ± 0.02	20.9	00-	4.92	30.1	23.7 1.2	00000	1.02	1.03	001
275	1.14 ± 0.00	21.0	00-	4.93	35.7	23.7 1.2	01000	0.99	1.01	000
277*	1.60 ± 0.12	20.3	0.33	...	011	5.65	15.9	22.8 2.8	11101	0.95	1.01	101
278	1.32 ± 0.08	20.8	0.12	...	000	5.33	25.8	23.6 1.3	00100	1.04	1.05	000
306*	1.28 ± 0.08	20.6	0.17	1.0 ± 0.1	000	4.59	6.5	23.6 1.4	00010	1.01	0.96	101
307*	1.06 ± 0.01	21.2	0.16	...	000	5.64	14.3	23.5 1.4	01000	0.97	0.97	001

Table 6. continued.

ID ^a	airmass ^b	$\mu_{V,\text{sky}}^c$	A_V^d	seeing ^e	flags(O) ^f	δ_λ^g	S/N(R_{50}) ^h	$I_{3\sigma}^i$	flags(R) ^j	$\left(\frac{g_{\text{CALIFA}}}{g_{\text{SDSS}}}\right)^k$	$\left(\frac{r_{\text{CALIFA}}}{r_{\text{SDSS}}}\right)^l$	flags(C) ^m
309*	1.27 ± 0.05	21.0	0.15	...	000	5.97	12.8	23.1 2.1	11001	0.99	0.99	001
311	1.03 ± 0.01	21.3	0.16	...	000	5.96	7.1	23.0 2.2	11001	0.87	0.86	101
314	1.13 ± 0.05	21.1	0.15	1.1 ± 0.1	000	4.99	31.1	24.0 0.9	00000	1.05	1.07	001
319*	1.11 ± 0.03	20.5	0.56	...	001	5.54	21.7	23.3 1.8	01100	0.91	1.00	001
326*	1.05 ± 0.01	20.8	00-	4.66	24.8	23.9 1.0	00000	1.00	1.02	000
340	1.27 ± 0.05	20.9	...	1.1 ± 0.2	00-	5.21	12.7	23.8 1.1	01000	0.93	0.95	100
341*	1.17 ± 0.03	...	0.17	1.5 ± 0.2	0-0	5.06	17.0	23.7 1.2	00000	1.01	1.03	000
353	1.03 ± 0.02	20.9	00-	4.74	20.8	23.3 1.7	00000	0.98	1.00	001
364*	1.33 ± 0.07	20.8	0.12	...	000	5.39	34.0	23.8 1.1	00100	1.01	1.05	000
381	1.01 ± 0.00	21.2	00-	4.77	32.5	23.9 1.0	00000	1.04	1.03	001
388	1.02 ± 0.01	21.1	...	0.2 ± 0.2	00-	5.18	7.8	23.2 1.9	00001	0.95	0.94	000
436	1.13 ± 0.03	21.1	0.19	...	000	...	21.7	23.1 2.1	0-011	0.97	0.98	000
475*†	1.35 ± 0.07	20.8	0.12	...	000	5.36	21.2	23.7 1.2	00000	0.96	1.03	110
476	1.06 ± 0.02	20.8	00-	4.75	64.0	23.9 1.0	00010	1.01	1.03	100
479*	1.14 ± 0.03	20.8	00-	4.67	28.4	23.9 0.9	00010	1.02	1.03	000
486*	1.05 ± 0.03	...	0.16	1.2 ± 0.7	0-0	4.66	22.3	24.0 0.9	00000	0.99	0.98	000
502	1.11 ± 0.01	21.3	00-	5.04	40.3	24.0 0.9	00000	1.09	1.07	100
515*	1.01 ± 0.00	20.9	0.14	...	000	5.25	14.9	23.2 1.9	00001	0.95	0.98	000
518*	1.16 ± 0.01	20.9	0.15	...	000	5.64	18.6	23.3 1.7	01100	0.97	1.00	000
528*	1.14 ± 0.01	20.8	00-	4.71	7.5	23.7 1.2	00000	1.01	1.02	001
548*	1.16 ± 0.01	20.8	0.19	1.2 ± 0.1	000	4.64	43.6	23.8 1.1	00010	1.02	1.00	001
569	1.06 ± 0.01	21.2	00-	4.65	33.8	24.1 0.8	10000	0.96	1.01	000
577*†	1.02 ± 0.01	21.0	0.15	...	000	4.95	13.3	24.0 0.9	01100	-0-
592	1.03 ± 0.01	20.9	00-	4.69	20.0	23.3 1.7	00000	0.82	0.84	101
593	1.11 ± 0.02	21.0	00-	4.73	19.5	23.9 1.0	00000	0.98	0.99	000
606	1.07 ± 0.01	21.4	00-	5.19	15.8	23.9 1.0	00000	0.95	1.00	101
607*	1.22 ± 0.03	21.3	0.16	...	000	5.39	41.2	23.6 1.3	10000	0.91	0.92	100
608*	1.31 ± 0.06	21.1	00-	5.87	11.3	23.3 1.7	11000	0.91	0.91	101
609*	1.07 ± 0.02	21.3	0.14	...	000	5.55	17.3	23.8 1.1	01000	0.99	0.97	100
610*	1.11 ± 0.03	21.2	00-	5.85	22.7	23.5 1.5	11000	0.96	0.97	000
630	1.36 ± 0.04	20.0	01-	4.64	17.6	23.4 1.6	00000	0.99	1.00	001
633	1.13 ± 0.01	21.0	00-	4.77	13.8	23.7 1.2	00000	0.93	0.96	000
657*	1.02 ± 0.01	21.2	0.19	1.1 ± 0.1	000	4.69	10.4	23.9 1.0	00000	1.01	1.00	000
663*	1.20 ± 0.04	20.9	00-	5.32	24.4	23.7 1.2	01000	1.01	1.02	100
664*	1.04 ± 0.02	21.2	...	1.1 ± 0.1	00-	5.21	35.6	23.9 0.9	00000	1.05	1.06	000
665*	1.06 ± 0.01	21.1	00-	5.21	18.8	23.7 1.2	00000	1.02	1.03	100
676*	1.03 ± 0.03	21.0	0.15	...	000	5.52	12.5	23.2 1.8	-10-1	0.96	0.97	100
680*	1.07 ± 0.02	21.0	00-	4.66	11.8	24.1 0.8	00010	1.00	1.03	000
684*	1.05 ± 0.02	21.0	00-	4.66	25.1	23.5 1.5	00000	0.97	0.99	000
708	1.18 ± 0.03	20.8	00-	4.76	18.8	23.0 2.2	00011	0.93	0.95	000
714	1.09 ± 0.01	20.6	0.14	...	000	4.66	28.1	23.8 1.0	00010	1.03	1.02	000
715	1.10 ± 0.06	21.1	0.21	...	000	4.74	35.9	24.0 0.9	-00-0	1.02	1.04	101
740	1.12 ± 0.03	21.0	00-	4.66	30.0	23.3 1.7	00000	0.96	0.99	001
749	1.08 ± 0.02	21.1	0.19	1.1 ± 0.1	000	4.90	28.9	24.0 0.9	00000	1.03	1.04	100
758*	1.02 ± 0.00	21.1	0.24	1.1 ± 0.1	000	4.72	12.2	24.0 0.9	00000	0.96	0.97	000
764*	1.29 ± 0.05	21.1	0.18	1.0 ± 0.1	000	4.62	20.0	24.0 0.9	00000	1.07	1.02	000
769*	1.02 ± 0.01	21.2	00-	5.47	18.7	23.6 1.3	01100	1.00	1.00	000
778	1.15 ± 0.04	21.2	...	0.9 ± 0.1	00-	4.77	25.3	23.6 1.4	00000	0.99	1.00	000
783*	1.08 ± 0.02	21.3	0.16	...	000	5.46	29.3	23.6 1.3	00010	0.98	0.98	000
789	1.15 ± 0.03	21.1	0.20	0.9 ± 0.1	000	4.64	27.3	24.0 0.9	00010	0.99	0.99	000
791	1.16 ± 0.03	20.9	00-	4.78	35.6	23.5 1.4	00000	0.99	1.01	001
795	1.01 ± 0.00	21.1	...	0.8 ± 0.1	00-	4.71	27.7	23.9 1.0	00000	0.97	1.00	000
797*	1.05 ± 0.07	21.0	0.15	...	000	5.11	17.6	24.0 0.9	01100	0.99	1.00	000
798*	1.05 ± 0.02	21.3	0.21	...	000	4.66	27.0	24.3 0.7	00000	0.97	1.00	000
806*	1.00 ± 0.00	21.1	0.25	1.1 ± 0.1	000	4.70	59.9	23.6 1.3	00000	0.85	0.86	101
807	1.16 ± 0.04	20.9	00-	4.67	18.3	23.4 1.5	00010	0.99	1.00	100
809	1.35 ± 0.05	21.0	...	1.0 ± 0.5	00-	4.85	16.2	23.3 1.8	00000	0.84	0.87	101
813	1.08 ± 0.01	20.9	0.22	1.4 ± 0.1	000	4.65	19.4	23.6 1.4	00010	0.98	0.99	000
815	1.21 ± 0.05	21.1	0.18	0.8 ± 0.1	000	4.82	11.6	23.6 1.3	00000	0.96	0.98	000
816	1.21 ± 0.04	20.7	...	0.8 ± 0.1	00-	4.67	34.2	23.8 1.1	00010	1.02	1.02	001
820*	1.07 ± 0.02	21.2	0.17	...	000	5.61	7.2	22.9 2.5	21001	1.03	1.03	101

Table 6. continued.

ID ^a	airmass ^b	$\mu_{V,\text{sky}}^c$	A_V^d	seeing ^e	flags(O) ^f	δ_λ^g	S/N(R_{50}) ^h	$I_{3\sigma}^i$	flags(R) ^j	$\left(\frac{g_{\text{CALIFA}}}{g_{\text{SDSS}}}\right)^k$	$\left(\frac{r_{\text{CALIFA}}}{r_{\text{SDSS}}}\right)^l$	flags(C) ^m
822*	1.03 ± 0.01	21.2	00–	6.08	10.1	23.1 2.1	11001	0.96	0.96	101
823*	1.15 ± 0.00	20.9	0.19	...	000	4.62	21.3	23.8 1.1	10010	0.99	0.98	000
824*†	1.14 ± 0.01	20.9	00–	4.72	22.9	23.9 1.0	00000	0.92	0.89	101
826*	1.18 ± 0.03	21.1	00–	5.32	26.4	23.7 1.2	00100	1.03	1.04	000
828*	1.21 ± 0.03	21.3	0.26	0.9 ± 0.1	000	4.64	27.2	24.0 0.9	00000	1.11	1.04	101
829*	1.09 ± 0.01	21.2	0.18	...	000	4.73	17.7	23.4 1.6	10000	0.95	0.93	101
831	1.42 ± 0.07	20.2	01–	4.65	22.3	23.3 1.7	00000	1.03	1.02	000
832*	1.01 ± 0.01	21.3	00–	5.49	23.4	23.5 1.5	00100	0.98	0.99	100
833*	1.12 ± 0.03	21.2	0.18	0.9 ± 0.1	000	5.00	18.1	23.8 1.1	00100	1.02	0.98	000
834	1.39 ± 0.07	20.5	0.29	...	010	4.70	28.0	23.9 1.0	00000	1.17	1.23	101
835*	1.00 ± 0.00	21.1	...	1.1 ± 0.2	00–	5.28	38.2	24.0 0.9	01000	0.98	1.01	000
837*	1.11 ± 0.00	21.1	0.17	0.9 ± 0.1	000	4.84	43.0	24.1 0.8	01000	1.07	1.03	001
838	1.46 ± 0.09	20.3	01–	4.65	25.7	23.6 1.4	00000	1.06	1.06	000
840*	1.18 ± 0.04	21.0	0.28	0.9 ± 0.1	000	4.65	3.0	23.5 1.4	00000	1.02	0.96	100
841	1.16 ± 0.04	21.2	...	0.9 ± 0.1	00–	4.71	24.0	23.6 1.3	00000	1.01	1.03	001
843*	1.45 ± 0.09	21.0	0.23	0.8 ± 0.1	000	4.60	9.3	23.8 1.1	00000	1.08	1.05	011
845*	1.03 ± 0.02	21.4	0.19	...	000	4.64	16.0	23.8 1.1	00000	0.93	0.95	100
846*	1.06 ± 0.02	21.0	0.39	0.8 ± 0.1	001	4.64	7.7	23.7 1.2	00000	0.97	0.98	000
847*	1.31 ± 0.09	21.3	0.15	0.7 ± 0.1	010	4.66	20.4	24.0 0.9	20000	1.16	1.25	101
848*	1.10 ± 0.00	21.0	0.38	0.9 ± 0.1	001	4.74	32.3	23.8 1.1	00000	1.02	1.01	000
850*	1.05 ± 0.01	21.0	0.29	...	000	4.66	29.6	23.7 1.2	00000	1.00	1.01	000
851*	1.32 ± 0.04	20.5	0.41	0.7 ± 0.1	001	4.66	9.5	23.3 1.7	00010	0.93	0.93	100
852*	1.12 ± 0.01	21.0	0.36	0.9 ± 0.1	001	4.76	8.1	23.8 1.1	00000	1.01	0.99	000
854*	1.18 ± 0.03	20.7	0.42	0.9 ± 0.1	001	4.68	20.3	23.6 1.3	00010	1.00	1.01	001
856*	1.05 ± 0.02	21.2	0.17	...	000	4.61	24.1	23.9 1.0	00000	0.99	0.99	000
857*	1.08 ± 0.00	21.5	0.16	0.9 ± 0.1	000	4.67	36.7	24.2 0.8	00000	0.98	1.01	000
858*	1.10 ± 0.03	21.2	0.15	1.3 ± 0.2	000	4.67	15.8	23.7 1.2	00000	1.01	0.98	000
859*	1.16 ± 0.02	21.2	0.15	0.7 ± 0.1	000	4.67	11.0	23.6 1.4	00000	0.92	0.95	000
860*	1.04 ± 0.02	21.2	0.29	1.0 ± 0.1	000	4.60	41.5	23.6 1.3	00000	1.10	1.06	101
861	1.08 ± 0.02	21.1	00–	4.62	22.4	23.5 1.4	00000	1.04	1.06	001
862	1.13 ± 0.03	20.8	...	1.1 ± 0.2	00–	5.19	20.3	23.4 1.6	00100	0.99	1.01	001
863*	1.09 ± 0.01	21.4	0.16	0.7 ± 0.1	000	4.67	29.4	24.1 0.8	00000	1.02	1.05	001
864*	1.06 ± 0.01	20.9	0.28	...	000	4.70	12.2	23.5 1.5	20010	0.99	0.98	100
865*	1.01 ± 0.01	21.2	0.25	...	000	4.71	32.4	23.9 1.0	10000	1.01	1.02	001
866*	1.04 ± 0.02	21.3	0.21	1.1 ± 0.1	000	4.64	12.6	24.0 0.9	20000	1.04	1.02	000
867*	1.13 ± 0.01	21.2	0.21	1.1 ± 0.1	000	4.69	39.2	24.0 0.9	10000	1.08	1.09	001
868	1.65 ± 0.04	20.1	01–	4.84	25.3	23.3 1.7	–00–0	0.96	0.99	001
869	1.41 ± 0.06	20.8	0.19	1.1 ± 0.1	000	4.66	16.4	23.5 1.5	00000	1.04	1.02	101
871	1.38 ± 0.01	20.6	0.17	0.9 ± 0.1	000	4.70	21.3	23.4 1.6	–00–0	0.99	1.02	100
872*	1.28 ± 0.01	20.9	0.15	0.6 ± 0.1	000	4.66	18.2	23.4 1.5	00010	0.98	0.98	000
874*	1.10 ± 0.02	21.0	0.22	...	000	4.75	24.4	23.2 1.9	00001	1.01	1.03	101
877*†	1.24 ± 0.05	21.0	0.22	...	000	4.72	16.8	23.6 1.3	20000	1.23	1.23	101
878*	1.33 ± 0.01	20.9	0.22	0.9 ± 0.1	000	4.59	6.8	23.7 1.1	00010	1.01	0.99	101
880	1.24 ± 0.03	20.7	0.29	0.9 ± 0.1	000	4.63	24.2	23.6 1.3	00010	0.93	0.94	100
881*	1.10 ± 0.00	21.1	0.15	0.8 ± 0.1	000	4.67	18.2	23.8 1.1	00010	0.94	0.94	000
883*	1.10 ± 0.01	21.2	0.17	1.0 ± 0.2	000	4.63	10.1	23.6 1.3	00000	0.99	0.95	101
884	1.66 ± 0.10	20.4	01–	4.90	10.8	23.4 1.5	00000	0.97	0.98	110
885	1.25 ± 0.04	20.9	0.20	0.7 ± 0.1	000	4.88	25.4	23.7 1.2	00100	1.04	1.01	001
886	1.29 ± 0.04	21.0	0.17	0.9 ± 0.2	000	4.65	40.5	23.4 1.5	00000	1.01	1.00	000
887*	1.08 ± 0.02	21.3	0.17	0.9 ± 0.1	000	4.67	31.9	23.9 1.0	00000	1.01	0.98	001
888*	1.01 ± 0.01	20.9	0.22	...	000	4.68	2.5	23.5 1.5	00010	0.93	0.94	000
890*	1.08 ± 0.02	21.0	0.22	...	000	4.71	29.9	23.9 1.0	00010	1.00	1.01	000
891	1.37 ± 0.06	20.3	0.21	1.2 ± 0.2	010	5.23	9.2	23.1 2.0	00101	0.91	0.98	000
893*	1.35 ± 0.07	20.5	0.20	1.0 ± 0.1	000	5.32	6.9	22.9 2.6	20111	0.89	0.92	111
894	1.31 ± 0.06	20.5	...	0.9 ± 0.1	00–	4.74	21.3	23.6 1.3	00010	1.06	1.11	101
895	1.15 ± 0.03	20.5	0.22	1.1 ± 0.1	000	5.15	10.3	23.5 1.4	00000	0.94	0.97	100
896*	1.36 ± 0.08	20.8	0.18	0.9 ± 0.1	000	5.01	21.8	23.8 1.1	00100	1.04	1.02	001
898	1.60 ± 0.11	20.4	...	0.9 ± 0.1	01–	4.66	12.4	22.9 2.5	00011	0.97	1.00	000
901*	1.10 ± 0.03	21.3	0.14	1.0 ± 0.1	000	4.63	29.9	23.7 1.2	20000	0.97	1.03	101
902*	1.10 ± 0.00	21.2	0.17	0.8 ± 0.1	000	4.71	39.3	23.6 1.3	00000	1.06	1.01	001
903	1.45 ± 0.08	20.9	00–	4.64	30.5	23.3 1.8	00000	0.97	0.97	001

Table 6. continued.

ID ^a	airmass ^b	$\mu_{V,\text{sky}}^c$	A_V^d	seeing ^e	flags(O) ^f	δ_λ^g	S/N(R_{50}) ^h	$I_{3\sigma}^i$	flags(R) ^j	$\left(\frac{g_{\text{CALIFA}}}{g_{\text{SDSS}}}\right)^k$	$\left(\frac{r_{\text{CALIFA}}}{r_{\text{SDSS}}}\right)^l$	flags(C) ^m
904*	1.20 ± 0.04	21.0	0.17	0.9 ± 0.1	000	4.71	21.5	23.6 1.4	00000	1.01	0.98	000
909	1.09 ± 0.02	20.8	00–	5.05	29.5	23.8 1.1	00000	1.02	1.00	000
910	1.22 ± 0.03	21.1	00–	4.62	18.7	23.4 1.6	00000	0.99	1.01	101
913	1.47 ± 0.09	21.1	00–	4.63	38.8	23.4 1.6	00000	0.96	1.01	100
914	1.18 ± 0.02	21.0	0.13	...	000	4.79	31.4	23.8 1.1	00000	0.98	1.00	000
915	1.28 ± 0.05	21.1	00–	4.61	25.4	23.4 1.6	00000	1.06	1.03	000
916	1.55 ± 0.10	20.8	00–	4.65	25.0	23.0 2.2	00001	0.95	0.99	101
917	1.21 ± 0.03	20.9	00–	4.69	31.5	23.5 1.4	00010	1.03	1.00	100
922	1.15 ± 0.00	20.8	0.14	...	000	5.20	16.8	23.5 1.5	00100	1.06	1.08	101
924	1.43 ± 0.12	20.6	00–	4.79	12.8	23.0 2.3	–00–1	1.01	1.00	000
927	1.29 ± 0.03	21.0	00–	4.64	14.7	23.8 1.1	00000	1.01	1.02	000
930	1.29 ± 0.03	20.8	00–	4.62	7.3	23.1 2.1	00011	1.03	1.04	010
932	1.27 ± 0.02	21.0	00–	4.71	33.5	23.7 1.2	00000	1.00	1.00	100
935*	1.04 ± 0.02	21.0	...	1.1 ± 0.1	00–	5.09	11.1	23.7 1.2	00000	0.96	1.00	000
936	1.42 ± 0.05	20.8	0.15	...	000	4.84	30.7	24.0 0.9	00000	1.06	1.11	101
937	1.13 ± 0.02	21.0	00–	4.62	13.8	23.7 1.2	00010	0.99	0.97	000
938	1.01 ± 0.01	...	0.16	...	0–0	4.74	31.5	24.0 0.9	00000	0.98	1.00	100
939*	1.11 ± 0.04	20.8	0.15	...	000	4.99	8.7	23.6 1.3	01110	1.05	1.03	100

Notes. We describe the meaning of each column including the identifier of each column in the electronic table available on the DR2 web page. ^(a) IDs marked with an asterisk were already part of the DR1. A dagger indicates cubes that were registered with the old method of the pipeline V1.3c. ^(b) Mean airmass (OBS_AIR_MEAN) and rms (OBS_AIR_RMS) of the observations for the frames used to create the considered datacube. ^(c) Average night-sky surface brightness (OBS_SKY_MAG) in the V band during the observations in units of mag arcsec⁻². ^(d) Average night-sky attenuation (OBS_EXT_MEAN) in the V band during the observations in magnitudes. ^(e) Average natural seeing (OBS_SEEING_MEAN) in the V-band during the observations in arcsec (FWHM). ^(f) Observation quality flags, combining the three individual column flags (FLAG_OBS_AM, FLAG_OBS_SKYMAG, FLAG_OBS_EXT) as described in Sect. 5. ^(g) Average spectral resolution (RED_DISP_MEAN) in Å (FWHM), measured by fitting the night-sky emission lines with single Gaussian functions. ^(h) Average signal-to-noise ratio (CAL_SNR1HLR) estimated for the full wavelength range at one half light radius from the center. ⁽ⁱ⁾ Average flux at the 3σ continuum detection limit in units of V-band mag arcsec⁻² and in units of 10^{-18} erg s⁻¹ cm⁻² Å⁻¹ arcsec⁻². ^(j) Reduction/instrumental performance quality flags, combining the five individual column flags (FLAG_RED_STRAYLIGHT, FLAG_RED_DISP, FLAG_RED_CDISP, FLAG_RED_SKYLINES, FLAG_RED_LIMSB) as described in Sect. 5. ^(k) Ratio between the SDSS g band flux derived from the datacube and the one derived from the SDSS images for a 30''-diameter aperture (CAL_QFLUX_G). ^(l) Ratio between the SDSS r band flux derived from the datacube and the one derived from the SDSS images for a 30''-diameter aperture (CAL_QFLUX_R). ^(m) Quality control flags, combining the three individual column flags (FLAG_CAL_SPECPHOTO, FLAG_CAL_WL, FLAG_CAL_IMA) as described in Sect. 5.

Table 7. CALIFA DR2 quality control parameters for the V1200 data

ID ^a	airmass ^b	$\mu_{V,sky}$ ^c	A_V ^d	seeing ^e	flags(O) ^f	δ_λ ^g	S/N(R_{50}) ^h	$I_{3\sigma}$ ⁱ	flags(R) ^j	flags(C) ^k
001*	1.01 ± 0.02	...	0.26	...	0-0	1.90	9.0	23.2 3.3	00000	000
002	1.32 ± 0.04	21.8	0.13	...	000	1.94	12.4	23.3 3.0	00000	000
003*	1.08 ± 0.06	22.0	0.17	...	000	1.96	6.5	23.3 2.9	11000	000
005	1.44 ± 0.05	21.8	0.16	...	000	1.94	13.2	23.4 2.8	-00-0	100
007*†	1.18 ± 0.02	21.7	0.14	...	000	1.96	10.2	22.8 4.9	00000	001
008	1.04 ± 0.03	21.9	0.43	...	001	1.90	10.2	23.2 3.3	00010	000
010*	1.29 ± 0.09	22.2	00-	1.92	6.1	23.0 4.1	00000	001
013	1.53 ± 0.04	21.8	0.14	...	000	1.94	16.0	23.4 2.9	00010	100
014*	1.27 ± 0.08	22.2	0.19	...	000	1.90	11.4	23.3 3.0	00000	000
017	1.19 ± 0.03	21.9	00-	1.94	4.4	23.5 2.5	00000	001
022	1.12 ± 0.08	22.4	0.15	...	000	1.99	6.2	22.7 5.3	-00-0	001
023	1.89 ± 0.07	1---	1.96	8.7	22.9 4.3	10010	000
025	1.22 ± 0.06	22.0	0.15	...	000	1.94	8.5	23.1 3.5	00010	101
026	1.27 ± 0.03	21.8	00-	1.91	10.5	23.4 2.7	00010	000
027	1.93 ± 0.05	21.3	0.13	...	110	1.95	14.0	23.2 3.2	10000	101
030	1.28 ± 0.03	21.9	0.14	...	000	1.94	17.2	23.7 2.1	00000	001
037	1.02 ± 0.01	22.2	00-	1.93	15.7	23.7 2.0	00010	001
039*	1.07 ± 0.04	22.1	0.21	1.1 ± 0.2	000	1.96	9.3	23.6 2.3	01000	000
040	1.03 ± 0.03	22.2	0.21	...	000	1.93	11.0	23.5 2.5	00000	000
041	1.02 ± 0.02	22.3	00-	1.90	9.9	23.5 2.6	00000	000
042*	1.19 ± 0.09	22.3	0.15	0.9 ± 0.1	000	2.01	9.1	23.6 2.3	01000	101
043*	1.01 ± 0.01	22.3	0.27	...	000	1.90	11.1	23.4 2.7	00000	000
044	1.05 ± 0.04	22.4	0.11	...	000	1.97	7.4	22.7 5.3	00110	000
045	1.01 ± 0.01	22.4	0.14	1.2 ± 0.2	000	1.99	9.2	23.5 2.4	00000	001
050	1.14 ± 0.07	22.3	0.14	...	000	2.06	16.2	23.2 3.3	01000	101
053*	1.33 ± 0.17	21.9	0.16	...	100	2.13	10.3	23.1 3.5	01110	000
072	1.13 ± 0.04	21.9	0.12	...	000	1.94	11.4	23.4 2.8	00000	000
073*	1.08 ± 0.04	22.2	0.26	...	000	1.91	7.2	22.9 4.3	00000	001
076	1.23 ± 0.08	22.2	0.11	...	000	2.09	4.6	22.6 5.6	01100	001
077	1.17 ± 0.01	21.8	00-	1.94	17.3	23.6 2.3	00010	001
088*	1.31 ± 0.13	21.4	0.21	...	010	1.99	9.1	22.7 5.1	01100	011
100*	1.36 ± 0.14	21.8	0.15	1.1 ± 0.1	000	2.00	13.2	23.1 3.7	01000	001
103	1.09 ± 0.09	22.2	00-	2.01	11.3	22.8 4.8	01100	001
104	1.26 ± 0.03	21.9	0.14	...	000	1.94	5.0	23.5 2.6	00000	001
115	1.34 ± 0.09	22.1	0.15	...	000	2.01	5.3	22.7 5.2	01100	101
127*	1.37 ± 0.27	21.7	0.15	...	100	1.99	4.2	22.5 6.4	-00-1	000
131	1.19 ± 0.00	22.3	0.14	...	000	1.99	7.0	22.3 7.7	-00-1	000
133	1.13 ± 0.01	21.9	0.16	...	000	2.00	5.5	22.5 6.4	-10-1	101
134	1.37 ± 0.01	22.0	00-	2.00	10.0	23.1 3.5	01000	000
141	1.37 ± 0.02	22.0	0.15	...	000	1.98	5.1	23.0 4.1	00100	001
146*†	1.48 ± 0.01	22.2	0.14	1.3 ± 0.2	000	2.00	10.7	23.3 2.9	01000	001
147	1.16 ± 0.02	22.3	0.14	1.1 ± 0.1	000	1.95	16.3	23.6 2.3	00010	001
148	1.29 ± 0.06	22.1	0.12	...	000	1.93	8.2	23.4 2.7	00000	001
149	1.27 ± 0.06	22.2	0.11	...	000	1.92	13.2	23.0 4.1	10000	001
150	1.06 ± 0.04	22.2	0.15	...	000	1.93	12.4	23.3 3.0	10000	000
151*	1.52 ± 0.19	21.4	11-	2.04	9.7	22.9 4.4	01100	001
153	1.09 ± 0.03	21.6	00-	1.97	10.7	23.1 3.4	-00-0	001
155*	1.09 ± 0.05	22.1	0.13	0.9 ± 0.1	000	2.33	4.8	22.5 6.2	21110	001
156*	1.08 ± 0.05	22.3	0.14	...	000	2.36	8.1	22.6 5.6	01100	001
165	1.25 ± 0.11	21.7	00-	1.94	15.7	23.1 3.5	00100	000
231	1.06 ± 0.03	22.3	00-	1.92	5.4	23.5 2.5	10000	001
232	1.31 ± 0.12	21.9	0.11	...	000	1.96	9.8	23.5 2.4	00010	101
272	1.13 ± 0.03	22.1	00-	2.09	9.2	22.8 5.0	01010	000
273*	1.06 ± 0.01	22.2	0.14	1.1 ± 0.1	000	2.01	12.6	23.6 2.3	01000	000
274*	1.30 ± 0.09	22.0	00-	2.05	10.7	23.0 4.0	01100	000
275	1.16 ± 0.02	22.4	0.15	...	000	1.99	9.2	22.4 6.7	-00-1	000
277*	1.08 ± 0.04	21.7	0.15	...	000	2.13	12.0	23.0 4.0	01010	001
278	1.09 ± 0.05	22.5	0.11	...	000	2.24	7.4	22.8 4.8	01100	100
306*	1.14 ± 0.03	21.3	01-	2.02	3.5	23.2 3.4	21100	001
307*	1.20 ± 0.08	22.2	0.15	0.8 ± 0.1	000	2.33	4.8	22.7 5.2	11100	001

Table 7. continued.

ID ^a	airmass ^b	$\mu_{V,\text{sky}}^c$	A_V^d	seeing ^e	flags(O) ^f	δ_i^g	S/N(R_{50}) ^h	$I_{3\sigma}^i$	flags(R) ^j	flags(C) ^k
309*	1.25 ± 0.08	22.1	0.14	...	000	2.38	6.3	22.8 4.8	01100	000
311	1.03 ± 0.03	22.4	00-	2.02	4.2	22.9 4.3	01100	000
314	1.05 ± 0.01	22.4	0.12	...	000	1.92	11.5	23.2 3.3	-00-0	001
319*	1.07 ± 0.06	22.2	0.15	1.1 ± 0.1	000	1.99	12.5	23.6 2.3	-01-0	000
326*	1.29 ± 0.05	21.9	00-	2.02	5.4	22.7 5.0	01100	001
340	1.08 ± 0.02	22.5	00-	2.01	4.0	23.0 3.9	01100	001
341*	1.21 ± 0.08	22.0	0.16	1.2 ± 0.1	000	1.91	7.9	23.4 2.7	00100	001
353	1.04 ± 0.03	22.5	0.10	...	000	2.07	9.4	23.3 2.9	01010	001
364*	1.02 ± 0.02	22.1	...	0.9 ± 0.1	00-	2.03	15.8	23.3 2.9	11000	001
381	1.01 ± 0.01	22.2	00-	1.96	12.4	23.6 2.4	-00-0	000
388	1.33 ± 0.11	22.1	00-	2.15	2.3	22.4 6.7	01111	101
436	1.10 ± 0.03	21.4	01-	1.96	11.1	23.0 3.9	-00-0	001
475*†	1.13 ± 0.07	22.1	00-	2.03	11.6	23.3 2.9	21010	101
476	1.40 ± 0.28	21.8	10-	2.02	25.5	22.9 4.5	01100	001
479*	1.16 ± 0.03	22.3	00-	2.05	7.2	22.7 5.3	01100	001
486*	1.21 ± 0.10	22.1	0.15	0.8 ± 0.1	000	1.99	8.6	23.5 2.5	10100	100
502	1.23 ± 0.08	21.9	00-	1.93	11.6	22.5 6.1	00000	001
515*	1.20 ± 0.09	22.3	0.15	0.9 ± 0.1	000	2.30	4.2	22.6 5.5	11110	000
518*	1.18 ± 0.03	22.6	0.13	...	000	2.03	12.6	23.3 2.9	01100	000
528*	1.48 ± 0.08	22.0	00-	2.10	2.0	22.7 5.5	01100	110
548*	1.21 ± 0.05	21.9	0.18	0.8 ± 0.1	000	2.00	14.6	23.2 3.3	10000	100
569	1.16 ± 0.05	22.0	0.15	...	000	1.95	15.0	23.5 2.4	00000	001
577*†	1.06 ± 0.04	22.2	0.22	...	000	1.89	6.5	23.6 2.3	00100	00-
592	1.03 ± 0.02	22.3	00-	2.25	4.9	22.6 5.5	01100	000
593	1.15 ± 0.05	21.9	00-	1.95	8.3	23.5 2.6	00000	010
606	1.33 ± 0.09	22.1	0.17	...	000	1.94	10.4	23.6 2.3	00000	001
607*	1.25 ± 0.07	22.3	0.14	...	000	2.25	16.7	23.1 3.7	01000	000
608*	1.20 ± 0.10	21.9	0.16	...	000	1.92	6.3	23.2 3.3	00000	000
609*	1.08 ± 0.05	22.4	0.15	0.8 ± 0.1	000	2.28	6.8	23.0 3.9	11100	011
610*	1.17 ± 0.07	22.5	00-	2.14	8.9	23.0 4.1	11100	100
630	1.26 ± 0.06	22.4	00-	1.92	10.7	23.3 2.9	00000	000
633	1.55 ± 0.12	22.0	00-	1.92	4.3	23.2 3.3	00010	000
657*	1.09 ± 0.05	22.4	0.19	1.5 ± 0.2	000	1.90	5.3	23.7 2.1	00000	000
663*	1.10 ± 0.02	22.0	00-	1.98	11.8	23.3 2.9	01000	001
664*	1.07 ± 0.04	22.0	0.26	1.2 ± 0.1	000	1.96	16.2	23.4 2.7	00000	001
665*	1.17 ± 0.10	22.1	0.10	...	000	1.95	5.1	22.8 4.6	00000	001
676*	1.01 ± 0.02	22.5	0.17	0.8 ± 0.1	000	2.26	4.6	22.9 4.2	01100	001
680*	1.07 ± 0.05	22.4	0.10	...	000	1.95	5.4	23.7 2.0	00000	000
684*	1.06 ± 0.04	22.3	0.13	0.9 ± 0.1	000	1.96	13.0	23.4 2.8	00000	001
708	1.12 ± 0.04	22.2	00-	1.91	7.7	23.0 4.0	00010	000
714	1.43 ± 0.12	21.9	00-	1.93	12.6	23.4 2.7	-00-0	001
715	1.18 ± 0.06	21.9	0.22	...	000	2.00	18.7	23.6 2.3	00000	001
740	1.05 ± 0.04	22.8	00-	2.24	4.4	22.2 8.3	01011	001
749	1.07 ± 0.04	22.3	00-	2.06	13.2	23.4 2.7	11010	001
758*	1.18 ± 0.05	22.2	0.26	1.0 ± 0.1	001	1.89	5.5	23.4 2.7	-00-0	100
764*	1.11 ± 0.04	...	0.16	...	0-0	2.02	7.7	23.6 2.4	01100	001
769*	1.03 ± 0.02	22.2	00-	2.00	9.6	23.3 3.1	01000	000
778	1.02 ± 0.01	22.5	00-	2.13	8.8	23.2 3.3	01000	000
783*	1.20 ± 0.07	22.3	0.17	...	000	2.29	11.3	22.9 4.2	01000	000
789	1.10 ± 0.05	22.1	00-	1.95	12.4	23.5 2.6	00000	000
791	1.08 ± 0.02	22.6	00-	2.28	9.0	22.7 5.1	01110	001
795	1.23 ± 0.09	22.3	00-	1.92	12.3	23.5 2.6	00000	000
797*	1.06 ± 0.04	22.5	0.17	1.3 ± 0.2	000	1.89	8.4	23.6 2.4	00000	000
798*	1.13 ± 0.07	22.2	0.30	0.8 ± 0.1	001	1.93	8.1	23.4 2.8	00000	001
806*	1.06 ± 0.05	22.2	0.21	1.1 ± 0.1	000	1.90	29.0	23.5 2.4	00010	000
807	1.30 ± 0.19	22.0	10-	1.96	9.8	23.5 2.5	-00-0	001
809	1.30 ± 0.08	21.7	00-	1.95	8.2	23.2 3.2	00010	001
813	1.07 ± 0.02	22.3	00-	2.05	8.7	23.1 3.7	01010	000
815	1.15 ± 0.10	22.2	00-	2.05	3.8	23.1 3.7	-10-0	001
816	1.15 ± 0.06	22.2	00-	2.08	12.1	23.3 3.0	11010	001
820*	1.15 ± 0.10	22.3	0.15	0.7 ± 0.1	000	2.35	4.3	22.7 5.4	-11-0	101

Table 7. continued.

ID ^a	airmass ^b	$\mu_{V,\text{sky}}^c$	A_V^d	seeing ^e	flags(O) ^f	δ_i^g	S/N(R_{50}) ^h	$I_{3\sigma}^i$	flags(R) ^j	flags(C) ^k
822*	1.09 ± 0.05	22.1	0.16	0.8 ± 0.1	000	1.91	7.4	23.4 2.9	00000	000
823*	1.17 ± 0.03	22.0	0.26	0.9 ± 0.1	000	1.91	10.3	23.3 3.1	00000	001
824*†	1.18 ± 0.04	21.6	0.24	1.1 ± 0.2	000	1.98	6.4	22.6 5.7	00000	001
826*	1.16 ± 0.04	22.0	00-	2.10	10.9	22.9 4.5	-11-0	001
828*	1.17 ± 0.04	22.6	0.16	1.0 ± 0.1	000	1.89	12.4	23.6 2.2	10000	000
829*	1.24 ± 0.07	22.0	0.17	1.4 ± 0.2	000	1.95	7.1	23.3 2.9	01110	000
831	1.18 ± 0.05	21.3	0.17	...	010	1.95	12.5	23.1 3.6	10000	000
832*	1.02 ± 0.02	22.1	00-	2.00	10.4	23.4 2.9	-10-0	001
833*	1.07 ± 0.03	22.2	0.10	...	000	1.95	4.6	22.9 4.4	00000	001
834	1.27 ± 0.10	22.3	0.23	...	000	2.04	10.5	23.5 2.5	01010	001
835*	1.04 ± 0.03	22.3	0.16	1.0 ± 0.1	000	1.95	16.8	23.6 2.2	00000	000
837*	1.15 ± 0.04	22.2	0.14	0.8 ± 0.1	000	1.98	22.1	23.6 2.3	00100	001
838	1.32 ± 0.12	21.9	00-	2.03	14.6	23.4 2.7	01010	001
840*	1.24 ± 0.09	22.1	0.10	...	000	1.95	1.8	23.2 3.2	00000	000
841	1.40 ± 0.09	21.8	0.15	...	000	1.94	9.5	23.1 3.6	-00-0	000
843*	1.11 ± 0.05	22.4	0.26	...	000	1.92	5.6	23.5 2.6	00000	001
845*	1.19 ± 0.15	21.7	0.28	0.8 ± 0.1	100	1.93	4.5	23.2 3.3	-00-0	000
846*	1.17 ± 0.07	22.0	0.25	...	000	1.95	3.3	23.3 2.9	00000	000
847*	1.03 ± 0.03	21.9	0.32	0.8 ± 0.1	001	1.93	7.9	23.1 3.5	00010	001
848*	1.24 ± 0.12	...	0.28	1.0 ± 0.1	0-1	1.88	13.9	23.2 3.3	-00-0	001
850*	1.05 ± 0.02	22.0	0.19	0.8 ± 0.1	000	1.93	12.3	23.3 3.0	00000	000
851*	1.12 ± 0.04	22.1	0.28	0.9 ± 0.1	000	1.89	5.0	23.2 3.4	00000	000
852*	1.38 ± 0.09	21.6	0.19	1.4 ± 0.2	000	1.99	3.6	23.4 2.7	01100	001
854*	1.20 ± 0.06	22.0	0.37	0.9 ± 0.1	001	1.88	9.0	23.2 3.3	20000	001
856*	1.05 ± 0.03	22.7	0.24	0.9 ± 0.1	001	1.91	7.0	22.8 4.7	-00-0	001
857*	1.10 ± 0.02	22.4	0.21	0.9 ± 0.1	000	1.95	14.8	23.5 2.6	00000	000
858*	1.25 ± 0.14	22.1	0.23	0.9 ± 0.1	000	1.98	5.5	23.1 3.7	-00-0	001
859*	1.18 ± 0.05	22.2	0.32	0.7 ± 0.1	001	1.93	3.7	23.0 3.9	00010	000
860*	1.04 ± 0.02	22.3	0.27	0.9 ± 0.3	001	1.91	20.4	23.1 3.4	00010	001
861	1.32 ± 0.13	22.2	00-	1.96	8.7	23.0 3.8	10010	001
862	1.09 ± 0.04	22.2	...	1.1 ± 0.1	00-	1.95	14.3	23.4 2.6	00000	001
863*	1.20 ± 0.06	22.3	0.19	0.9 ± 0.1	000	1.95	10.7	23.3 3.0	00010	001
864*	1.05 ± 0.02	22.4	0.20	...	000	1.96	6.7	23.5 2.6	00010	000
865*	1.02 ± 0.02	22.3	0.27	0.9 ± 0.1	000	1.93	13.0	23.4 2.8	00010	001
866*	1.08 ± 0.05	22.1	0.34	...	001	1.96	4.7	23.5 2.5	00000	101
867*	1.13 ± 0.01	22.1	0.39	...	001	1.96	16.4	23.2 3.3	00000	001
868	1.74 ± 0.13	21.5	0.15	...	110	2.01	12.2	23.0 4.1	01100	001
869	1.35 ± 0.01	22.0	0.22	...	000	1.92	5.8	22.9 4.4	00000	001
871	1.40 ± 0.04	21.7	00-	1.95	11.0	23.0 3.8	00110	000
872*	1.37 ± 0.05	21.7	0.22	1.0 ± 0.1	000	1.94	6.5	23.0 4.1	-00-0	001
874*	1.14 ± 0.05	21.8	0.31	0.8 ± 0.1	001	1.95	9.7	23.1 3.6	00010	001
877*†	1.10 ± 0.05	...	0.22	1.0 ± 0.1	0-0	1.94	5.1	22.9 4.3	10010	001
878*	1.37 ± 0.07	22.1	0.18	1.1 ± 0.1	000	1.91	4.1	23.5 2.5	00000	001
880	1.25 ± 0.07	22.0	...	0.9 ± 0.1	00-	1.91	8.7	22.8 4.9	00000	001
881*	1.17 ± 0.11	22.0	0.30	0.9 ± 0.2	000	1.96	5.3	23.2 3.4	-00-0	000
883*	1.13 ± 0.04	22.1	0.31	0.9 ± 0.1	001	1.90	2.6	22.7 5.1	00000	001
884	1.49 ± 0.13	21.8	00-	2.01	5.8	23.0 3.9	01000	101
885	1.15 ± 0.00	22.1	00-	1.93	12.4	23.3 3.1	-00-0	000
886	1.32 ± 0.09	22.0	0.19	0.9 ± 0.1	000	1.99	13.8	22.3 7.3	00011	001
887*	1.05 ± 0.01	22.2	0.29	0.8 ± 0.1	000	1.89	10.4	23.1 3.8	-00-0	001
888*	1.08 ± 0.05	21.9	0.41	...	001	2.01	1.3	23.1 3.8	01000	000
890*	1.02 ± 0.01	21.8	0.23	0.9 ± 0.1	000	1.94	10.8	23.4 2.9	-00-0	000
891	1.20 ± 0.03	22.1	00-	1.94	4.1	23.0 4.1	10110	000
893*	1.40 ± 0.21	21.8	0.15	1.0 ± 0.1	100	1.95	3.2	22.8 4.6	-00-0	001
894	1.03 ± 0.01	22.5	00-	1.98	8.0	23.1 3.7	10100	101
895	1.12 ± 0.03	21.9	00-	1.99	5.2	23.2 3.4	-00-0	001
896*	1.03 ± 0.02	22.3	0.14	1.4 ± 0.3	000	2.13	8.3	23.2 3.3	01100	000
898	1.20 ± 0.09	22.2	0.24	...	000	1.97	6.1	22.6 5.9	00100	000
901*	1.20 ± 0.10	22.1	0.25	1.0 ± 0.2	000	2.02	10.7	22.9 4.5	01010	000
902*	1.38 ± 0.14	21.7	0.21	1.1 ± 0.1	000	1.97	17.0	23.2 3.3	00010	001
903	1.26 ± 0.07	21.9	0.12	...	000	1.95	12.6	22.8 4.6	00010	000

Table 7. continued.

ID ^a	airmass ^b	$\mu_{V,\text{sky}}^c$	A_V^d	seeing ^e	flags(O) ^f	δ_i^g	S/N(R_{50}) ^h	$I_{3\sigma}^i$	flags(R) ^j	flags(C) ^k
904*	1.27 ± 0.08	21.7	0.22	1.3 ± 0.3	000	1.99	9.2	23.0 3.9	00000	101
909	1.29 ± 0.11	21.9	0.12	...	000	1.95	7.6	22.5 6.1	00000	001
910	1.28 ± 0.06	21.8	00–	2.05	6.8	23.0 4.0	–10–0	000
913	1.24 ± 0.10	22.1	01–	2.24	13.4	22.9 4.3	01100	001
914	1.16 ± 0.02	22.0	00–	1.92	12.4	23.2 3.4	00010	101
915	1.30 ± 0.11	22.0	00–	1.90	12.2	23.3 3.1	00010	001
916	1.21 ± 0.07	22.2	0.13	...	000	2.00	12.0	22.9 4.4	01010	000
917	1.12 ± 0.01	22.4	0.20	...	000	1.93	11.6	23.0 3.9	00010	001
922	1.23 ± 0.06	22.0	0.14	...	000	1.94	11.0	23.4 2.7	00000	100
924	1.32 ± 0.06	21.9	00–	1.94	10.4	23.3 3.1	00000	101
927	1.29 ± 0.05	22.0	0.11	...	000	1.98	3.9	22.7 5.1	00000	001
930	1.27 ± 0.05	21.9	00–	1.90	7.8	23.5 2.4	00000	000
932	1.29 ± 0.05	21.8	0.12	...	000	1.95	10.6	23.3 3.0	00000	001
935*	1.09 ± 0.06	22.3	0.18	...	000	2.13	4.5	23.4 2.8	01100	000
936	1.45 ± 0.13	21.6	00–	1.94	7.0	23.0 3.9	–00–0	001
937	1.16 ± 0.04	22.1	0.19	...	000	1.98	7.1	23.2 3.2	–01–0	101
938	1.13 ± 0.07	...	0.23	1.0 ± 0.1	0–0	1.94	12.6	23.4 2.8	00000	000
939*	1.32 ± 0.08	21.9	0.28	0.9 ± 0.1	001	1.89	5.2	23.3 3.0	–00–0	000

Notes. We describe the meaning of each column including the identifier of each column in the electronic table available on the DR2 web page. ^(a) IDs marked with an asterisk were already part of the DR1. A dagger indicates cubes that were registered with the old method of the pipeline V1.3c. ^(b) Mean airmass (OBS_AIR_MEAN) and rms (OBS_AIR_RMS) of the observations for the frames used to create the considered datacube. ^(c) Average night-sky surface brightness (OBS_SKY_MAG) in the V band during the observations in units of mag arcsec⁻². ^(d) Average night-sky attenuation (OBS_EXT_MEAN) in the V band during the observations in magnitudes. ^(e) Average natural seeing (OBS_SEEING_MEAN) in the V-band during the observations in arcsec (FWHM). ^(f) Observation quality flags, combining the three individual column flags (FLAG_OBS_AM, FLAG_OBS_SKYMAG, FLAG_OBS_EXT) as described in Sect. 5. ^(g) Average spectral resolution (RED_DISP_MEAN) in Å (FWHM), measured by fitting the night-sky emission lines with single Gaussian functions. ^(h) Average signal-to-noise ratio (CAL_SNR_IHLR) estimated for the full wavelength range at one half light radius from the center. ⁽ⁱ⁾ Average flux at the 3 σ continuum detection limit in units of B-band mag arcsec⁻² and in units of 10⁻¹⁸ erg s⁻¹ cm⁻² Å⁻¹ arcsec⁻². ^(j) Reduction/instrumental performance quality flags, combining the five individual column flags (FLAG_RED_STRAYLIGHT, FLAG_RED_DISP, FLAG_RED_CDISP, FLAG_RED_SKYLINES, FLAG_RED_LIMSB) as described in Sect. 5. ^(k) Quality control CAL flags, combining the three individual column flags (FLAG_CAL_SPECPHOTO, FLAG_CAL_WL, FLAG_CAL_IMA) as described in Sect. 5.

Appendix A: Computing the error spectrum for co-added spectra

Some science cases require a minimum S/N in the spectra, especially in the outer parts of the galaxies. This is achieved by spatially co-adding spaxels in the datacubes, often by means of an adaptive binning method like the Voronoi-binning scheme, implemented for optical IFS data by Cappellari & Copin (2003). However, the final error spectrum of the co-added spectra cannot be simply quadratically summed since the spectra are not independent of each other. As described in Sect. 3.1, we adopt an inverse-distance weighted image reconstruction which, like many other image resampling schemes, introduces a correlation between spaxels in the final datacube. In Sect. 3.2 we provide an equation that relates the analytically propagated error recorded in the datacubes with the final "real" error of the co-added spectra¹².

Let B be a bin of size N spectra, i.e. we want to co-add N spectra and compute the corresponding error spectrum for that bin. Since we are adding the flux to obtain an integrated spectra, first we need to add the errors of each individual spectra in quadrature:

$$\epsilon_B^2 = \sum_{k=1}^N \epsilon_k^2$$

This would be the error spectrum of the bin B if the spaxels were completely independent. To account for the correlated noise, we just need to multiply by the corresponding "correlation factor" (Eq. 1) for a given number of spectra in a particular bin:

$$\epsilon_{\text{real},B}^2 = \beta(N)^2 \times \epsilon_B^2$$

When the bin B contains a large number of spaxels ($N \gtrsim 80$), the use of Eq. 1 is not recommended. In this case, the ERWEIGHT HDU extension of the CALIFA FITS file datacube should be used (see Table 2) as a correction factor for each spaxel.

¹² See also Sect. 3.2 and 3.3 of Cid Fernandes et al. (2013) for a detailed disquisition on error propagation and correlated noise for IFS.